

Interactive Modelling of Glacier Climatic Mass Balance in the Karakoram Range

by

Sarah Emily Collier

A thesis submitted in partial fulfillment of the requirements for the degree of

Doctor of Philosophy

Department of Earth and Atmospheric Sciences

University of Alberta

©Sarah Emily Collier, 2015

Abstract

Glacier behaviour in the Karakoram region of the greater Himalaya shows strong spatial and temporal heterogeneity and, in some areas, anomalous trends compared with glaciers elsewhere in High Asia. Knowledge of the mass balance fluctuations of Karakoram glaciers, as well as of the important driving factors and interactions between them, is limited by a scarcity of observational data. A novel approach to simulating atmosphere-cryosphere interactions is developed as a multi-scale solution to the paucity of information in this region: a process-based climatic mass balance (CMB) model is interactively coupled with a regional atmospheric model (Weather and Research Forecasting model, or WRF). The coupled model (hereafter WRF-CMB) is used to (1) investigate the surface-energy and climatic-mass fluxes of glaciers in the Karakoram over an ablation season, and (2) compare the traditional, one-way approach to simulations of glacier CMB with an interactive one. Both simulations reproduce observed magnitudes of CMB, with improvements arising from the inclusion of feedbacks from the CMB model to WRF.

Supraglacial debris is prevalent in the Karakoram, with an estimated mean proportion of glacier area covered by debris of $\sim 20\%$. As debris exerts a strong control on glacier melt, there is a need to determine its influence on glacio-hydrological processes in this region. Therefore, a debris component is introduced into the CMB model that provides the first numerical treatment of moisture fluxes and phase changes in the debris layer to date, using simple parameterizations for the debris ice and water content and the latent heat flux. A case study is performed for the Miage Glacier in the Italian Alps, due to the availability of eddy covariance measurements over glacier debris cover. By comparing a “dry” and a “moist” simulation, the importance of moisture on the surface-energy and climatic-mass balance of debris-covered glaciers is investigated. Sub-debris ice melt during the ablation season is reduced when moisture effects are considered,

mainly due to surface heat extraction by the latent heat flux, while during transition seasons, the presence of ice at the base of the debris layer contributes to a reduction in simulated ablation.

To investigate glaciological and meteorological changes that arise due to the presence of debris in the Karakoram, the modified CMB model is introduced into WRF-CMB and two simulations are performed: one that treats glacier surfaces as debris-free and one that introduces an idealized specification for debris thickness. Debris cover strongly reduces simulated ablation, particularly at lower altitudes, with a regional mean reduction in mass loss of 30 % over an ablation season. By altering surface boundary conditions, the presence of debris also impacts near-surface meteorological conditions and atmospheric boundary layer dynamics, through changes in the turbulent exchanges of heat and moisture between the glacier surface and the atmosphere. The research presented in this thesis contributes towards an improved understanding of glacier behaviour in the Karakoram and lays the foundation for investigations of glacier change in this region over longer time periods.

Preface

Chapters one and two of this thesis were published as the following two papers:

- **Collier, E.**, Mölg, T., Maussion, F., Scherer, D., Mayer, C., and Bush, A. B. G.: High-resolution interactive modelling of the mountain glacieratmosphere interface: an application over the Karakoram, *The Cryosphere*, 7, 779-7-95, doi:10.5194/tc-7-779-2013, 2013.
- **Collier, E.**, Nicholson, L.I., Brock, B.W., Maussion, F., Essery, R. and Bush, A. B. G.: Representing moisture fluxes and phase changes in glacier debris cover using a reservoir approach, *The Cryosphere*, 8, 1429–1444, doi:10.5194/tc-8-1429-2014, 2014.

I completed the model development with T. Mölg and L. Nicholson for the first and second papers, respectively. For both publications, I performed the data analysis and composed the manuscript. My co-authors provided data for model evaluation and valuable feedback on the interpretation of the results and content of the manuscripts.

Chapter three is unpublished original work that was completed mainly in collaboration with F. Maussion, who performed the debris-thickness specification. I completed the code development, model simulations, data analysis and manuscript composition. L. Nicholson, W. Immerzeel, and A.B.G. Bush provided helpful feedback on the manuscript and its interpretations. The manuscript has been submitted as:

- **Collier, E.**, Maussion, F., Nicholson, L.I., Immerzeel, W. and Bush, A. B. G.: Impact of debris cover on glacier ablation and atmosphere-glacier feedbacks in the Karakoram, submitted to *The Cryosphere*, 2014.

Acknowledgements

Financial support for this research was provided by the Natural Sciences and Engineering Research Council of Canada, Alberta Innovates, and the University of Alberta. I would like to express my gratitude to Canadians and the Governments of Canada and Alberta for supporting the work of scientists.

The high-performance computing resources were provided by Compute/Calcul Canada and WestGrid. I am very grateful for the assistance and technical support provided by WestGrid system administrators, particularly those working with the nexus, checkers, and bugaboo clusters.

I would like to thank my supervisor, Andrew Bush, for his guidance and support throughout my graduate studies and for championing my research. I would also like to thank the members of my supervisory committee, Gordon Swaters and Jeff Kavanaugh, for their feedback and assistance, and the members of my candidacy and defense committees for their participation (Paul Myers, Mathieu Dumberry, and Bruce Sutherland). Thank you to Brian Menounos for acting as the external advisor.

I am grateful to Dieter Scherer and Mathias Rotarch for hosting me as a visiting researcher at the Chair of Climatology (Technical University of Berlin, Germany) and the Institute of Meteorology and Geophysics Innsbruck (University of Innsbruck, Austria), respectively. These visits provided me with exceptional opportunities for collaboration and academic training. I am deeply thankful for the scientific contributions and support of my main collaborators at these institutions: Fabien Maussion, Thomas Mölg, and Lindsey Nicholson. I would also like to thank Walter Immerzeel for his patience and helpful input during the final stretch of my PhD research.

Thank you to my friends and colleagues at TU Berlin, the University of Innsbruck, and the

University of Alberta for making my graduate studies productive and enjoyable. Finally, I am especially grateful for the support provided by my family over the long course of my studies. Special thanks to my parents for their generous support and encouragement; to Janet Millar for her impeccable editing services; and to my partner Paul Zöll for the many invaluable ways he helped and encouraged me while I completed my thesis.

Contents

Abstract	ii
Preface	iv
Acknowledgements	v
Contents	vii
List of Figures	viii
List of Tables	ix
1 Introduction	1
1.1 Study area and motivation	1
1.2 Obtaining meteorological forcing data	3
1.3 Influence of supraglacial debris	4
1.4 Thesis objective and outline	6
References	8
2 High-resolution interactive modelling of the mountain glacier–atmosphere interface: an application over the Karakoram	14
2.1 Introduction	14
2.2 Methods	18
2.2.1 Mesoscale atmospheric model	18

2.2.2	Surface energy and climatic mass balance model	20
2.2.3	Coupling architecture	21
2.2.4	Measurements for model evaluation	23
2.3	Results and discussion	24
2.3.1	Remote sensing data	25
2.3.2	Baltoro glacier	27
2.3.3	Influence of interactive coupling	32
2.3.4	Remarks and perspectives for future research	40
2.4	Conclusion	44
References		45
3	Representing moisture fluxes and phase changes in glacier debris cover using a reservoir approach	52
3.1	Introduction	52
3.2	Methods	54
3.2.1	Debris-free glacier CMB model	54
3.2.2	Inclusion of debris	55
3.2.3	Miage Glacier case study	62
3.3	Results	67
3.3.1	Comparison with in situ measurements	67
3.3.2	Modelling insights from the 2008 simulation	67
3.3.3	Impact of phase changes in the 2011 simulation	73
3.4	Discussion	77
3.5	Conclusion	82
References		84
4	Impact of debris cover on glacier ablation and atmosphere-glacier feedbacks in the Karakoram	89
4.1	Introduction	89

4.2	Methods	91
4.2.1	Regional atmospheric model	92
4.2.2	Glacier CMB model with debris treatment	94
4.2.3	Specification of debris extent and thickness in WRF D3	97
4.2.4	Evaluation of simulated land surface temperature	100
4.3	Results	103
4.3.1	Meteorological drivers of glacier fluctuations	103
4.3.2	Glacier surface energy and climatic mass dynamics	105
4.3.3	Atmosphere-glacier feedbacks	109
4.4	Discussion	112
4.5	Conclusions	117
	References	119
	5 Perspectives for future research	127
	References	130
	Works Cited	132

List of Figures

1.1	The Karakoram range of the Hindu Kush-Himalaya and surrounding area. Glaciers (Pfeffer et al., 2014) and their debris-covered areas (Kääb et al., 2012) are shaded in blue and grey, respectively. The wider geographical location of the Karakoram is shown in the subset.	2
2.1	(a) WRF atmospheric model domains, configured with horizontal spatial resolutions of 33, 11, and 2.2 km. Terrain elevation from the GTOPO30 dataset is shaded in units of meters. (b) Outline of Baltoro glacier and its tributaries, which are included in WRF D3, with the mean stake locations labeled and denoted by stars.	17
2.2	Comparison between WRF-CMB D3, Noah LSM, and MODIS for land surface temperature, (a) averaged from 25 June–28 August 2004, and in 50 m elevation bins; (c) the mean time series above 5200 m elevation; and for (b) snow albedo, averaged between 25 June–31 August 2004, over glacier grid cells where at least 25 % of the daily times are available.	26
2.3	Hourly (a) air temperature at 2 m, (b) relative humidity at 2 m, (c) wind speed at 10 m, and (d) surface air pressure, as well as (e) daily total precipitation. Solid black (blue) curves display data from the interactive (offline) simulations while the dashed grey curve is the Urdukas AWS station data. Note the difference in elevation of the AWS (4022 m a.s.l.) and the terrain height in the closest WRF grid cell (4322 m).	28

2.4	<p>(a) Total and (b) INT-OFF surface height change between 1–15 July 2004, in the vicinity of the main tongue of the Baltoro glacier. Stake site and transect locations shown in (b), with additional information provided in Table 2.3. White grid cells correspond to non-glacierized area. (c) Measured mean ablation (triangles) at stake locations, with range of observed values denoted by bars. Simulated INT (OFF) ablation shown by black squares (blue circles).</p>	31
2.5	<p>Daily mean (a) air temperature, (b) relative humidity, (c) wind speed, (d) total precipitation, incoming (e) normal short-wave and (f) downward long-wave radiation at ground surface, (g) air pressure, and (h) frozen fraction of precipitation, area-averaged over all glacierized grid cells. Data for (a–c), and (g) are taken from the lowest model level ($z = 20$ m). The subpanel in (a) presents the average diurnal temperature cycle over the simulation period. Black (blue) curves display data from the interactive (offline) simulation.</p>	33
2.6	<p>Vertical and subsurface distribution of the influence of interactive coupling over glacierized areas illustrated by hourly time series of the change (INT-OFF) in area-averaged (a) air temperature, (b) specific humidity, (c) subsurface temperature, and (d) cloud fraction.</p>	35
2.7	<p>Daily basin-scale averages of (a) accumulated surface height change, (b) accumulated total mass balance, and (c) surface temperature. Black (blue) curves display data from the interactive (offline) simulation. For reference, surface temperature simulated by the Noah LSM is the dashed grey curve in (c).</p>	36
2.8	<p>(a) The vertical mass balance profile of the Karakoram basin at the end of the simulation. The altitudinal dependence of (b) total accumulated precipitation, and (c) mean frozen fraction, averaged over the simulation. Data are area-averaged in 50 m elevation bins.</p>	38

2.9	From the interactive WRF-CMB simulation: daily (a) mean surface energy balance components (left y-axis; see Eq. 1 for explanation of symbols) and albedo values (grey right y-axis), and (b) sums of mass fluxes. The radiation variables are shown in (a) as solid (directed downward) and dashed (upward) lines, albedo as grey dots, and the other surface energy fluxes as bars. The heat flux from precipitation (QPRC) is negligible and not shown. Values are averaged over glacierized grid cells only.	39
2.10	Area-averaged mean difference (INT – OFF) over the simulation period and over glacierized grid cells of (a) the main components of the WRF surface energy budget, (b) the CMB model energy fluxes, and (c) the MB model mass fluxes. Symbols in (a) represent, from left to right, net short- and long-wave radiation, ground heat flux, and turbulent fluxes of sensible and latent heat. Note that the sign convention for the turbulent fluxes in (a) is opposite to (b) . Symbols in (b) are discussed in Sect. 2.2.2	41
3.1	Schematic of the CMB-RES model and its treatment of the debris moisture content and its phase. The levels m_S , m_D , and m_K correspond to the bottom of the snowpack, the base of the debris layer, and the level of the saturated horizon, respectively.	59
3.2	Map showing the location of the Miage Glacier. The AWS located on the glacier is denoted with a red circle and the AWS2 from which precipitation data were obtained is shown by a red triangle.	63
3.3	Times series from the 2008 simulation of the forcing variables of (a) 2 m air temperature (K), (b) wind speed (m s^{-1}), (c) 2 m vapour pressure (hPa), (d) incoming shortwave radiation (W m^{-2}), (e) incoming longwave radiation (W m^{-2}), (f) surface pressure (hPa), and (g) precipitation (mm). Data from the AWS on the Miage Glacier are shown in black, from the second AWS (4 km away) in blue, and temporally downscaled from the ERA-Interim reanalysis in green. Dashed curves indicate the discarded spin-up period, while solid curves indicate the simulation time.	64

3.4	Time series from the 2008 simulation of (a) debris surface temperature (T_{sfc} ; K) and the turbulent fluxes of (b) sensible and (c) latent heat (W m^{-2}), for measurements (black curve), CMB-DRY (dark grey curve), and CMB-RES (blue, dashed curve). (d) Same as panel a , but for the 2011 simulation. The horizontal dashed red line indicates the freezing point, 273.15 K.	68
3.5	Time series from the 2008 simulation of (a) surface (dashed-blue curve) and 2 m air (black curve) vapour pressure (hPa) in CMB-RES, and (b) total accumulated mass balance (kg m^{-2}) for CMB-DRY (solid-grey curve) and CMB-RES (dashed-blue curve).	70
3.6	CMB-RES values for (a) daily mean energy fluxes over the evaluation period (W m^{-2}). The grey curve is net shortwave radiation, the black curve is net long-wave radiation, and the grey dots show daily-mean surface albedo, which remains constant at the debris value because there is no solid precipitation. (b) Daily total mass fluxes (kg m^{-2}). Maximum daily values of evaporation and condensation are 1.4 and 0.02 kg m^{-2} , respectively, although the latter flux is not visible. Note that while daily-accumulated rainfall is shown (purple asterisks), it is not technically a mass flux, since the mass balance calculation in CMB-RES does not account for debris-water storage. Rather, this field is plotted to show its correspondence with other fields, such as net shortwave radiation.	71
3.7	Time series of total debris-water content (black curve) as well as the two sources of debris-water loss: horizontal drainage (solid-grey curve) and evaporation (dashed-grey curve). Units are in kilograms per square metre (kg m^{-2}).	73
3.8	Depth variation of (a) debris thermal conductivity ($\text{W m}^{-1} \text{K}^{-1}$), (b) density (kg m^{-3}), and (c) specific heat capacity ($\text{J kg}^{-1} \text{K}^{-1}$), shown for CMB-DRY in grey-unfilled circles and for CMB-RES in both black-filled circles (“dry” time slice) and blue asterisks (“wet” time slice). Time series of bulk values for these same properties are shown in panels (d–f) for CMB-RES in blue and CMB-DRY in grey. The locations of the “dry” and “wet” time slices are indicated by the first (solid grey) and second (dashed grey) reference lines on the x axis, respectively. .	74

3.9	Temporal and depth variation of (a) CMB-RES debris temperature and (b) the difference between the model runs (CMB-RES minus CMB-DRY). Units are in Kelvin (K). For reference, $-1*QL$ (solid-black curve; now positive for energy loss from the surface) and debris-water content (black dashed) are plotted without y axes in panel (b) . The height of the debris-water curve shows the estimated level of moisture in the reservoir.	75
3.10	Same as Fig. 3.6 but for the 2011 simulation.	78
3.11	(a) Time series from the 2011 simulation of the debris water (black line) and ice (grey line) content (kg m^{-2}). Temporal and depth variation of the debris temperatures in (b) CMB-RES and (c) CMB-DRY, and (d) the difference between the model runs (CMB-RES minus CMB-DRY). Units are in Kelvin (K).	79
3.12	Daily mean subdebris ice ablation rate (mm w.e. d^{-1}) vs. debris thickness (cm), produced by the CMB models using the forcing data from the 2008 simulation. The clean-ice-melt rate is represented by a black triangle. CMB-DRY is the solid-grey curve and CMB-RES is the dashed-blue curve.	81
4.1	Topographic height shaded in units of m for (a) all three model domains in WRF-CMB, which are centered over the Karakoram and configured with grid spacings of 30-, 10- and 2-km resolution and grid dimensions of 84x105, 109x109 and 186x186, and (b) a zoom-in of the finest resolution domain, WRF D3. . . .	90
4.2	(a) debris-covered (grey) and debris-free (blue) glacier area, as calculated on the HR (40-m) grid for the Baltoro glacier and surrounding areas. The result of the debris thickness specification for (b) the Baltoro glacier and (d) the entire WRF-D3 region. In (d), the red line delineates the region where centerline information was available from (Rankl et al., 2014). (c) A box plot of debris thicknesses values for 250-m elevation bins in WRF D3. The thick-blue and thin-black lines indicate the mean and median thickness value in each bin and the total number of debris-covered pixels is given as a text string at the upper end of the range. . .	99

4.3	<p>(a) Mean elevational profiles of land surface temperature from DEB, CLN, and composite MODIS Terra MOD11A1/Aqua MYD11A1 datasets, averaged from 1 May to 1 October 2004 and in 250-m elevation bins over glacierized pixels in WRF. MODIS data with the highest quality flag are projected on to the WRF D3 grid prior to averaging and compared with WRF data points from the same [local solar] time step. (b) A sample time slice of MODIS Terra LST from 5 August 2004 on its native grid, overlaid on the Baltoro glacier outline and debris-covered area. (c) Time series of LST from 1 July to 31 August 2004 from the same datasets in panel (a), taken from the pixel on the Baltoro tongue denoted by a black circle in panel (b).</p>	102
4.4	<p>Time series of daily-mean meteorological data in the DEB simulation, area-averaged over glacierized grid cells: (a) air temperature [K], (b) vapour pressure [hPa], (c) wind speed [m s^{-1}], incoming (e) short- and (f) long-wave radiation [W m^{-2}], and (g) pressure [hPa]. Data were taken from the lowest model level, which was specified at a height of ~ 17 m. Panel (d) shows daily total precipitation in [mm]. Panel (h) shows the daily maximum number of exposed debris pixels in DEB, with the grey reference line on the y-axis indicating the 10% threshold for temporal averaging of subsequent results.</p>	104
4.5	<p>Geopotential height contours shaded in units of [m] and wind vectors at 500 hPa in WRF D1 averaged over (a) the whole simulation period of 1 May to 1 October 2004, and over (b) days with total precipitation exceeding 5 mm. The extent of WRF D3 is delineated by the black box. (c) Total accumulated precipitation in WRF D3 over the simulation, overlaid by wind vectors averaged over the lowest 500 hPa above the surface and over hours with basin-mean precipitation exceeding 0.25 mm.</p>	106

4.6	(a) The mean percentage of pixels containing in each 250-m elevation bin between 3000 and 7500 m a.s.l., with min and max values delimited by the dashed lines. Elevational profiles of mean glacier (b) surface-energy and (c) mass fluxes., with the solid (dashed) line denoting data from DEB (CLN). Note the non-linear x axis in panel (c).	108
4.7	(a) Daily mean ice melt rate versus debris thickness for DEB (circle markers) and CLN (line markers), colored by their topographic height values. DEB values represent sub-debris ice ablation, while CLN values represent surface melt, considering only snow-free pixels (333 in total). (b) Vertical balance profile, averaged over all glacier pixels and in 250-m elevation bins. Grey-square markers denote results from the CLN simulation, while those from DEB are plotted with black markers, with the marker shape determined by the mean debris thickness.	110
4.8	Total accumulated mass balance in [kg m ⁻²] between 1 July–1 October 2004 for (a) the DEB simulation and (b) the difference between DEB and CLN.	111
4.9	For the DEB simulation, (a) date of the start of the summer melt season and (b) total number of hours where surface temperatures reach or exceed the melting point (melt hours). (c) Difference in total melt hours between the two simulations.	113
4.10	Elevational profiles of (a) air temperature [K] and (b) relative humidity [%] at a height of 2m; (c) wind speed at a height of 10 m; (d) accumulated precipitation, from the DEB (black-circle markers) and CLN (grey-square) simulations. The temporal averaging period is 1 July to 1 October 2004.	114
4.11	(a) Elevational profile and (b) diurnal cycle of the planetary boundary layer height over exposed debris in DEB (black markers and curve) and their equivalent pixels in CLN (grey).	115

List of Tables

2.1	WRF configuration.	19
2.2	MB model configuration.	22
2.3	Summary of available ablation stake measurements from the Baltoro glacier.	24
2.4	Ablation rates (cm day^{-1}) and debris thickness on the Baltoro glacier.	30
3.1	Physical parameter values used in the CMB models.	56
3.2	Subsurface layer distribution and debris thickness used in this study.	57
3.3	Mean deviation (MD), mean absolute deviation (MAD), and R value for the evaluation variables of surface temperature (T_{sfc}), and the turbulent fluxes of sensible (QS) and latent heat (QL).	69
3.4	Average-energy and accumulated-mass fluxes at the surface over the 2008 simulation for CMB-RES and CMB-DRY.	72
3.5	Average-energy and accumulated-mass fluxes at the surface over the 2011 simulation for CMB-RES and CMB-DRY.	76
4.1	WRF configuration	93
4.2	Subsurface layer depths.	94
4.3	Physical properties in the CMB model.	96
4.4	Mean glacier surface-energy and climatic-mass fluxes.	107
4.5	Elevational lapse rates.	112

Chapter 1

Introduction

1.1 Study area and motivation

The Karakoram range of the Hindu Kush-Himalaya (HKH; $\sim 74\text{-}77^\circ\text{E}$, $34\text{-}37^\circ\text{N}$) is extensively glacierized, with an estimated ice-covered area of $\sim 18,000 \text{ km}^{-2}$ (Fig. 1.1; Bolch et al., 2012). Supraglacial debris is prevalent in this region, with a mean proportion of debris-covered glacier area of $\sim 18\text{-}22 \%$ (Scherler et al., 2011a; Hewitt, 2011). The Karakoram has received increased scientific attention in recent years due to evidence of stable, or even slightly positive, mass balances for approximately half of the glaciers (e.g. Hewitt, 2005; Scherler et al., 2011a; Gardelle et al., 2012, 2013; Kääb et al., 2012) that are in contrast with predominantly negative glacier mass balances in the rest of the HKH (Cogley 2011). The concept of a “Karakoram anomaly” was first proposed by Hewitt (2005) on the basis of field observations during the 1990s: the presence of termini thickening and advancement of some of the highest glaciers; a small number of glaciers overriding their lateral moraines, and; an increased prevalence of glacier surge activity. A study of termini positions and surface velocities of 286 glaciers across the HKH provided further support for a regional anomaly, since, over the period of 2000 to 2008, 58 % of glaciers studied in the Karakoram were stable or advanced, in contrast to $\geq 65 \%$ of glaciers in retreat studied elsewhere (Scherler et al., 2011a).

Recent geodetic studies provided the first definitive confirmation of stable or slightly positive mass balances in the Karakoram (Gardelle et al., 2012, 2013; Kääb et al., 2012). Based on

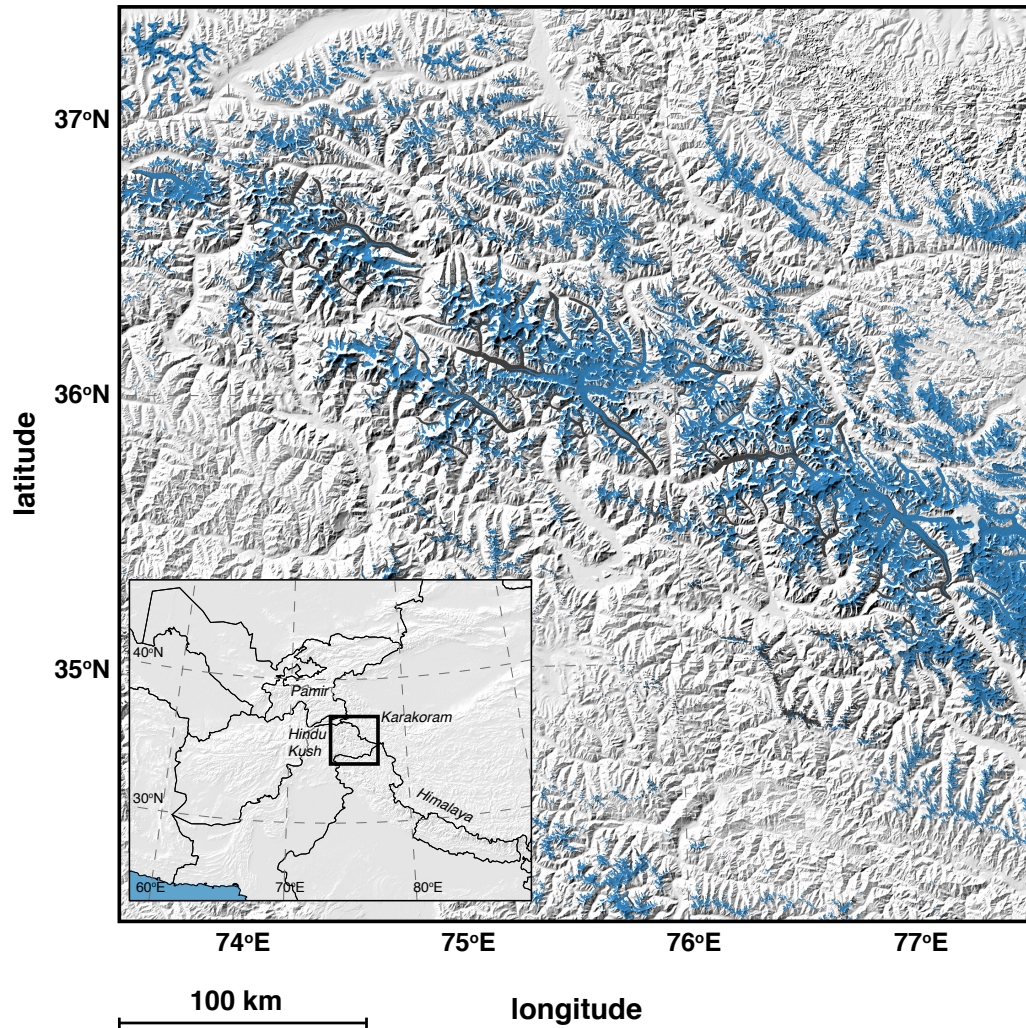


Figure 1.1: The Karakoram range of the Hindu Kush-Himalaya and surrounding area. Glaciers (Pfeffer et al., 2014) and their debris-covered areas (Kääb et al., 2012) are shaded in blue and grey, respectively. The wider geographical location of the Karakoram is shown in the subset.

differencing of digital elevation models between 1999 and 2008, Gardelle et al. (2012, 2013) reported a regional-mean elevation change of $\sim 0.11 \pm 0.22 \text{ m w.e. a}^{-1}$ for the central Karakoram and surrounding area, while Kääb et al. (2012) found approximately balanced mass budgets in the region using ICESat data between 2003 and 2008. Furthermore, Gardelle et al. (2013) reported a similar anomaly in the neighboring Pamir range ($0.14 \pm 0.10 \text{ m w.e. a}^{-1}$), leading the authors to propose the concept of a “Pamir-Karakoram anomaly.” These studies highlighted the anomalous nature of recent changes in these regions compared with the western, central and eastern Himalaya, where the measured elevation changes were 0.41 ± 0.11 , 0.21 ± 0.10 , and $0.29 \pm 0.09 \text{ m w.e. a}^{-1}$, respectively (Gardelle et al., 2013).

The anomalous response of Karakoram glaciers has been frequently attributed to observations of increasing winter precipitation and decreasing spring and summer temperatures in the Karakoram during the latter part of the 20th century, as recorded at low-altitude weather stations (Archer and Fowler, 2004; Fowler and Archer, 2006) and as indicated by tree-ring records (Yadav et al., 2004; Treydte et al., 2006). While the aforementioned remote-sensing studies have contributed more information about recent glaciological changes, definitive attribution of causality to certain climate trends or atmospheric circulation patterns is hampered by a lack of both observational data (in particular at high altitudes) and high-resolution meteorological data. Thus, there remains a fundamental gap in our understanding of drivers of glaciological changes in the Karakoram, which numerical modelling has the potential to address.

1.2 Obtaining meteorological forcing data

Distributed simulations of glacier climatic mass balance (CMB: denoting mass fluxes at the surface and in the upper-subsurface; Cogley et al., 2011), require distributed local meteorological data as forcing. Commonly used approaches for glacier simulations include (1) extrapolation of automatic weather station (AWS) data and (2) interpolation of meteorological data from atmospheric models and reanalyses using surface- and free- air lapse rates, respectively. However, surface lapse rates of air temperature (a strong driver of ablation) have been observed to vary significantly and non-linearly in both space and time on debris-free glaciers (e.g. Marshall et al., 2007; Gardner et al., 2009; Brock et al., 2010; Petersen and Pellicciotti, 2011). The issue of

variability seems to be equally relevant, if not more so, on debris-covered glaciers, since the debris surface temperature is not limited by the ice melting point. Brock et al. (2010) confirm large fluctuations in lapse rates of near-surface air temperatures from measurements on the Miage Glacier in the Italian Alps, with daytime values that exceed the commonly assumed average moist adiabatic lapse rate of 6.5 K km^{-1} , rapid diurnal variations, and a locational dependence on factors such as topographic shading. Additional statistical techniques are required to account for the poor representation of the strength and spatial variability of orographic precipitation in coarse spatial-resolution atmospheric models (e.g. Radić and Hock, 2011).

Dynamical downscaling has been used to address the issue of spatial resolution in the most recent studies, by producing climate data at grid spacings of 1-10 km as forcing for glacier mass-balance models (Mölg and Kaser, 2011; Mölg et al., 2012a,b, 2013). However, its application in these studies has been one-way or offline, with meteorological forcing data passed to the mass-balance model but no feedbacks from changing glacier surface conditions or CMB processes incorporated. The application of dynamical downscaling is also complicated by the relatively simple treatment of glaciers in regional atmospheric models to date, with the land surface schemes frequently imposing minimum snowdepths over glacierized grid cells and retaining the same treatment as for seasonal snowcover (e.g. Chen and Dudhia, 2001; Niu et al., 2011). Preventing snow cover removal and therefore the exposure of glacier ice or debris precludes accurate simulations of glacier CMB using these forcing data, in particular for debris-covered glaciers, and contributes to a cold bias in land surface temperatures due to a higher surface albedo (Collier et al., 2013). Furthermore, key CMB processes, such as ice melt, the formation of superimposed ice, and penetrating shortwave radiation, are neglected.

1.3 Influence of supraglacial debris

The prevalence of debris cover in the Karakoram is a key factor that should be accounted for in glacio-hydrological modelling of this region, since debris exerts a strong control on glacier ablation. The relationship between debris thickness and sub-debris ice ablation rates was first quantified experimentally by Østrem (1959), who found that ablation is suppressed exponentially compared with debris-free ice melt rates as debris thickness increases above a few centimeters,

while it is enhanced below this depth. The so-called “Østrem curve” has been reproduced in subsequent empirical studies (e.g. Loomis, 1970; Fujii, 1977; Inoue and Yoshida, 1980; Mattson et al., 1993). The enhancement of sub-debris ice ablation under thinner debris has been attributed to a reduction in surface albedo, an increase in absorption of shortwave radiation, and rapid transfer of the energy to the underlying ice, while reduced melt associated with thicker debris has been attributed to insulation of the ice from atmospheric energy sources. The debris thickness under which the rate of ablation is equal to that of debris-free ice is termed the critical thickness, and ranges between 1.5-5 cm in the aforementioned studies, depending on debris lithology, its optical and thermal properties, near-surface meteorological conditions, and the glacier’s geographic location and altitude (e.g. Mattson et al., 1993; Adhikary et al., 1997).

A number of full surface-energy balance models for modelling ice ablation under debris have been developed (e.g. Kraus, 1975; Nakawo and Young, 1981; Han et al., 2006; Nicholson and Benn, 2006; Reid and Brock, 2010; Zhang et al., 2011; Reid et al., 2012; Lejeune et al., 2013). The most sophisticated models explicitly calculate heat conduction through a debris layer resolved into multiple levels (Reid and Brock, 2010), perform distributed calculations, and include a time-varying snowpack on top of the debris (Reid et al., 2012; Lejeune et al., 2013). However, with the exception of Lejeune et al. (2013), these studies assume that the underlying ice is at the melting point and there is no heat conduction into the ice, which limits the applicability of these models outside of the ablation season. Previous studies also omitted (1) the influence of moisture on the debris layer, by assuming melt or rainwater runs off immediately without ponding, influencing the debris thermal properties or undergoing phase changes; and, (2) surface moisture fluxes, with the exception of testing the two end-member cases of completely-dry or completely-saturated debris layers (e.g. Nakawo and Young, 1981; Kayastha et al., 2000; Nicholson and Benn, 2006; Reid and Brock, 2010).

Both field observations and laboratory experiments indicate that debris covers can be partially or entirely saturated at times during the ablation season, depending on the thickness and environmental conditions, with a minimum of a saturated layer adjacent to the ice interface if the ice is at the melting point (e.g. Nakawo and Young, 1981; Conway and Rasmussen, 2000; Kayastha et al., 2000; Reznichenko et al., 2010; Nicholson and Benn, 2012). The presence of

liquid or frozen water modifies the thermal properties of the debris layer (Nicholson and Benn, 2012). Furthermore, moisture exchanges between the surface and overlying atmosphere influence the surface energy balance and have been observed to be non-negligible at times. For example, during the ablation season on the Miage glacier in the Italian Alps, Brock et al. (2010) calculate large spikes in the latent heat flux (QL), of up to -800 W m^{-2} , that coincide with daytime rainfall events on the heated debris surface (with fluxes defined as positive when energy transfer is to the surface).

Debris has a strong potential to alter atmosphere-glacier feedbacks, by changing the surface boundary conditions. This is particularly evident with the surface temperature, since it is not limited to the melting point over debris, and with the turbulent fluxes of sensible and latent heat. These fluxes have been estimated to become strong energy sinks when debris is present (assuming saturation; Inoue and Yoshida, 1980; Takeuchi et al., 2000, 2001), due to heat transfer from the warmer surface to the atmosphere and stronger evaporation. The change is also consistent with the development of a deeper internal boundary layer over debris, as compared with ice, due to the formers higher surface roughness (Granger et al., 2002). Alterations to the surface energy balance contribute to noticeable differences in near-surface air temperature. For example, Takeuchi et al. (2000, 2001) measured nighttime temperatures during the ablation season on the Khumbu glacier in Nepal that were warmer over the debris-covered area than on both the adjacent debris-free ice and the glacier moraine, as well as slower nighttime cooling rates in this region.

1.4 Thesis objective and outline

The main aim of my thesis is to develop an improved and explicit treatment of alpine glaciers in atmospheric models that can be used to understand both mesoscale climatic drivers of glacier CMB fluctuations in the Karakoram and local forcing factors, such as debris cover and feedbacks between the glacier surface and the atmosphere. The thesis is divided into three main chapters:

Chapter 2: The issues highlighted in Sect. 1.2 are addressed by introducing a new, interactively coupled, high-resolution atmosphere-glacier modelling system (WRF-CMB) that contains two components: the Advanced Research version of the Weather and Research Forecasting

model (WRF Skamarock and Klemp, 2008), and the process-based glacier CMB model of Mölg et al. (2008, 2009). The coupled model is configured with three nested domains of ~ 30 –, 10– and 2–km resolution centered over the Karakoram, with the finest-resolution domain providing high-resolution atmospheric data as direct forcing for the glacier CMB model with no statistical linkages. We investigate simulated glacier surface-energy and climatic-mass fluxes as well as changes to the atmospheric forcing resulting from the inclusion of clean-glacier CMB feedbacks over an ablation season.

Chapter 3: From the perspective of coupled atmosphere-glacier modelling, neglecting the latent heat flux in the surface energy balance computation over ~ 20 % of the glacier area would introduce erroneous artifacts into the atmospheric forcing data. Therefore, the issues highlighted in Sect. 1.3 are addressed in two steps. First, a treatment for supraglacial debris is introduced into the glacier CMB model. Second, simple parameterizations are developed for the debris moisture content and its phase and for the latent heat flux. The model is evaluated over the Miage Glacier in the Italian Alps, due to the availability of eddy covariance data over the debris surface at that site. From the results, the influence of moisture on sub-debris ice-melt rates is elucidated.

Chapter 4: The influence of debris cover on Karakoram glaciers is investigated by comparing two simulations performed with WRF-CMB: one that treats glacier surfaces as debris-free (as in Chapter 2) and one that introduces an idealized debris thickness specification. The impact of debris on glacier melt and on atmosphere-glacier feedbacks over exposed debris is quantified for an ablation season.

Concluding remarks and perspectives for future research are presented in **Chapter 5**.

References

- Adhikary, S., Seko, K., Nakawo, M., Ageta, Y., and Miyazaki, N.: Effect of surface dust on snow melt, *Bull. Glacier Res.*, 15, 85–92, 1997.
- Archer, D. R., and Fowler, H. J.: Spatial and temporal variations in precipitation in the Upper Indus Basin, global teleconnections and hydrological implications, *Hydrol. Earth Syst. Sci.*, 8, 47-61, 2004.
- Bolch, T., Kulkarni, A., Kääh, A., Huggel, C., Paul, F., Cogley, J. G., Frey, H., Kargel, J. S., Fujita, K., Scheel, M., Bajracharya, S., and Stoffel, M.: The state and fate of Himalayan glaciers, *Science*, 336, 310–314, 2012.
- Brock, B. W., Mihalcea, C., Kirkbride, M. P., Diolaiuti, G., Cutler, M. E., and Smiraglia, C.: Meteorology and surface energy fluxes in the 2005–2007 ablation seasons at the Miage debris-covered glacier, Mont Blanc Massif, Italian Alps. *J. Geophys. Res.*, 115, D09106, doi:10.1029/2009JD013224, 2010.
- Chen, F. and Dudhia, J.: Coupling an advanced land surface-hydrology model with the Penn State – NCAR MM5 modelling system. Part I: Model implementation and sensitivity, *Mon. Weather Rev.*, 129, 569–585, 2001.
- Cogley, J. G., Hock, R., Rasmussen, L. A., Arendt, A. A., Bauder, A., Braithwaite, R. J., Jansson, P., Kaser, G., Müller, M., Nicholson, L., and Zemp, M.: Glossary of Glacier Mass Balance and Related Terms, IHP-VII Technical Documents in Hydrology No. 86, IACS Contribution No. 2, UNESCO-IHP, Paris, 2011.
- Collier, E., Mölg, T., Maussion, F., Scherer, D., Mayer, C., and Bush, A. B. G.: High-resolution

- interactive modelling of the mountain glacier–atmosphere interface: an application over the Karakoram, *The Cryosphere*, 7, 779–795, 2013.
- Conway, H. and Rasmussen, L. A.: Summer temperature profiles within supraglacial debris on Khumbu Glacier, Nepal, *Debris-Covered Glaciers*, IAHS PUBLICATION no. 264, 89–97, 2000.
- Fowler, H., and Archer, D.: Conflicting signals of climatic change in the Upper Indus Basin, *J. Clim.*, 19, 4276–4293, 2006.
- Fujii, Y.: Experiment on glacier ablation under a layer of debris cover, *J. Japan. Soc. Snow Ice (Seppyo)*, 39, 20–21, 1977.
- Gardelle, J., Berthier, E., and Arnaud, Y.: Slight mass gain of Karakoram glaciers in the early twenty-first century, *Nat. Geosci.*, 5, 322–325, 2012.
- Gardelle, J., Berthier, E., and Arnaud, Y.: Region-wide glacier mass balances over the Pamir-Karakoram-Himalaya during 1999–2011, *The Cryosphere*, 7, 1263–1286, 2013.
- Gardner, A. S., Sharp, M. J., Koerner, R. M., Labine, C., Boon, S., Marshal, S. J., Burgess, D. O., and Lewis, E.: Near-surface temperature lapse rates over Arctic glaciers and their implications for temperature downscaling, *J. Climate*, 22, 4281–4298, 2009.
- Granger, R. J., Pomeroy, J. W., and Parviainen, J.: Boundary layer integration approach to advection of sensible heat to a patchy snow cover, 59th Eastern Snow Conference, Stowe, Vermont, 2002.
- Han, H. D., Ding, Y. J., and Liu, S. Y.: A simple model to estimate ice ablation under a thick debris layer, *J. Glaciol.*, 52, 528–536, 2006.
- Hewitt, K.: The Karakoram anomaly? Glacier expansion and the “elevation effect” Karakoram Himalaya, *Mt. Res. Dev.*, 25, 332–340, 2005.
- Hewitt, K.: Glacier change, concentration, and elevation effects in the Karakoram Himalaya, Upper Indus Basin, *Mt. Res. Dev.*, 31, 188–200, 2011.

- Inoue, J. and Yoshida, M.: Ablation and heat exchange over the Khumbu Glacier, *J. Japan. Soc. Snow Ice (Seppyo)*, 39, 7–14, 1980.
- Kääb, A., Berthier, E., Nuth, C., Gardelle, J., and Arnaud, Y.: Contrasting patterns of early twenty-first-century glacier mass change in the Himalayas, *Nature*, 488, 495–498, 2012.
- Kayastha, R. B., Takeuchi, Y., Nakawo, M., and Ageta, Y.: Practical prediction of ice melting beneath various thickness of debris cover on Khumbu Glacier, Nepal using a positive degree-day factor, *Symposium at Seattle 2000 – Debris-Covered Glaciers, IAHS Publ.*, 264, 71–81, 2000.
- Kraus, H.: An energy-balance model for ablation in mountainous areas, *Snow and Ice-Symposium-Neiges et Glaces, August 1971, IAHS-AISH PUBLICATION no. 104*, 1975.
- Lejeune, Y., Bertrand, J.-M., Wagnon, P., and Morin, S.: A physically based model of the year-round surface energy and mass balance of debris-covered glaciers, *J. Glaciol.*, 59, 327–344, 2013.
- Loomis, S. R.: Morphology and ablation processes on glacier ice, *Assoc. Am. Geogr. Proc.*, 2, 88–92, 1970.
- Marshall, S. J., Sharp, M. J., Burgess, D. O., and Anslow, F. S.: Surface temperature lapse rate variability on the Prince of Wales Ice-eld, Ellesmere Island, Canada: implications for regional-scale downscaling of temperature, *Int. J. Climatol.*, 27, 385–398, 2007.
- Mattson, L. E., Gardner, J. S., and Young, G. J.: Ablation on debris covered glaciers: an example from the Rakhiot Glacier, Punjab, Himalaya, *Snow and Glacier Hydrology, IAHS-IASH Publ.*, 218, 289–296, 1993.
- Mölg, T., Cullen, N. J., Hardy, D. R., Kaser, G., and Klok, E. J.: Mass balance of a slope glacier on Kilimanjaro and its sensitivity to climate, *Int. J. Climatol.*, 28, 881–892, 2008.
- Mölg, T., Cullen, N. J., Hardy, D. R., Winkler, M., and Kaser, G.: Quantifying climate change in the tropical midtroposphere over East Africa from glacier shrinkage on Kilimanjaro, *J. Climate*, 22, 4162–4181, 2009.

- Mölg, T. and Kaser, G.: A new approach to resolving climate–cryosphere relations: downscaling climate dynamics to glacier-scale mass and energy balance without statistical scale linking, *J. Geophys. Res.*, 116, D16101, doi:10.1029/2011JD015669, 2011.
- Mölg, T., Maussion, F., Yang, W., and Scherer, D.: The footprint of Asian monsoon dynamics in the mass and energy balance of a Tibetan glacier, *The Cryosphere*, 6, 1445–1461, 2012a.
- Mölg, T., Großhauser, M., Hemp, A., Hofer, M., and Marzeion, B.: Limited forcing of glacier loss through land-cover change on Kilimanjaro, *Nat. Clim. Change*, 2, 254–258, 2012b.
- Mölg, T., Maussion, F., and Scherer, D.: Mid-latitude westerlies as a driver of glacier variability in monsoonal High Asia, *Nat. Clim. Change*, 4, 68–73, 2013.
- Nakawo, M. and Young, G. J.: Field experiments to determine the effect of a debris layer on ablation of glacier ice, *Ann. Glaciol.*, 2, 85–91, 1981.
- Nicholson, L. and Benn, D.: Calculating ice melt beneath a debris layer using meteorological data, *J. Glaciol.*, 52, 463–470, 2006.
- Nicholson, L. and Benn, D.: Properties of natural supraglacial debris in relation to modelling sub-debris ice ablation, *EPSL*, 38, 490–501, 2012.
- Niu, G.-Y., Yang, Z.-L., Mitchell, K. E., Chen, F., Ek, M. B., Barlage, M., Kumar, A., Manning, K., Niyogi, D., Rosero, E., Tewari, M., and Youlong, X.: The community Noah land surface model with multiparameterization options (Noah-MP): 1. Model description and evaluation with local-scale measurements, *J. Geophys. Res.*, 116, D12109, doi:10.1029/2010JD015139, 2011.
- Østrem, G.: Ice melting under a thin layer of moraine, and the existence of ice cores in moraine ridges, *Geogr. Ann.*, 41, 228–230, 1959.
- Petersen, L. and Pellicciotti, F.: Spatial and temporal variability of air temperature on a melting glacier: atmospheric controls, extrapolation methods and their effect on melt modeling, *Juncal Norte Glacier, Chile*, *J. Geophys. Res.*, 116, D23109, doi:10.1029/2011JD015842, 2011.

- Pfeffer, W. T., Arendt, A., Bliss, A., Bolch, T., Cogley, J. G., Gardner, A. S., Hagen, J.-O., Hock, R., Kaser, G., Kienholz, C., Miles, E. S., Moholdt, G., Mölg, N., Paul, F., Radic, V., Rastner, P., Raup, B. H., Rich, J., and Sharp, M. J.: The Randolph Glacier Inventory: a globally complete inventory of glaciers, *J. Glaciol.*, 221, 537–552, 2014.
- Radić, V. and Hock, R.: Regionally differentiated contribution of mountain glaciers and ice caps to future sea-level rise, *Nat. Geosci.*, 4, 91–94, 2011.
- Reid, T. D. and Brock, B. W.: An energy-balance model for debris-covered glaciers including heat conduction through the debris layer, *J. Glaciol.*, 56, 903–916, 2010.
- Reid, T. D., Carenzo, M., Pellicciotti, F., and Brock, B. W.: Including debris cover effects in a distributed model of glacier ablation, *J. Geophys. Res.*, 117, D18105, doi:10.1029/2012JD017795, 2012.
- Reznichenko, N., Davies, T., Shulmeister, J., and McSaveney, M.: Effects of debris on ice-surface melting rates: an experimental study, *J. Glaciol.*, 56, 384–394, 2010.
- Scherler, D., Bookhagen, B., and Strecker, M. R.: Spatially variable response of Himalayan glaciers to climate change affected by debris cover, *Nat. Geosci.*, 4, 156–159, 2011.
- Skamarock, W. C. and Klemp, J. B.: A time-split nonhydrostatic atmospheric model for weather research and forecasting applications, *J. Comput. Phys.*, 227, 3465–3485, 2008.
- Takeuchi, Y., Kayastha, R. B., and Nakawo, M.: Characteristics of ablation and heat balance in debris-free and debris-covered areas on Khumbu glacier, Nepal Himalayas, in the pre-monsoon season, in: *Debris-covered glaciers*, IAHS Publ., 264, 53–61, 2000.
- Takeuchi, Y., Kayastha, R. B., Naito, N., Kadota, T., and Izumi, K.: Comparison of meteorological features in the debris-free and debris-covered areas at Khumbu Glacier, Nepal Himalayas, in the premonsoon season, 1999, *Bull. Glaciol. Res.*, 18, 15–18, 2001.
- Treydte, K. S., Schleser, G. H., Helle, G., Frank, D. C., Winiger, M., Haug, G. H., and Esper, J.: The twentieth century was the wettest period in northern Pakistan over the past millennium, *Nature*, 440, 1179–1182, 2006.

Yadav, R. R., Park, W.-K., Singh, J., and Dubey, B.: Do the western Himalayas defy global warming? *Geophys. Res. Letts.*, 31, L17201, doi:10.1029/2004GL020201, 2004.

Zhang, Y., Fujita, K., Liu, S., Liu, Q., and Nuimura, T.: Distribution of debris thickness and its effect on ice melt at Hailuoguo glacier, southeastern Tibetan Plateau, using in situ surveys and ASTER imagery, *J. Glaciol.*, 57, 1147–1157, 2011.

Chapter 2

High-resolution interactive modelling of the mountain glacier–atmosphere interface: an application over the Karakoram

2.1 Introduction¹

Spatially-distributed simulations of glacier surface and climatic mass balance (where the latter term denotes surface plus near-subsurface mass balance following; Cogley et al., 2011) require distributed meteorological forcing; however, obtaining these data is complicated both by the spatial and temporal scarcity of in situ observations and by the “scale mismatch” between the spatial scales represented in atmospheric models and those relevant for surface and CMB calculations (e.g. Machguth et al., 2009; Mölg and Kaser, 2011). To overcome these issues, forcing data can be obtained by extrapolation from point measurements by automated weather stations, where available, or interpolation from climate reanalyses and atmospheric model output, using surface- and free-air lapse rates. Surface lapse rates exhibit significant spatial and temporal variability, however, leading to uncertainty in temperature downscaling from altitude changes

¹T. Mölg, F. Maussion, D. Scherer, C. Mayer, and A. B. G. Bush contributed to this chapter.

(Marshall et al., 2007; Gardner et al., 2009; Petersen and Pellicciotti, 2011). In addition, the assumption of linear lapse rates over glacier surfaces may be inappropriate (Petersen and Pellicciotti, 2011) and may under-predict near-surface temperature over debris-covered regions (Reid et al., 2012). Finally, additional corrections are often required for the poor representation of the strength and spatial variability of processes relevant to mass balance, such as orographic precipitation, in coarse spatial-resolution atmospheric models (e.g. Paul and Kotlarski, 2010; Radić and Hock, 2011).

Dynamical downscaling has been used to address the issue of spatial resolution in the most recent studies to produce climate data at horizontal resolutions of ~ 18 km (Machguth et al., 2009; Kotlarski et al., 2010a,b; Paul and Kotlarski, 2010), ~ 11 km (Van Pelt et al., 2012) and ~ 1 – 3 km grid spacings (Mölg and Kaser, 2011; Mölg et al., 2012a,b) as forcing for distributed alpine glacier surface- and climatic-mass-balance calculations. This approach provides high spatial- and high temporal-resolution atmospheric fields obtained from a physical model, and the increased resolution allows for improved representation of features such as complex topography and orographic precipitation (e.g. Maussion et al., 2011). However, most of these studies required statistical corrections to link mesoscale circulation patterns and meteorological fields simulated by regional atmospheric models to local conditions on the glacier surface. Mölg and Kaser (2011) first showed that, at sufficiently high spatial resolution (~ 1 km), a regional atmospheric model could be used to force explicit distributed simulations of glacier CMB without statistical corrections at the glacier–atmosphere interface. This approach has since been applied successfully in multiple locations for small glaciers (Mölg and Kaser, 2011; Mölg et al., 2012a,b).

Traditional approaches to simulations of surface and climatic mass balance, including those discussed above, have been one-way, or offline, in which meteorological fields are passed to the CMB model but changing surface boundary conditions due to CMB processes are not fed back into the atmospheric model. Interactively or two-way coupled atmospheric and ice-sheet simulations with simple treatments of ablation have been performed to estimate the paleoclimate and future climate behaviours of the Laurentide and Greenland ice sheets, respectively, with significant alterations to atmospheric circulation, temperature and precipitation resulting from ice sheet evolution (Ridley et al., 2005; Pritchard et al., 2008). Although an initial effort has

been made to include “interactive” alpine glaciers in a regional atmospheric model with the subgrid-scale parameterization of Kotlarski et al. (2010b), the influence of two-way coupling on the atmospheric forcing and explicitly simulated surface and climatic mass balance has yet to be assessed for alpine glaciers.

Here, we build on a new, unified and explicit approach to resolving the glacier–atmosphere interface without statistical downscaling (Mölg and Kaser, 2011), through the use of an interactively coupled high-resolution mesoscale atmospheric and physically based CMB modelling system. By allowing changes in glacier surface conditions to feed back on the atmospheric drivers, the model provides a consistent calculation of surface energy and mass fluxes. For the initial application of the coupled model, we simulate the Karakoram region of the Hindu Kush-Himalaya (Fig. 2.1), which is estimated to contain anywhere from $\sim 1250\text{--}4000\text{ km}^3$ of ice, covering an area of $\sim 18\,000\text{ km}^2$ (Bolch et al., 2012). Due to its extensive glaciation, this region presents a high potential influence on atmospheric simulations resulting from the inclusion of feedbacks from alpine glaciers. In addition, Yao (2007) estimates that more than half of the glacierized area is contained in the 15 largest glaciers, thus optimizing the Karakoram for representation in a high-resolution atmospheric model, where the smallest practical grid spacing is on the order of a few kilometers.

The Karakoram is also of interest due to recent evidence of stable or positive mass balances (e.g. Hewitt, 2005; Scherler et al., 2011a; Gardelle et al., 2012; Kääb et al., 2012), which contrasts with the general trend of mass loss exhibited by glaciers elsewhere in the Himalaya (Cogley, 2011). However, definitive statements about the mass balance of Karakoram glaciers have been hampered by a dearth of both in situ measurements and information on ice thickness changes. The latter limitation has been partially addressed by recent geodetic studies (Gardelle et al., 2012; Kääb et al., 2012) that support reduced mass loss or even a positive mass balance anomaly in the early 21st century but emphasize the spatial and temporal heterogeneity of recent glacier behaviour. In addition, explicit, physically based, spatially distributed numerical modelling has the potential to clarify the dynamics occurring in this region.

In this study, we first evaluate the regional and the local performance, respectively, of the coupled model against available measurements, by comparing the former with surface albedo

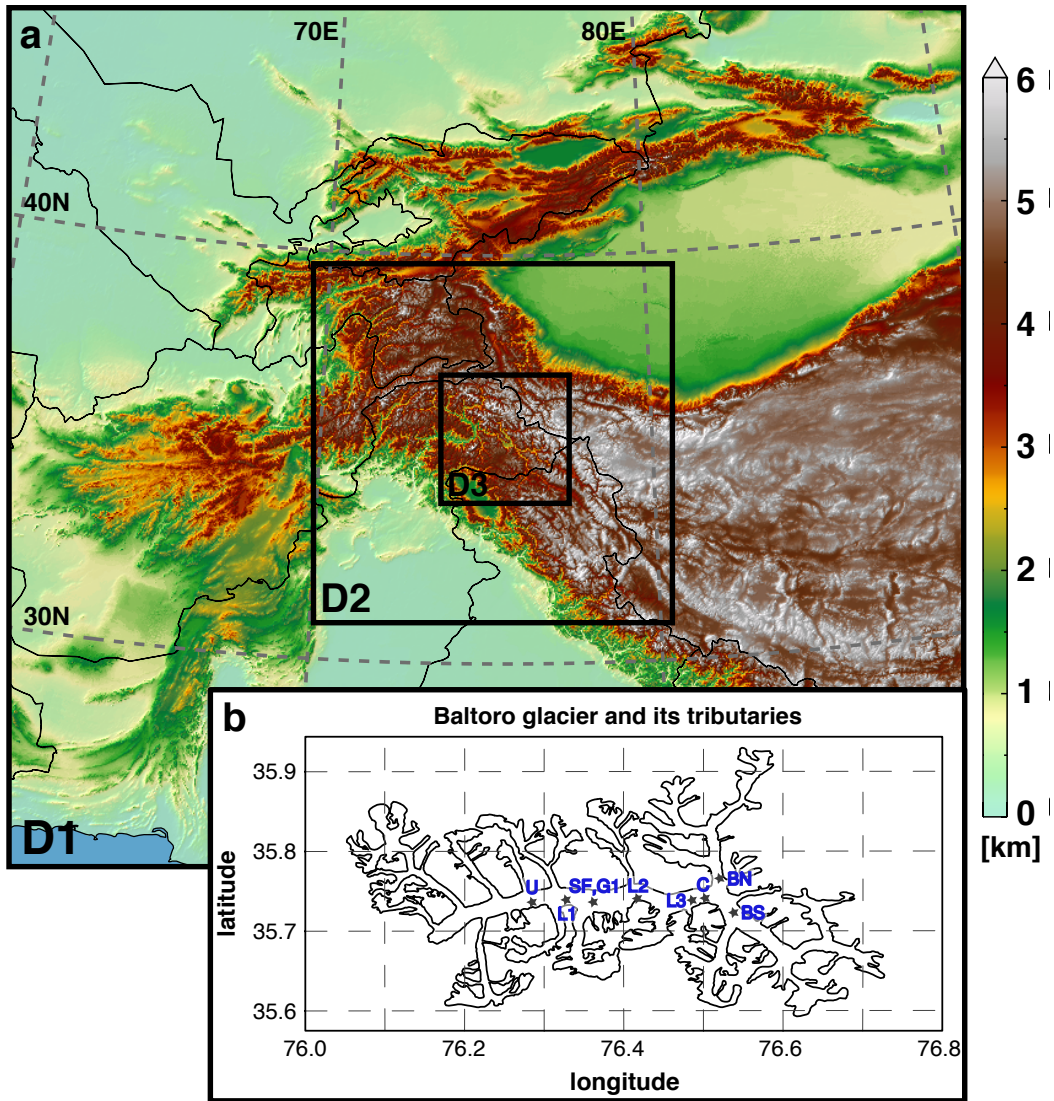


Figure 2.1: (a) WRF atmospheric model domains, configured with horizontal spatial resolutions of 33, 11, and 2.2 km. Terrain elevation from the GTOPO30 dataset is shaded in units of meters. (b) Outline of Baltoro glacier and its tributaries, which are included in WRF D3, with the mean stake locations labeled and denoted by stars.

and temperature over all glacier surfaces and the latter with meteorological fields and ablation on the Baltoro glacier. We then aim to (1) explore the importance of energy and mass exchanges between the glacier surface and boundary layer on the atmospheric forcing, and (2) assess the ultimate influence of interactive coupling on simulations of glacier mass balance. A final goal of this work is to improve the representation of alpine glaciers in mesoscale atmospheric models by introducing additional, relevant physical processes.

2.2 Methods

The coupled modelling system (hereafter “WRF-CMB”) consists of two components: the advanced research version of the nonhydrostatic and fully compressible Weather Research and Forecasting (WRF) mesoscale atmospheric model version 3.4 (Skamarock and Klemp, 2008, Sect. 2.2.1) and the process-based surface-energy and CMB model of Mölg et al. (2008, 2009, 2012a, Sect. 2.2.2). The CMB model has been incorporated into the WRF source code as an additional physics option, and, thus, the user may select via runtime (“namelist”) options whether the CMB simulation is offline (conventional one-way forcing, with feedbacks only from WRF’s land surface model) or interactive (feedback from CMB model to WRF over glacierized grid cells; Sect. 2.2.3). We performed two simulations, one interactive (INT) and one offline (OFF), for the months of June–August 2004, to coincide with a limited number of glaciological and meteorological measurements from the Baltoro glacier available for evaluation (Sect. 2.2.4), with the period of 1–25 June discarded as model spin-up time. Here we use the term interactive to denote surface–atmosphere exchanges through heat, moisture and momentum fluxes only and not through topographic feedbacks, as glacier geometry is held constant over our brief simulation. As a first approximation, we focused on the meteorologically driven fluctuations of mass balance and neglected the influence of debris cover.

2.2.1 Mesoscale atmospheric model

For these simulations, WRF was configured with three nested domains of 33, 11 and 2.2 km spatial resolution, centered over the Karakoram (D1–3; Fig. 2.1). By increasing the spatial resolution over the region of interest, the use of multiple grid nesting improves the representation

of complex terrain and associated processes such as orographic precipitation, and has been found to increase the simulation skill of WRF for mountain summit conditions (Mölg and Kaser, 2011). Model physics and other settings were selected following the recommendations of the National Center for Atmospheric Research (NCAR) for regional climate simulations with WRF (Table 2.1; outlined in WRF ARW user’s guide). Note that no cumulus parameterization was employed in the highest-resolution, convection-permitting model domain, WRF D3 (e.g. Molinari and Dudek, 1992; Weisman et al., 1997). The range of terrain elevation represented in this domain at 2.2 km resolution is 916 to 7442 m a.s.l., which encompasses the most heavily glacierized altitudes in the Karakoram (\sim 2700–7200 m, as shown in Fig. S2 of Bolch et al. (2012), with the mean basin-wide glacier elevation located at 5326 m).

In this study, WRF was coupled with the Noah land surface model (LSM; Chen and Dudhia, 2001). The land-ice mask was updated using glacier outlines for the Karakoram region based on the glacier inventory of China (Shi et al., 2009) as well as inventories generated by ICIMOD (2007) and GlobGlacier (Frey et al., 2012). Other modifications made to glacierized grid cells included assigning (1) zero vegetation cover, (2) maximum and minimum albedo values consistent with the parameterization in the CMB model (Sect. 2.2), and (3) a soil moisture availability of 1.0 (from an original value of 0.95). The conventional bulk computation of the latent heat flux in the WRF surface module is multiplied by the last parameter; therefore, this change was made for consistency with the CMB model.

The atmospheric model was forced with ERA-Interim data at $0.75^\circ \times 0.75^\circ$ spatial-resolution and 6-hourly temporal-resolution, as provided by the European Centre for Medium-Range Weather Forecasts (ECMWF; Dee et al., 2011). In the ERA-Interim reanalysis, snow depth is arbitrarily set to 10 m in the analysis for grid cells with greater than 50% glacier coverage (Paul Berrisford, personal communication, 2012), which results in unphysical snow depths over the Karakoram. We therefore obtained an initial snow condition from the microwave-derived Global EASE-Grid 8-day Blended SSM/I and MODIS Snow Cover SWE data (Brodzik et al., 2007), by assuming a snow density of 300 kg m^{-2} and assigning an initial depth of 2 m over large glaciers where these data are missing (less than 0.1% (8 in total) of data points in the region spanned by WRF D1).

Table 2.1: WRF configuration.

Model domains	
Horizontal grid spacing	33, 11, 2.2 km (domains 1–3)
Time step	60, 20, 4 s
Vertical levels	40
Height of lowest model level	~ 20 m
Model top pressure	25 hPa
Model physics	
Radiation	CAM
Microphysics	Thompson
Cumulus	Kain–Fritsch (none in D3)
Atmospheric boundary layer	Yonsei University
Surface layer	Monin–Obukhov (revised MM5)
Land surface	Noah version 3.1
Dynamics	
Top boundary condition	w-Rayleigh damping
Horizontal advection	Explicit 6th order coeff: 0.12, 0.12, 0.36
Lateral boundaries	
Specified boundary width	10 grid points
Relaxation exponent	0.33
Forcing	ERA Interim, $0.75^\circ \times 0.75^\circ$ updated 6-hourly

WRF employs a terrain-following hydrostatic-pressure coordinate in the vertical, defined as eta (η) levels (Skamarock and Klemp, 2008). For these simulations, the lowest atmospheric model level was specified at $\eta = 0.997585$ (~ 20 m) to maintain the validity of the constant-flux assumption in the bulk computation of the turbulent heat fluxes, as the surface mid-layer height (less than 10 m) is used in the calculation following the approach of the Noah LSM. We selected the recently revised Monin–Obukhov surface layer (Jiménez et al., 2012), which was found to improve the simulation of the diurnal amplitudes of near-surface meteorological fields over complex terrain with a horizontal spatial resolution of 2 km. We also used positive-definite explicit 6th order diffusion (Kniewel et al., 2007), in order to dampen grid-scale noise in the atmospheric fields and because Mölg and Kaser (2011) found this option improved the simulated magnitude of precipitation at high elevations on Kilimanjaro. For the simulations presented here, we selected the default value of the diffusion coefficient (0.12) for all model domains except D3, for which we used a value of 0.36. The choice of the diffusion parameter value is uncertain; sensitivity runs revealed that increasing the strength increased simulated precipitation at high elevations, which may be attributable to increased diffusive transport, with the best agreement with the Urdukas AWS data found for the selected value.

2.2.2 Surface energy and climatic mass balance model

The CMB model is described fully by Mölg et al. (2008, 2009) with the most recent updates in Mölg et al. (2012a), but we will review some important features here. The model computes the column specific mass balance from solid precipitation, surface deposition and sublimation, surface and subsurface melt, and refreeze of both meltwater and liquid precipitation. To determine the mass fluxes, the model first solves the surface energy balance equation:

$$S\downarrow \cdot (1 - \alpha) + L\downarrow + L\uparrow + QS + QL + QG + QPRC = F_{\text{NET}} \quad (2.1)$$

in which the terms correspond to, from left to right: incoming short-wave radiation, broadband albedo, incoming and outgoing long-wave radiation, turbulent fluxes of sensible and latent heat, ground heat flux and heat flux from precipitation. The ground heat flux, QG, consists of a conductive component (QC) as well as a component due to subsurface penetration of short-wave radiation (QPS). The net flux, F_{NET} , represents the energy available for melt, QM, provided

Table 2.2: MB model configuration.

Vertical levels (14)	0, 0.1, 0.2, 0.3, 0.4, 0.5, 0.8, 1, 1.4, 2, 3, 5, 7, 9 m
Fresh snow density	250 kg m ⁻²
Ice density	900 kg m ⁻²
<hr/>	
Albedo scheme parameters	Mölg et al. (2012a)
<hr/>	
Ice albedo	0.30
Firn albedo	0.55
Fresh snow albedo	0.85
Time scale	6.0 days
Depth scale	8.0 cm

the surface temperature is at the melting point, $T_M = 273.15$ K.

The model treats both surface and subsurface processes, including surface albedo and roughness evolution based on snow depth and age; snowpack compaction and densification by refreeze; and the influence of penetrating solar radiation, refreeze and conduction on the englacial temperature distribution. The CMB model is forced by air temperature, humidity, wind speed, and air pressure, all of which were taken from the lowest model level ($z = 20$ m). Note that the diagnostically updated 2 and 10 m meteorological fields were not used as forcing so as to (1) be consistent with the approach of the Noah LSM (Chen and Dudhia, 2001), and (2) prevent decoupling of the atmosphere and land surface, wherein the lower atmosphere is no longer influenced by surface conditions. The CMB model also takes as input: total precipitation and its frozen fraction; incoming short- and long-wave radiation; and time between snowfall events. Some model parameter values are provided in Table 2.2. The initial subsurface temperature was specified through linear interpolation of the input data to the Noah LSM, available at 0.1, 0.4, 1.0, and 2.0 m depths, and assigning a constant value of 268.6 K below this level. The lower boundary is specified at 268.6 K during the simulation, based on measurements taken from a Tibetan glacier (Mölg et al., 2012a). We address uncertainties in the subsurface temperature initialization by including a long (25 day) model spin-up period.

2.2.3 Coupling architecture

For both offline and interactive simulations, the CMB model calculates glacier surface-energy and surface- and near-surface-mass fluxes among other variables at every time step (e.g. every 4 s in D3) over glacierized grid cells, while the Noah LSM values are retained over non-glacierized grid cells. The integrated modelling approach permits some advantages in the CMB model's forcing strategy. For example, topographic shading, incoming short- and long-wave radiation, and the fraction of frozen precipitation are now obtained from the atmospheric model's surface, radiation, and microphysics modules, respectively. Another important advantage is that WRF provides high-resolution, dynamically derived, and spatially distributed forcing data without the need for traditional statistical methods, such as those mentioned in Sect. 2.1. The incorporation of the CMB model for all glacier grid points in the coupled model adds negligible computational expense to WRF simulations.

For interactive simulations, the CMB model updates over glacierized areas in WRF, at every time step: (1) surface heat and moisture fluxes, (2) surface and subsurface (including deep soil) temperature, (3) snow depth, water equivalent and fractional cover, (4) surface albedo and roughness, and (5) surface specific humidity. The inclusion of feedbacks represents a more consistent approach, as it permits the near-surface forcing variables to be modified by exchanges of mass, momentum and moisture between the glacier and the atmospheric surface layer. In this study, the CMB model output accumulated energy and mass fluxes every hour that were then converted into hourly averages for analysis; these data will be referred to as “hourly”.

As indicated at the beginning of Sect. 2.2, it is not absolutely correct to label the two forcing approaches as “offline” and “interactive” because the atmospheric model currently receives surface feedbacks through the Noah LSM. There have been recent efforts to improve the simulation of snow processes in WRF, such as with the introduction of the Noah-MP land surface parameterization (Niu et al., 2011), which, for example, introduces separate vegetation canopy and surface layers and the possibility of multiple vertical layers in the snowpack. However, the simplified treatment of glacier grid cells in the Noah LSM is retained. Thus, by incorporating the CMB model, we are able to simulate more physical processes relevant for glaciers, such as refreezing of meltwater in the snowpack, englacial melt, and formation of superimposed ice.

Other improvements to the treatment of snow and ice physics, compared with the Noah LSM, include introducing multiple layers in the snowpack, increasing the column depth from 2 to 9 m, consideration of snow porosity, and allowing for full snowpack ablation to expose bare ice. The latter point is especially critical, as the Noah LSM imposes minimum snow depth and water equivalent values over land-ice grid cells.

2.2.4 Measurements for model evaluation

In Sect. 2.3.2, we compare the coupled model results with a limited number of available ablation stake measurements as well as automated weather station (AWS) data that were acquired in summer 2004 on the Baltoro glacier ($35^{\circ} 35' - 35^{\circ} 56' \text{ N}$, $76^{\circ} 04' - 76^{\circ} 46' \text{ E}$; Mihalcea et al., 2006). The glacier is approximately 62 km long, with an average (maximum) width of 2.1 (3.1) km (Mayer et al., 2006). Therefore, in WRF-CMB the Baltoro glacier is represented by at least one grid point in the along-glacier direction and we resolve longitudinal rather than transverse gradients in surface conditions. We use data from 6 sections (SF, U, G1, C, BN, and BS) as well as from longitudinal transects along the glacier (L1, L2 and L3), comprising 53 stakes in total that provide sufficient spatial coverage (cf. Fig. 2.1b) to evaluate both the spatial pattern and the magnitude of ablation in the coupled model applied to the Baltoro glacier. The ablation measurements were taken at different intervals between 1–15 July 2004; a brief summary of the location and other details of the stake measurements are given in Table 2.3 (a more detailed description of the data can be found in Mihalcea et al., 2006). While the data represent a brief period, they provide the only available direct ablation measurements in the Karakoram. For the comparison, total simulated surface lowering was interpolated to the mean location of the stake section or transect using inverse distance weighting.

The AWS was situated adjacent to the glacier on a moraine ridge at an elevation of 4022 m ($35^{\circ} 43.684' \text{ N}$, $76^{\circ} 17.164' \text{ E}$) and provided hourly mean data after 18 June 2004 (Mihalcea et al., 2006). We compared these data with WRF data from the nearest model grid point (located at an elevation of 4322 m), which was also non-glacierized and therefore was more consistent in the land surface type. However, the data therefore do not include direct feedbacks from the CMB model. Note that the assumptions discussed in Sect. 2.2.1 for snow initialization were not

Table 2.3: Summary of available ablation stake measurements from the Baltoro glacier.

Stake section (Symbol) [Num. Stakes]	Measurement period (2004)	Mean location	Mean elevation (m a.s.l.)
Urdukas (U) [4]	2–15 July	76.285° E, 35.737° N	3993 [WRF: 4202]
Longitudinal Sect. 1 (L1) [2]	3–14 July	76.328° E, 35.740° N	4120 [WRF: 4201]
Stake Farm (SF) [23]	4–14 July	76.362° E, 35.737° N	4177 [WRF: 4262]
Gore 1 (G1) [4]	4–13 July	76.364° E, 35.739° N	4182 [WRF: 4303]
Longitudinal Sect. 2 (L2) [4]	5–12 July	76.418° E, 35.742° N	4308 [WRF: 4347]
Longitudinal Sect. 3 (L3) [2]	8–11 July	76.486° E, 35.739° N	4470 [WRF: 4601]
Concordia (C) [5]	8–11 July	76.502° E, 35.742° N	4537 [WRF: 4622]
Baltoro South (BS) [5]	7–11 July	76.538° E, 35.724° N	4634 [WRF: 4704]
Baltoro North (BN) [4]	8–11 July	76.520° E, 35.766° N	4646 [WRF: 4760]

applied over the stake sites on the main glacier area (cf. Fig. 2.1b).

To supplement these field measurements, we also evaluate in Sect. 2.3.1 the basin-scale performance of the coupled model using MODIS/Aqua (1) MYD10A1 daily snow albedo available at 500 m resolution, and (2) MYD11A2 eight-day land surface temperature available at 1 km resolution, with daily data obtained by averaging day- and night-time temperatures where both fields were available and were assigned the highest quality assurance flag for MODIS products. Due to the prevalence of missing data in the snow albedo dataset, we considered only the grid cells with at least 25% valid observations during the 67 day period for comparison with WRF. Both MODIS datasets were re-projected to the WRF D3 grid before completing the analysis.

2.3 Results and discussion

We first compare our simulated results with remote sensing data (Sect. 2.3.1) and with meteorological and glaciological measurements from the Baltoro glacier (Sect. 2.3.2). The role of interactive coupling on the atmospheric forcing data and on simulations of CMB will then be discussed. Results are presented from the finest-resolution atmospheric model domain only, since it provides the most realistic terrain representation.

2.3.1 Remote sensing data

Figure 2.2 presents a comparison between WRF-CMB and the MODIS/Aqua datasets discussed in Sect. 2.2.4. The elevational profile of land surface temperature (LST) averaged over the simulation period produced by the CMB model is in good agreement with the MODIS data above ~ 5200 m and is an improvement on the Noah LSM values at all resolved elevations (Fig. 2.2a). The strong divergence of modelled and observed LST below 5200 m likely results from neglecting debris cover, since its presence allows the glacier surface to be warmed by solar radiation above the melting point. Supraglacial debris extent has also been found to increase with distance down glacier in remote-sensing case studies of the central Karakoram (e.g. Scherler et al., 2011a). Specific to the Baltoro glacier and its tributaries, Mayer et al. (2006) found that debris coverage increased to 70–90 % of the glacier area below 5000 m, with 100 % coverage found below the U site (Fig. 2.1b). A time-series analysis of LST, averaged only over elevations greater than 5200 m is presented in Fig. 2.2c. The CMB model gives an improved performance over the LSM alone, although LST is generally under-predicted, with mean biases of -1.0 , -1.3 , and -6.1 K in the INT, OFF, and Noah LSM simulations, respectively. Conversely, snow albedo in WRF-CMB is in good agreement with MODIS below ~ 5200 m (Fig. 2.2b), although simulated values are constrained by the lower bound of $\alpha_{\text{ice}} = 0.3$ as snow depth goes to zero and, thus, slightly overestimate the observational values at the lowest elevations. Above 5200 m, WRF-CMB over-predicts snow albedo compared with MODIS. However, it produces values and an altitudinal gradient that are in much better agreement with observations than the Noah LSM.

The strong discrepancy between Noah LSM and MODIS data is in part related to the treatment of grid cells defined as glacial ice: the LSM in WRF v3.4 imposes minimum values of snow depth and water equivalent of 0.5 and 0.1 m, respectively, thus preventing the exposure of bare ice or debris and the associated lowering of surface albedo. In addition, the Noah LSM employs a time-decaying snow albedo formulation (based on the scheme of Livneh et al., 2009) and determines surface albedo using fractional snow cover to correct a background snow-free albedo. Although snow albedo is likewise an exponential function of age in the CMB model (following Oerlemans and Knap, 1998), the actual surface albedo also depends on snow depth to account for surface darkening when the snowpack is thin. It is clear from Fig. 2.2 that this

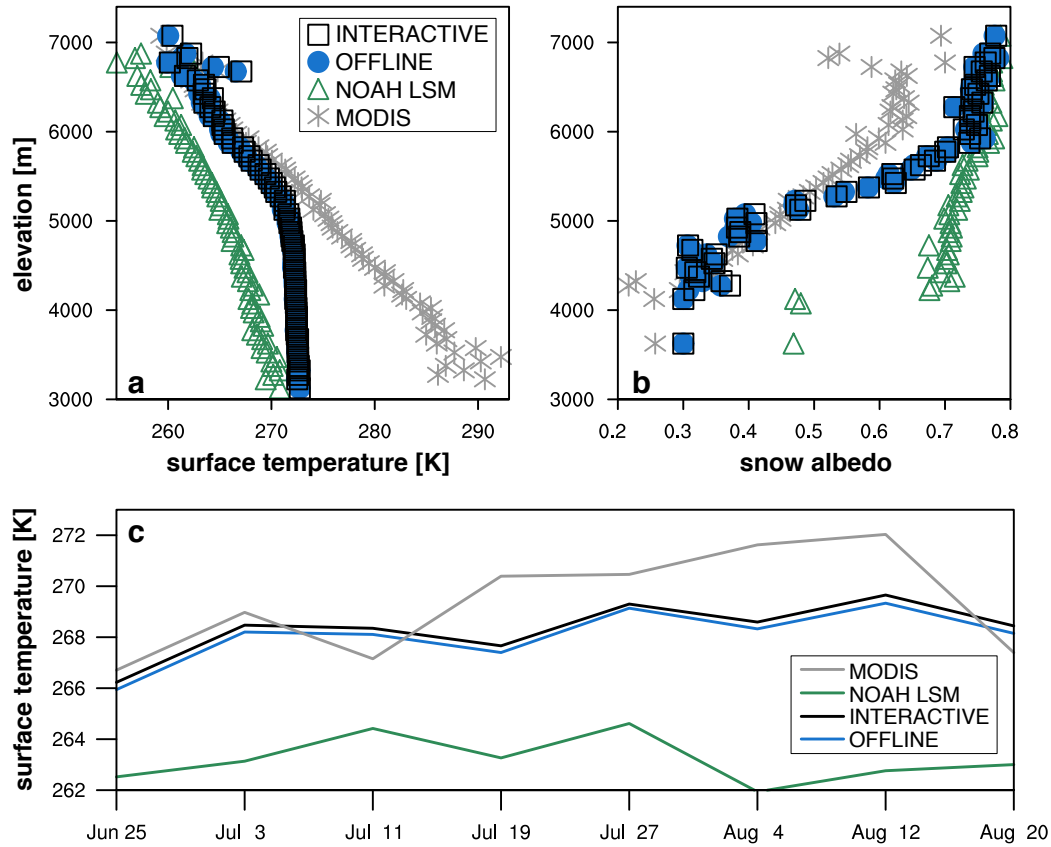


Figure 2.2: Comparison between WRF-CMB D3, Noah LSM, and MODIS for land surface temperature, (a) averaged from 25 June–28 August 2004, and in 50 m elevation bins; (c) the mean time series above 5200 m elevation; and for (b) snow albedo, averaged between 25 June–31 August 2004, over glacier grid cells where at least 25% of the daily times are available.

formulation, in combination with permitting snow-free conditions, gives more realistic values.

The evaluation of modelled albedo is sensitive to the simulated timing of snowfall events for both models, due to the nature of the parameterization schemes, and is limited by the large number of missing data in MODIS. In addition, comparison is hindered by the fact that the MODIS daily albedo product is not a daily-averaged quantity (as the simulated data are) but rather a collection of pixels with the highest quality from that day for which acquisition time is not trivial to retrieve (Stroeve et al., 2006). Finally, the small positive biases in snow albedo below ~ 4300 m and the negative biases in LST are both physically consistent with neglecting the influence of debris cover in WRF-CMB, as will be discussed further in Sect. 2.3.4.

2.3.2 Baltoro glacier

Figure 2.3 presents a time series of modelled and observed near-surface meteorological data from the Urdukas AWS that is situated adjacent to the Baltoro glacier. WRF-CMB is skillful in simulating air temperature at 2 m, and its evolution over the study period, including capturing periods of reduced diurnal variability at the beginning and between 30 July and 6 August. However, the good agreement in near-surface temperature despite a difference in real and modelled elevation of ~ 300 m (4022 vs. 4322 m a.s.l., respectively) suggests that there is a positive temperature bias in WRF-CMB at this grid point. The greatest contributing factor is higher incoming short-wave radiation: averaged over the simulation period, the surface in INT receives an additional 112 W m^{-2} of radiation than measured by the AWS (not shown). The discrepancy is most likely due to insufficient simulated cloud cover and humidity (Fig. 2.3b), with a potential contribution also from the computation of topographic shading at 2.2 km resolution. Finally, the amplitude of the diurnal temperature cycle is smaller in WRF-CMB, which may be attributable to differing thermal properties of the real and modelled land surface or to the fact that the AWS sensor was not aspirated.

The magnitude of the near-surface wind speed is also in agreement with the AWS data (Fig. 2.3c). However, an important discrepancy is the underestimation of precipitation at this particular grid cell in both INT and OFF simulations: the AWS records a total of 122.8 mm of precipitation between 25 June and 31 August, while INT and OFF simulate 46.9 and 48.4 mm,

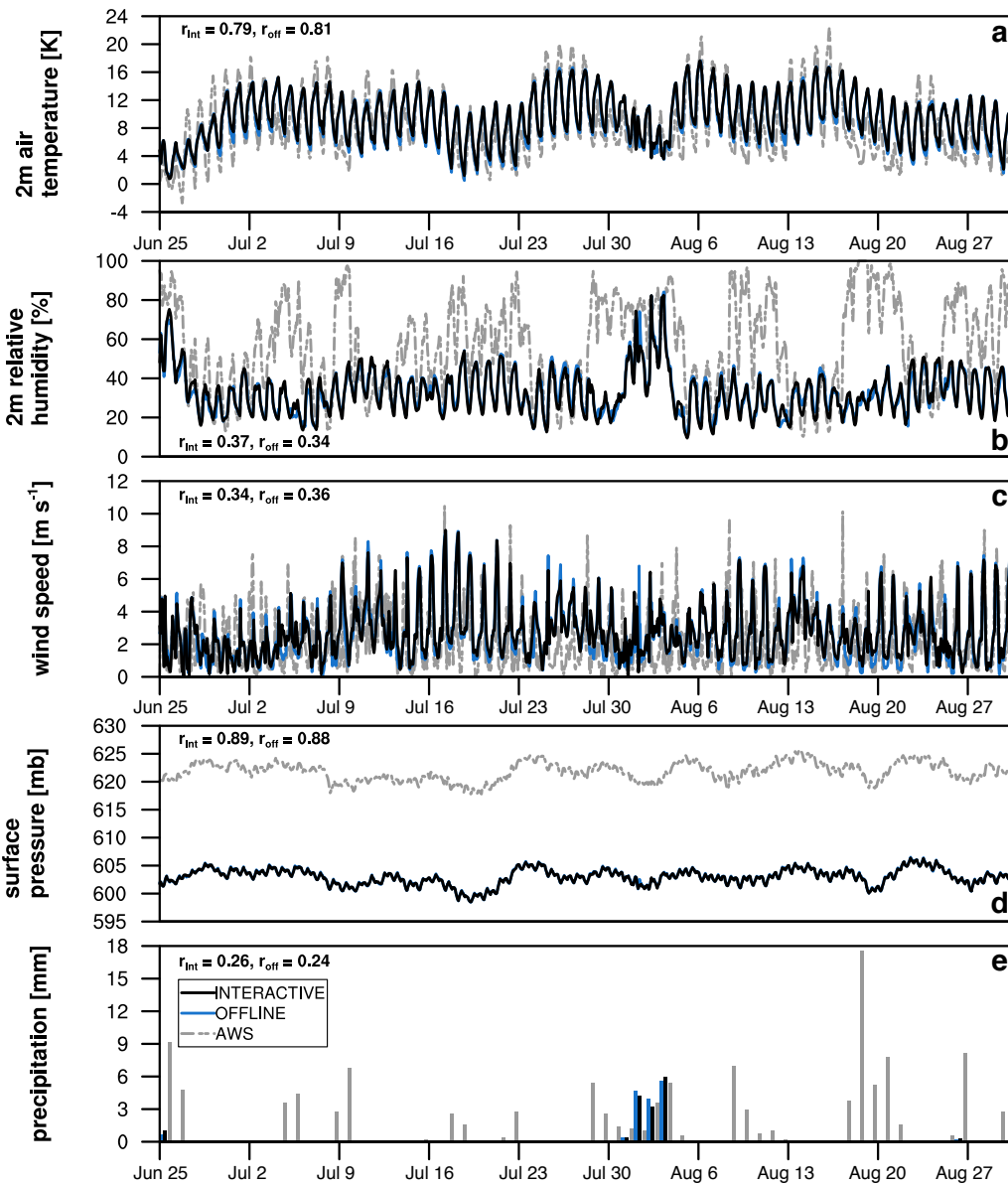


Figure 2.3: Hourly (a) air temperature at 2 m, (b) relative humidity at 2 m, (c) wind speed at 10 m, and (d) surface air pressure, as well as (e) daily total precipitation. Solid black (blue) curves display data from the interactive (offline) simulations while the dashed grey curve is the Urdukas AWS station data. Note the difference in elevation of the AWS (4022 m a.s.l.) and the terrain height in the closest WRF grid cell (4322 m).

respectively (Fig. 2.3e). Missing precipitation events are also reflected as discrepancies in the time series of relative humidity (cf. Fig. 2.3b, e) and are consistent with an overestimation of incoming short-wave radiation as a result of too little cloud cover. The disagreement in measured and simulated humidity and precipitation may reflect several sources of error, such as in the forcing data at the lateral boundaries. In addition, the spatial resolution of WRF D3 may be insufficiently fine to fully resolve orographic uplift or microscale complex flow features that affect precipitation at the AWS. Furthermore, we do not use a cumulus parameterization in the finest model domain and therefore assume that convection is explicitly resolved. However, previous studies indicate that a grid spacing on the order of 100 m (Bryan et al., 2003; Petch, 2006) or even 10 m (Craig and Dörnback, 2008) is needed to capture the dominant length scales of moist cumulus convection. A final potential error source is the difference in the land surface type adjacent to the AWS and model grid cell: the Baltoro glacier is debris-covered at the Urdukas site, while WRF-CMB has a clean snow/ice surface. The differing thermal properties of the adjacent surface area, specifically the limiting of temperature at the melting point in WRF-CMB, may also contribute to differences in localized convection.

WRF-CMB produces 40 to 80 cm of ablation along the main body of the Baltoro glacier between 1–15 July 2004 (Fig. 2.4a). Spatial comparison of the two simulations reveals only small differences, generally on the order of a few centimetres, consistent with the short nature of the study period (Fig. 2.4b). There are slightly positive anomalies at lower elevations, corresponding to less ablation in INT; conversely, there are negative anomalies at higher elevations, corresponding to more ablation in INT. Total simulated ablation is in order-of-magnitude agreement with measurements (Fig. 2.4c); however, the model overestimates ablation at all sites, in part because it does not capture four all-phase precipitation events, amounting to 17.6 mm, during the measurement period (cf. Fig. 2.3e). In comparing daily simulated/measured ablation rates and mean debris thickness (Table 2.4), the rates tend to be in better agreement for sites with thinner mean debris cover (SF, L2, L3, C) and more strongly overestimated by WRF-CMB where supraglacial debris is thicker (U, L1, G1, BN, BS). Although differences between INT and OFF are small, INT is in closer agreement with observations at all but one site (BN, as a result of less simulated refreeze than in OFF), with the strongest improvement at BS. The

Table 2.4: Ablation rates (cm day^{-1}) and debris thickness on the Baltoro glacier.

Site	INT	OFF	Average measured (ice)	Mean debris thickness (cm)
U	-5.6	-5.5	-3.9	8.6
L1	-5.4	-5.3	-3.5	7.0
SF	-5.2	-5.1	-4.3	3.8
G1	-5.2	-5.1	-2.9	18.0
L2	-5.1	-5.1	-4.8	2.5
L3	-5.0	-4.9	-4.3	2.0
C	-4.9	-4.9	-2.9	6.0
BS	-6.4	-5.6	-1.8	6.8
BN	-7.4	-7.7	-1.8	7.8

improvement at this site stems from faster complete snow cover removal (~ 1 day earlier in INT), which reduces subsurface penetration of short-wave radiation and, thus, subsurface melt production. Finally, the overestimation of ablation by WRF-CMB tends to diminish as the observation period increases (not shown), which suggests that the coupled model as configured in this study may be best suited for “climatological” simulations of glacier mass balance due to its sensitivity to the timing of precipitation.

Mihalcea et al. (2008) performed distributed surface-energy sub-debris melt modelling, using the Urdukas AWS data as forcing for the same study period. The authors determined debris extent, thickness and thermal properties from satellite imagery, and considered only the elevation range of 3650–5400 m a.s.l., which gives a corresponding glacier area of 124 km^2 . Mihalcea et al. (2008) computed 0.058 km^3 w.e. of ablation, or a mean surface lowering of 0.47 m between 1–15 July, which was found to be a slight underestimation (on average, -0.016 m) of the observed ablation rates at the SF site. For comparison, INT and OFF simulate 0.069 and 0.070 km^3 w.e. of surface melt, respectively, over an area of 126 km^2 that produces an average thickness change of approximately -0.55 m . The actual CMB calculation in the model also includes additional processes, such as snowpack ablation and surface vapour fluxes, that bring the total simulated mass loss to 0.078 km^3 w.e. between 1–15 July. We employ the same glacier outline, that of Mayer et al. (2006); however, discrepancies in our estimates may arise from its projection to the WRF D3 grid, differences in removal of tributary glaciers, and the coarser representation of the Baltoro glacier at 2.2 km spatial resolution (vs. 90 m in Mihalcea et al., 2008). Despite these

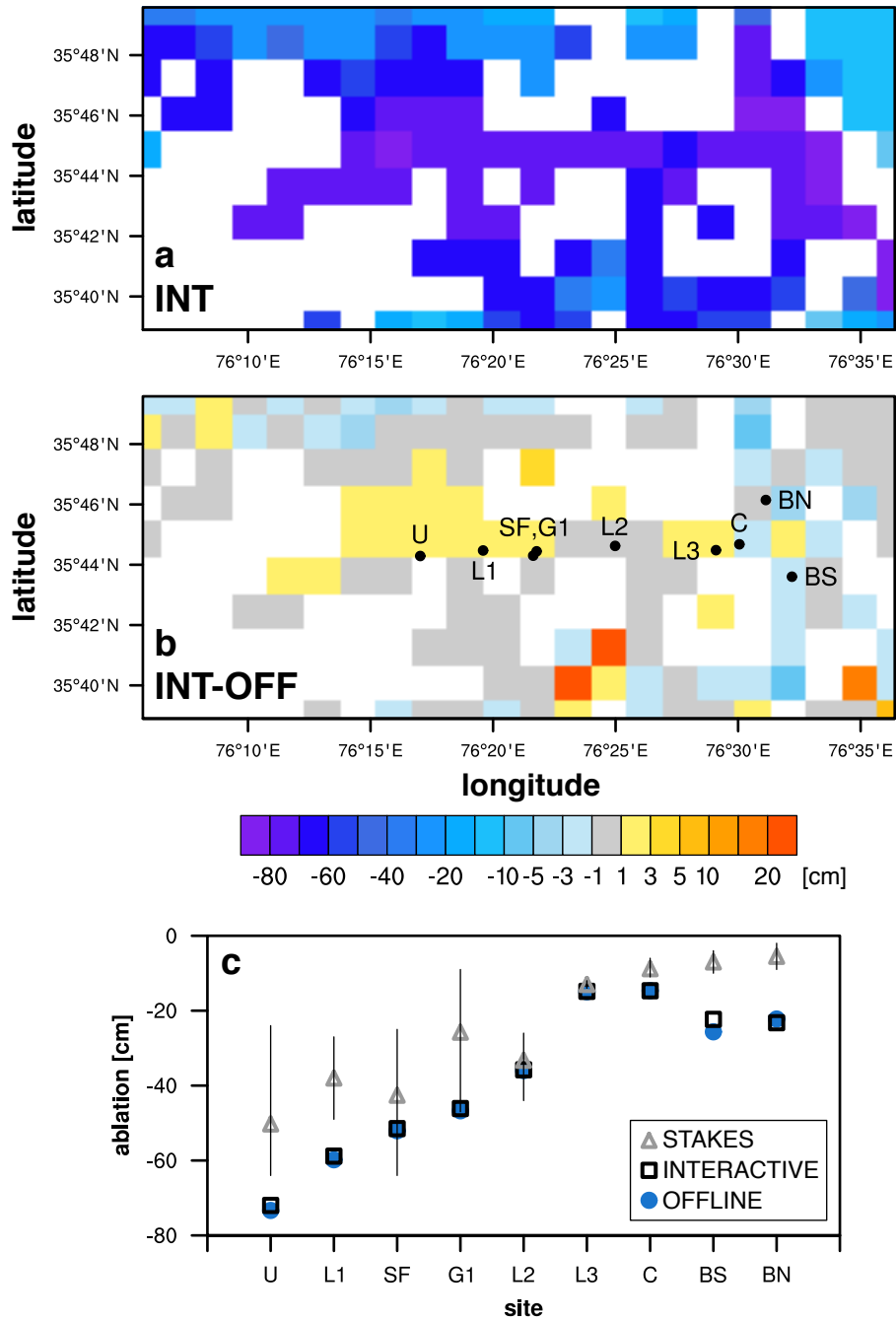


Figure 2.4: (a) Total and (b) INT-OFF surface height change between 1–15 July 2004, in the vicinity of the main tongue of the Baltoro glacier. Stake site and transect locations shown in (b), with additional information provided in Table 2.3. White grid cells correspond to non-glacierized area. (c) Measured mean ablation (triangles) at stake locations, with range of observed values denoted by bars. Simulated INT (OFF) ablation shown by black squares (blue circles).

and other sources of disagreement, comparing the two estimates gives an approximate measure of the effect of neglecting debris, which is thought to cover 38 % of the Baltoro glacier (Mayer et al., 2006) and 73 % of the altitude range of the main glacier tongue considered in Mihalcea et al. (2008), in our simulations.

2.3.3 Influence of interactive coupling

Figure 2.5 presents a time series of daily means of the near-surface WRF meteorological data used as forcing for the CMB model and provides the context for the fluctuations of surface energy and mass fluxes discussed in this section. Near-surface air temperatures in INT are higher by 0.3°C on average than in OFF (Fig. 2.5a). The difference arises primarily from a reduced amplitude of the diurnal cycle, with higher nocturnal temperatures (Fig. 2.5a subpanel). INT simulates higher surface temperatures (T_{sfc}), as well as higher subsurface temperatures in the top 0.5–1 m (peak differences are $\sim 0.7^{\circ}\text{C}$, not shown), as a result of stronger downward long-wave radiative forcing (see Fig. 2.5f for daily average curves). The increase in L_{\downarrow} is expressed between evening and early morning and is a direct result of higher mixing ratios at 2 m in INT (not shown). The change in radiative forcing in INT translates into less heat extraction from the surface layer, through a reduced nocturnal QS, and, in turn, into the near-surface temperature difference. Note that the near-surface air temperature evolution simulated in INT may represent an improvement, as Mölg et al. (2012b) found that WRF + Noah LSM can produce an excessively large diurnal cycle as a result of a nighttime cold bias at 2 m compared with AWS measurements on Kilimanjaro. Interactive coupling also results in a reduction of mean incoming short-wave radiation (-9.0 W m^{-2}) and, as previously mentioned, a mean increase in incoming long-wave radiation (2.4 W m^{-2}), changes that arise from alterations to atmospheric clouds and moisture (see Fig. 2.6). Basin-scale daily-mean differences in the other forcing variables for the CMB model are negligible.

The atmospheric changes induced by including feedbacks from the CMB model are generally small in magnitude and limited in vertical extent, but still appreciable. Air temperature and mixing ratio anomalies are generally confined to the lowest 10 model levels, which correspond to the layer between a mean surface pressure of 543 hPa and the level of 450 hPa (Fig. 2.6a). Vertical

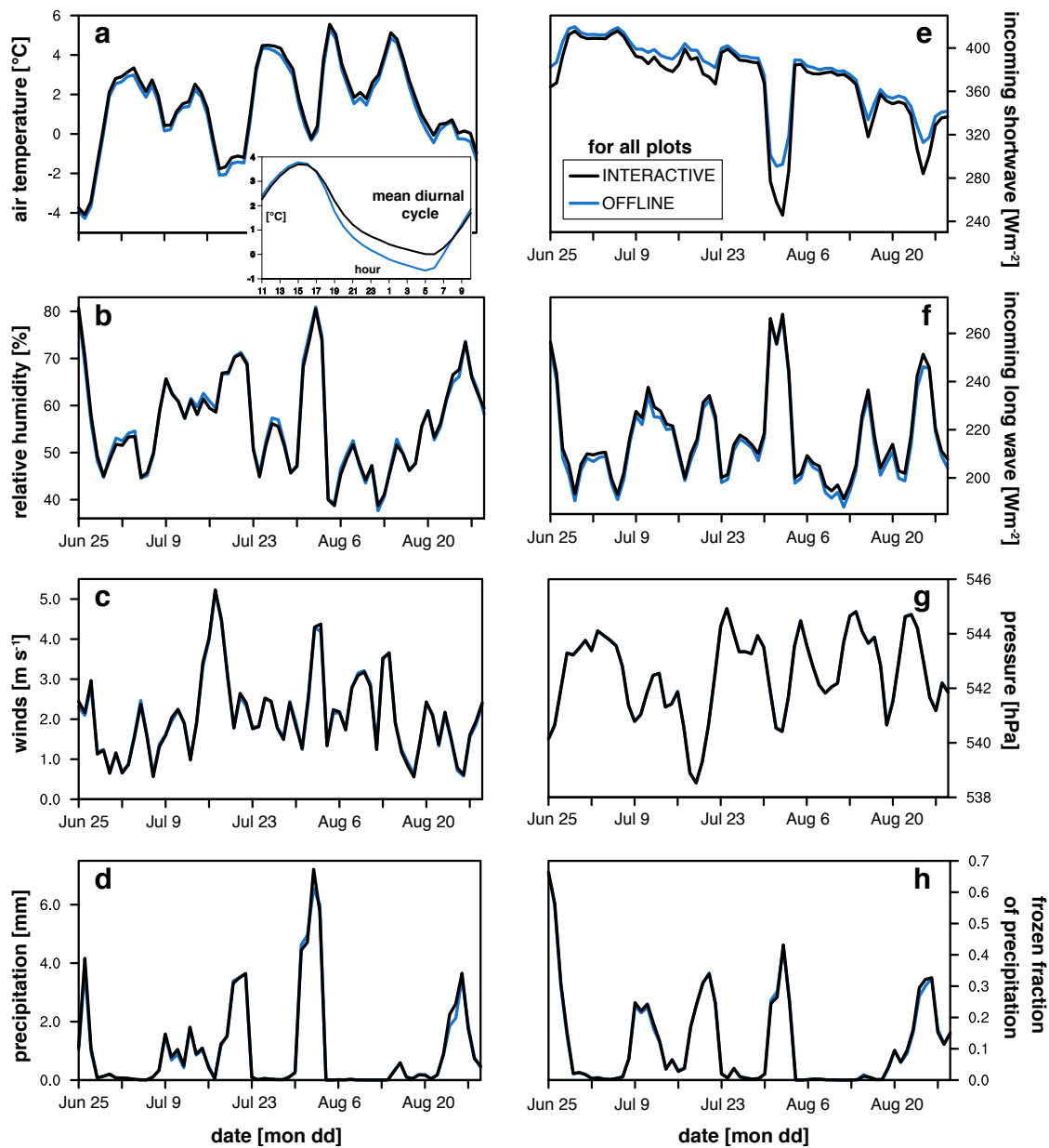


Figure 2.5: Daily mean (a) air temperature, (b) relative humidity, (c) wind speed, (d) total precipitation, incoming (e) normal short-wave and (f) downward long-wave radiation at ground surface, (g) air pressure, and (h) frozen fraction of precipitation, area-averaged over all glacierized grid cells. Data for (a–c), and (g) are taken from the lowest model level ($z = 20$ m). The subpanel in (a) presents the average diurnal temperature cycle over the simulation period. Black (blue) curves display data from the interactive (offline) simulation.

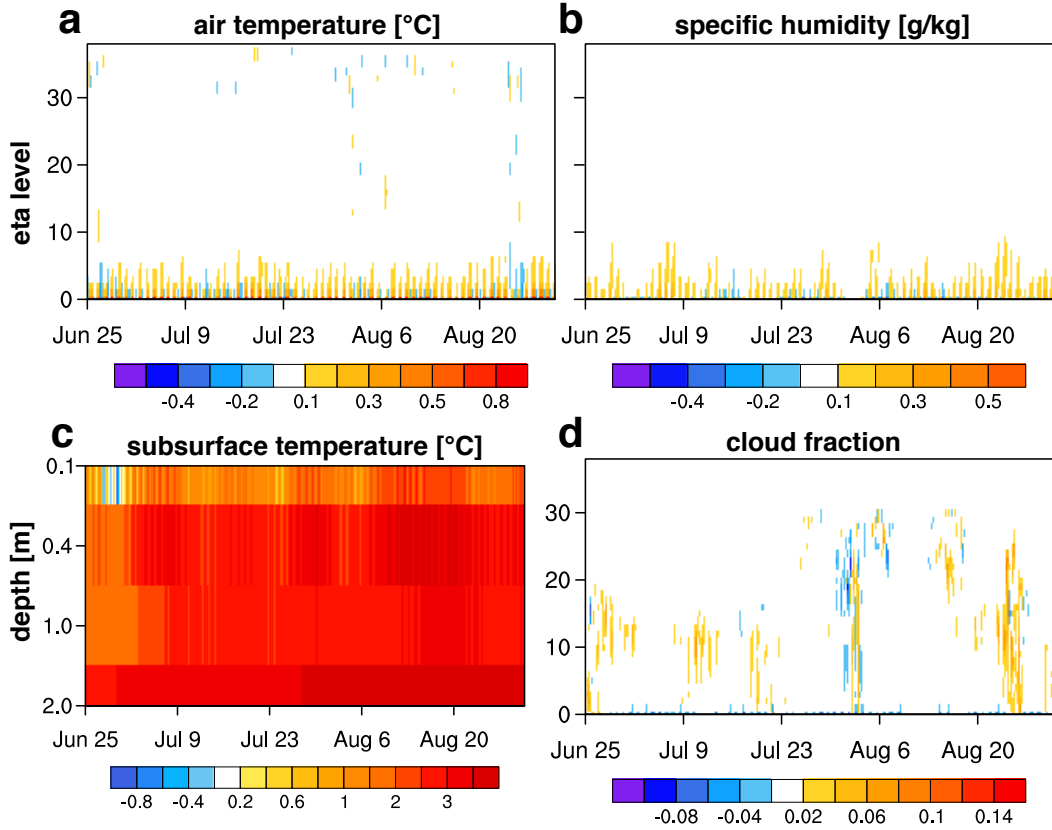


Figure 2.6: Vertical and subsurface distribution of the influence of interactive coupling over glacierized areas illustrated by hourly time series of the change (INT-OFF) in area-averaged (a) air temperature, (b) specific humidity, (c) subsurface temperature, and (d) cloud fraction.

changes in the mean cloud cover fraction are variable, with the greatest differences present near the levels of 375 ($\eta = 12-14$) and 125 hPa ($\eta = 26-29$; Fig. 2.6d). However, interactive coupling has a strong warming influence on the subsurface temperature distribution (on average, +2.6 K; Fig. 2.6c), as a result of (1) the inclusion of the energy flux from penetrating solar radiation, and (2) the method for updating deep soil temperature (T_{ds}), which is defined at a depth of 3 m. With regard to the latter point, T_{ds} in INT is taken from the CMB model subsurface scheme, which resolves the column to a depth of 9 m but is constrained by a lower boundary temperature of 268.6 K in this study. In contrast, the Noah LSM updates T_{ds} using a weighted combination of the annual mean T_{sfc} of the previous year and of the last 150 days as the data become available, with no lower threshold imposed. The resulting minimum values for T_{sfc} in the CMB model and Noah LSM are ~ 245 and 224 K, respectively.

The non-negligible influence of interactive coupling on the near-surface meteorological forcing data translates primarily into reduced ablation of snow and ice in INT (Fig. 2.7a and b). Area-averaged modelled surface height lowering is smaller and total mass balance is less negative in INT, with a mean reduction in ablation over the Karakoram basin of 0.1 m w.e. (-6.0%), to a cumulative value of -1.5 m w.e. by 31 August. The difference in the total mass balance arises despite higher T_{sfc} in INT (Fig. 2.7c). The inclusion of additional processes, such as the refreezing of meltwater, and the different method of subsurface temperature calculation both contribute to higher T_{sfc} in both INT and OFF compared with the Noah LSM.

The vertical balance profile (VBP) on 31 August 2004, is shown in Fig. 2.8a, with areas of negative (positive) balance modelled below (above) ~ 5875 m. The altitudinal distribution is characterized by a shallowing of the VBP above ~ 5000 m, associated with (1) an increase in the positive vertical gradient of the fraction of solid precipitation that contributes positively to CMB (Fig. 2.8c), and (2) cooling of mean surface temperature with height to below the melting point (cf. Fig. 2.2a). Above 5875 m, the VBP profile again steepens as a result of large increases in accumulated, solid precipitation. Below 5875 m, INT produces less ablation (on average, 117.7 mm w.e.), while above this level it simulates a mean increase in accumulation (13.4) in part due to small increases in both accumulated precipitation and its frozen fraction (cf. Fig. 2.8b and c). Averaged over the whole period, the equilibrium line altitudes are 5469 and 5536 m in INT and OFF, respectively, which exceed the annual and generalized estimate of 4500 m by Hewitt (2005) and of 4200–4800 m by Young and Hewitt (1993), because we only simulate the ablation season.

Figure 2.9 presents the surface fluxes of energy and mass from the interactive simulation. On average, the main energy sources are incoming radiation, $S\downarrow$ (374.3 W m^{-2}) and $L\downarrow$ (220.4), with smaller contributions from QS (9.5) and QC (8.1; Fig. 2.9a). The main energy sinks are outgoing $L\uparrow$ (-306.1) and reflected $S\uparrow$ (-186.4), followed by QM (-74.0), QPS (-32.1), and QL (-13.9). Mass gains are, in general, dominated by refreeze (1.0 kg m^{-2}) and solid precipitation (0.9; Fig. 2.9b), while mass loss is primarily through surface (-19.1) and subsurface (-3.2) melt. Figure 2.9 also illustrates the main advantage of the coupled model: it elucidates the important physical processes behind a mass change signal that results from atmospheric forcing.

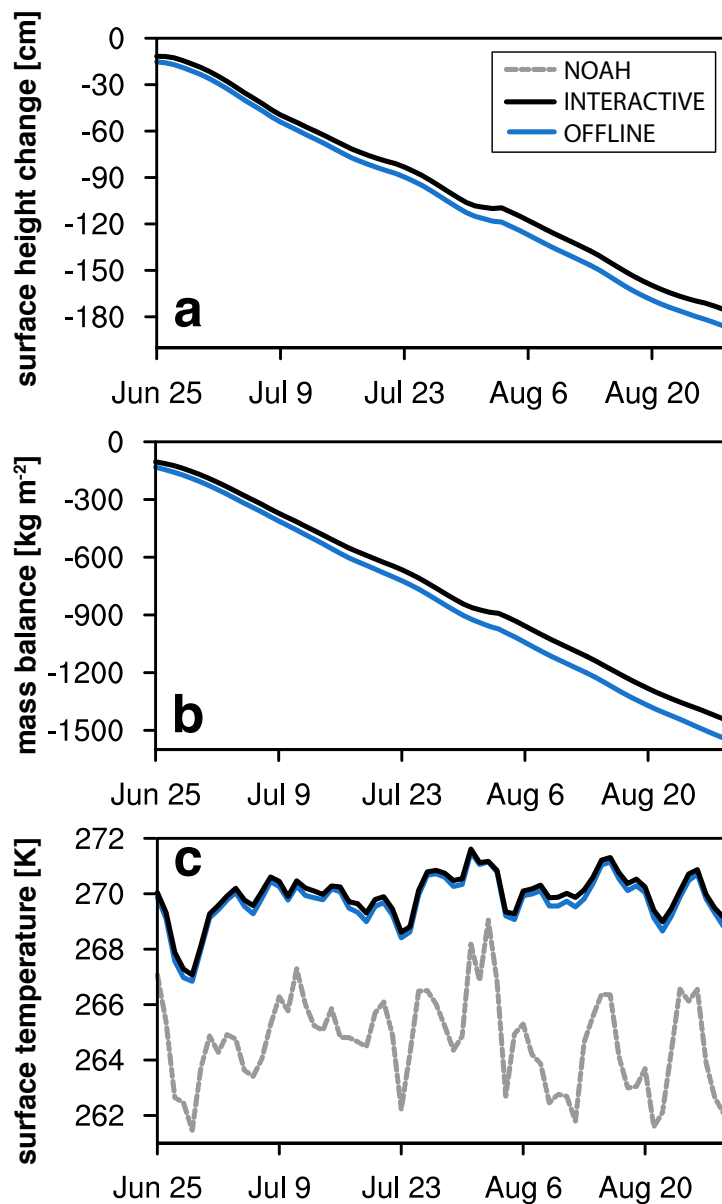


Figure 2.7: Daily basin-scale averages of (a) accumulated surface height change, (b) accumulated total mass balance, and (c) surface temperature. Black (blue) curves display data from the interactive (offline) simulation. For reference, surface temperature simulated by the Noah LSM is the dashed grey curve in (c).

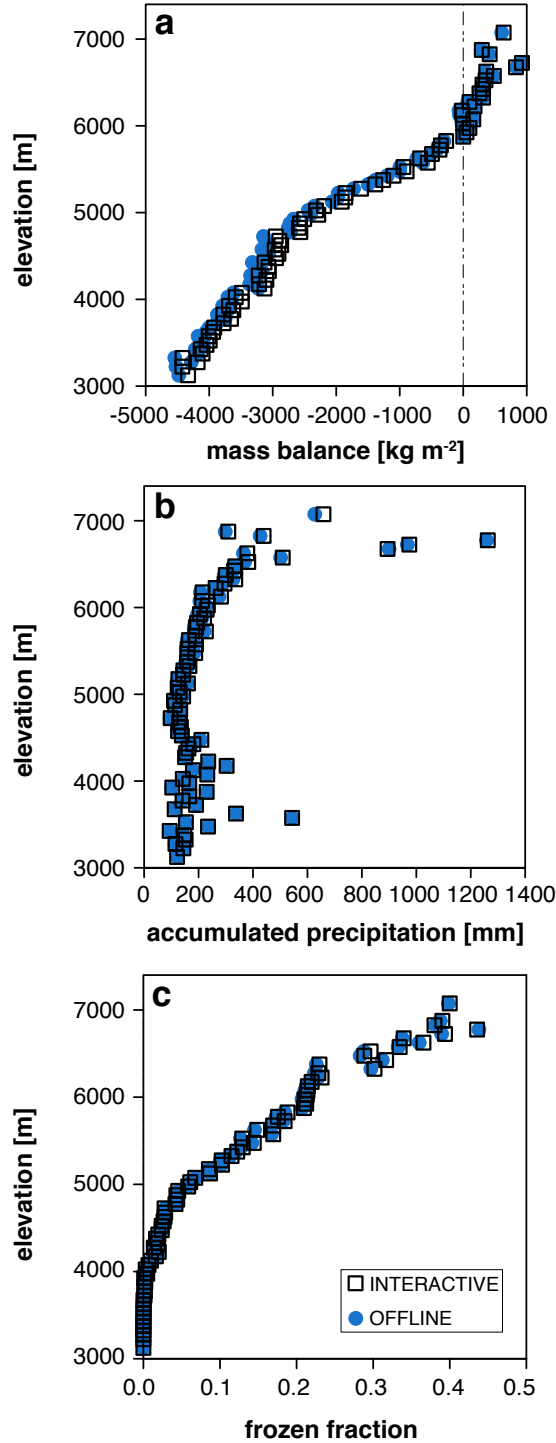


Figure 2.8: (a) The vertical mass balance profile of the Karakoram basin at the end of the simulation. The altitudinal dependence of (b) total accumulated precipitation, and (c) mean frozen fraction, averaged over the simulation. Data are area-averaged in 50 m elevation bins.

For example, the snowfall event that occurs at the beginning of August (cf. solid precipitation bars in Fig. 2.9b) is clearly associated with (1) a reduction in $S\downarrow$ and an increase in $L\downarrow$, (2) a spike in both surface albedo and thus $S\uparrow$, and (3) a reduction in absorbed short-wave radiation that translates into reduced energy for surface and subsurface melt. Furthermore, changes in glacier surface conditions have a noticeable feedback on the atmosphere during and after the snowfall event (cf. e.g. $S\downarrow$ in Fig. 2.5e or cloud fraction changes in Fig. 2.6d).

Interactive coupling has the strongest influence on the net short-wave and ground heat fluxes in the atmospheric model (Fig. 2.10a). The average QG in INT (-23.7 W m^{-2}) greatly exceeds that simulated by the Noah LSM alone (-0.5), due to (1) the inclusion of penetrating short-wave radiation, which always represents an energy sink at the surface, and (2) higher surface temperatures, which result in a stronger (more negative) flux downward to the subsurface. Mean absorbed short-wave radiation is also much larger in INT (184.8 vs. 107.9), as a result of lower average surface albedo (0.49 vs. 0.71; see Fig. 2.2c) over the simulation period. Smaller changes in the turbulent heat fluxes reflect in part different treatments of surface roughness, which is a spatially and temporally varying parameter in WRF-CMB that ranges between 0.8 and 2.6 mm as a function of snow age and generally exceeds the constant value of 1 mm specified by the Noah LSM for snow/ice surfaces.

In the CMB model, interactive coupling induces the largest magnitude change in the net short-wave (-3.3%) and long-wave ($+1.8\%$) radiative fluxes, as a result of the changes to $S\downarrow$ and $L\downarrow$ in the atmospheric model discussed previously. The CMB model fluxes of QL and QPS decrease (become less negative) on average in INT by 8.9% and 3.5%, respectively (Fig. 2.10b). In addition, QC and QS are reduced by 9.0% and 5.0%, respectively. The reduction in QPS is associated with less snow-cover-free glacier area in INT, which reduces the subsurface absorption of short-wave radiation (Mölg et al., 2008). The reduction in the turbulent heat fluxes appears to stem from reduced 10 m wind speeds (-0.2 to 4.3 m s^{-1}), due to the surface roughness changes discussed above. The changes also occur despite (1) a weaker correction for atmospheric stability on average, according to a modified version of the Monin–Obukhov stability function (Eq. 12 in Braithwaite, 1995); and (2) stronger mean gradients in vapor pressure (ΔVP ; -1.2 in INT vs. -0.7 hPa in OFF) and temperature (ΔT ; 1.8 vs. 1.2 K) between the near-surface and lower

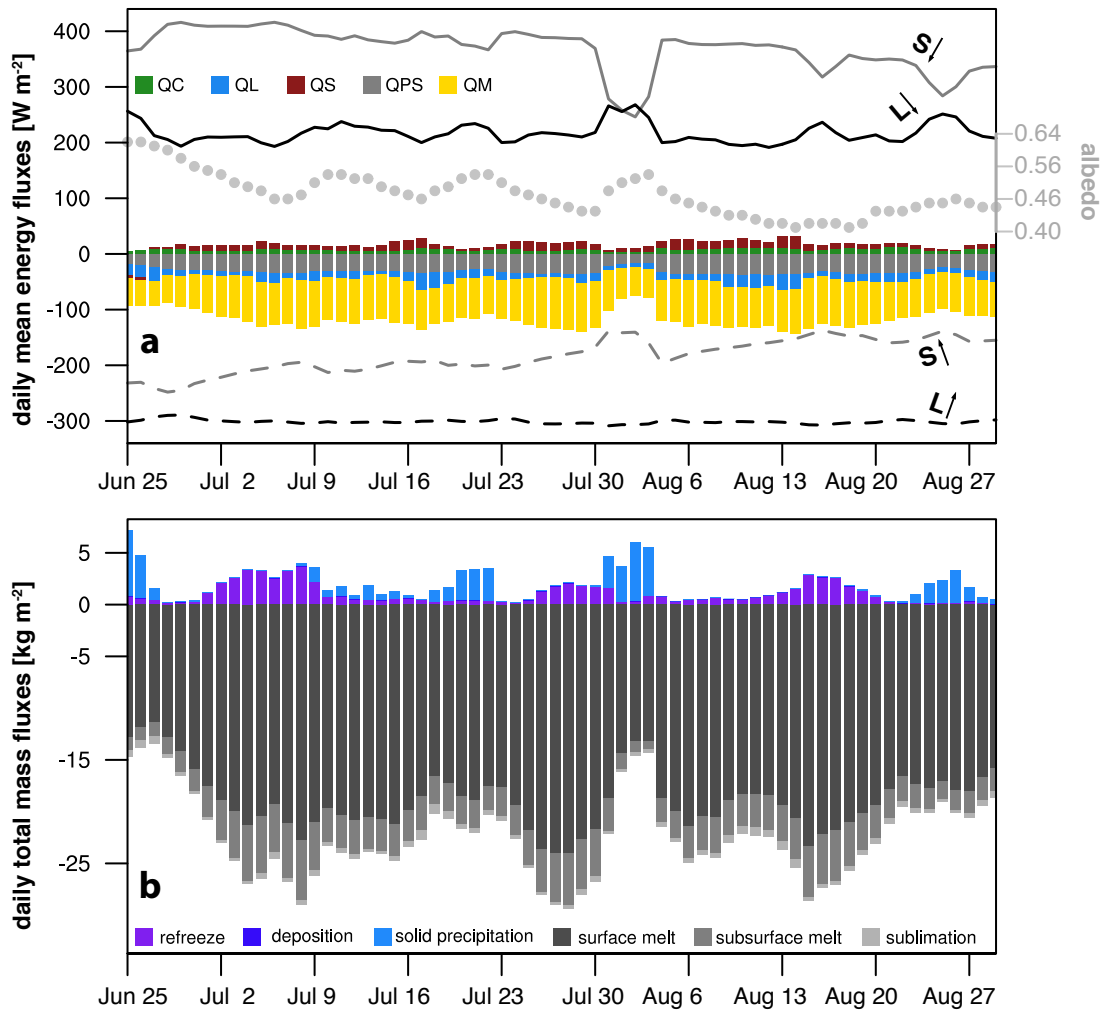


Figure 2.9: From the interactive WRF-CMB simulation: daily (a) mean surface energy balance components (left y-axis; see Eq. 1 for explanation of symbols) and albedo values (grey right y-axis), and (b) sums of mass fluxes. The radiation variables are shown in (a) as solid (directed downward) and dashed (upward) lines, albedo as grey dots, and the other surface energy fluxes as bars. The heat flux from precipitation (QPRC) is negligible and not shown. Values are averaged over glacierized grid cells only.

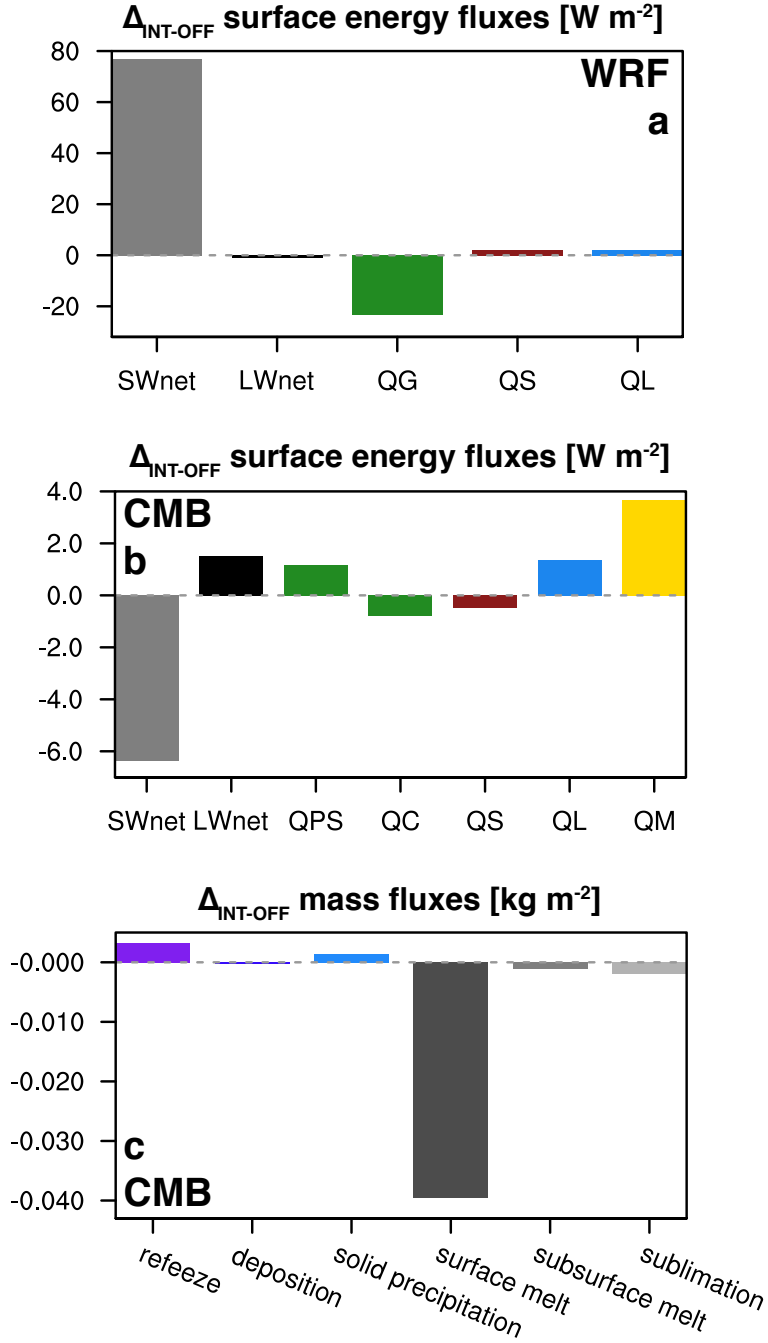


Figure 2.10: Area-averaged mean difference (INT – OFF) over the simulation period and over glacierized grid cells of (a) the main components of the WRF surface energy budget, (b) the CMB model energy fluxes, and (c) the MB model mass fluxes. Symbols in (a) represent, from left to right, net short- and long-wave radiation, ground heat flux, and turbulent fluxes of sensible and latent heat. Note that the sign convention for the turbulent fluxes in (a) is opposite to (b). Symbols in (b) are discussed in Sect. 2.2.2

boundary.

The net result is a decrease of 4.8 % in the average energy available for surface melt, QM, and less negative mass balance over the INT simulation (cf. Fig. 2.7b). The difference is primarily reflected in a reduction in surface melt (−5.8 %; Fig. 2.10c), and is compounded by increases in both refreezing in the snowpack and the formation of superimposed ice (8.5 % combined) as well as by greater solid precipitation (4.0 %). In general, mass exchanges between the glacier surface and the overlying boundary layer are smaller in INT, with the weakening in QL resulting in less sublimation (particularly at night) and deposition (at all times).

2.3.4 Remarks and perspectives for future research

The explicit approach to modelling alpine glacier climatic mass balance using WRF first demonstrated by Mölg and Kaser (2011) has been applied in offline mode for simulations of small glaciers (Mölg and Kaser, 2011; Mölg et al., 2012a,b) and has yielded important insights into the physical processes and the atmospheric forcing underlying mass fluctuations. However, here we demonstrate that feedbacks due to CMB processes are evident for the heavily-glacierized Karakoram region. The basin-scale influence of interactive coupling on the atmospheric forcing data, while moderate, acts to reduce the energy available for surface melt and, in concert with both reduced mass exchanges between the surface and boundary layer and increased refreezing, reduces modelled ablation during the summer of 2004. Furthermore, we demonstrate that the inclusion of additional real processes such as CMB feedbacks renders WRF-CMB capable of simulating observed magnitudes of CMB.

To the best of our knowledge, only one previous study, that of Kotlarski et al. (2010b), has performed interactive and distributed simulations of alpine glacier mass balance, achieved by introducing a subgrid-scale parameterization for glaciers and their areal changes into a regional climate model configured with a relatively coarse spatial resolution of ~ 18 km. However, their implicit treatment “pools” the glaciers located in a grid cell into one ice mass at a fixed altitude and with a uniform snow depth. Furthermore, they quantify the effect of two-way coupling by comparing their interactive simulation with a control run that contains no glaciers (i.e. snow and ice surfaces are compared with bare soil or vegetation-covered surfaces), thus obscuring the

exact role of feedbacks. Therefore, this paper presents the first assessment of the importance and strength of interactions between alpine glaciers and the atmosphere on explicit simulations of CMB.

We have shown results for only a short study period, of one ablation season, to evaluate the novel approach and its performance against the available measurements. The Karakoram, and High Mountain Asia in general, are very data-sparse (e.g. Bolch et al., 2012), due to the expense and logistics of field surveys in this remote region. The model captures the magnitude of the 53 stake measurements of Mihalcea et al. (2006), and simulating the ablation season likely represents the greatest test for some of the simplifying assumptions employed, such as zero debris cover. However, a longer application is needed to assess the year-long and inter-annual influence of interactive coupling, as well as the long-term performance of the atmospheric model under the climate-simulation forcing strategy we employ (i.e. with no nudging or model re-initialization; e.g. Maussion et al., 2011). Simulations of glacier mass balance are also inherently sensitive to the modeled solid precipitation (Mölg and Kaser, 2011), which is influenced in our study by the choice of microphysics scheme. Furthermore, the optimal choice of diffusion scheme, its strength, and its influence on simulated precipitation and therefore glacier CMB are beyond the scope of this paper and have not been investigated fully for our area of interest and model configuration. The simulation of near-surface meteorological fields by WRF over glacier surfaces has been found to be relatively insensitive to the choice of physical parameterizations (Claremar et al., 2012); however, the extent to which modelled CMB is dependent on the model physics, the choice of numerics, and the spatial resolution of the finest domain represents an important uncertainty that will be explored in a future study.

The mean proportion of debris covered-area on Karakoram glaciers is estimated to be 18–22% (Scherler et al., 2011a; Hewitt, 2011), which is higher than the pan-Himalayan average of $\sim 10\%$ (Bolch et al., 2012). Specific to the Baltoro glacier, Mayer et al. (2006) estimate that $\sim 38\%$ of the total glacier area is debris covered. The presence of debris above a threshold, or “critical thickness”, of ~ 2 cm has been shown, empirically and through surface energy balance modelling, to reduce glacier ablation as a result of its insulating effect (e.g. Østrem, 1959; Kayastha et al., 2000; Nicholson and Benn, 2006; Reid et al., 2012). The range of mean debris

thicknesses at the stake sites is 2.0–18.0 cm (Table 2.4), suggesting that on the whole insulation effects should dominate over the lowering of surface albedo except at the sites L2 and L3 where debris thickness is approximately equal to the critical value. Indeed, modelled ablation closely matches the measured rate at these two sites and elsewhere is overestimated by WRF-CMB (Fig. 2.4c), physically consistent with the exclusion of debris in this study. This interpretation is supported by the first distributed ablation modelling study for debris-covered ice, that of Reid et al. (2012), which found reduced sub-debris ablation when depth exceeded 2 cm. However, it is noteworthy that geodetic estimates of early 21st century elevation changes in the Karakoram (Gardelle et al., 2012; Kääb et al., 2012) do not show a difference between clean and debris-covered ice.

Given the similarity of the underlying surface types in INT (snow/ice) and OFF (snow) influencing the atmospheric forcing data, the difference in simulated CMB for the clean glacier simulations is relatively small. From the results presented here, it could be expected that the inclusion of feedbacks is not essential for small glaciers or less glacierized basins. However, we would expect the interactive inclusion of the CMB model to have a larger influence for glaciers with significant debris cover, as its presence alters surface temperature and moisture properties and thus turbulent exchanges with the surface boundary layer (e.g. Takeuchi et al., 2000). To assess the role of feedbacks for debris-covered glaciers and to allow the WRF-CMB modelling system to provide long-term, accurate simulations in the Karakoram, including the effects of debris cover on surface conditions and glacier ablation represents important future work. Treating debris cover in distributed mass balance modelling is also becoming more important in light of observations of increasing debris-covered area in many regions (e.g. Stokes et al., 2007; Bhambri et al., 2011). Another process that is thought to be important for Karakoram glaciers is accumulation via snow and ice avalanching (e.g. Hewitt, 2011), which may be useful to parameterize. Finally, dynamical ice flow changes have been shown to be important when quantifying the response of Himalayan glaciers to climate fluctuations on multiannual timescales (e.g. Scherler et al., 2011a; Gardelle et al., 2012; Kääb et al., 2012; Azam et al., 2012).

2.4 Conclusion

CMB feedbacks have been introduced into a new, multi-scale modelling approach for explicitly resolving the surface and climatic mass balance processes of alpine glaciers, and this technique has been extended to the regional scale. Although validation data is sparse, the model captures the magnitude of available in situ measurements, with improvements arising from including feedbacks from the CMB model to WRF. Furthermore, discrepancies between observed and simulated ablation can be attributed to physical processes neglected as simplifying assumptions, particularly debris cover effects.

Both components of WRF-CMB are based on physical principles, with no statistical down-scaling at their interface. The direct linkage increases the applicability of this approach for the simulation of the past- and future-climate response of glaciers, since the modelling system produces a physically-consistent response to changes in external forcing. Incorporation of the CMB model also increases the number of physical processes important for glaciers represented in the atmospheric model, and provides a consistent calculation of surface energy and mass fluxes, since changes in glacier surface conditions are permitted to influence the atmospheric drivers. Perhaps the most important advantage, however, is that WRF-CMB permits direct causal attribution of glacier mass changes to both physical processes and the main atmospheric drivers. With further development, the model has the potential to bridge the data gap in the Karakoram and shed light on the role of climate forcing in the anomalous behaviour of glaciers in this region.

The offline approach to simulations of CMB, as well as the simplified representation of glaciers in regional atmospheric models, essentially treats either the atmosphere or alpine glaciers simply as a boundary condition. We suggest that this unified, explicit approach should be increasingly adopted in future studies, particularly for heavily glacierized regions.

References

- Azam, M. F., Wagnon, P., Ramanathan, A., Vincent, C., Sharma, P., Arnaud, Y., Linda, A., Pottakkal, J. G., Chevallier, P., Singh, V. B., and Berthier, E.: From balance to imbalance: a shift in the dynamic behaviour of Chhota Shigri glacier, western Himalaya, India, *J. Glaciol.*, 58, 315–324, 2012.
- Bhambri, R., Bolch, T., Chaujar, R. K., and Kulshreshtha, S. C.: Glacier changes in the Garhwal Himalaya, India, from 1968 to 2006 based on remote sensing, *J. Glaciol.*, 57, 543–556, 2011.
- Bolch, T., Kulkarni, A., Kääb, A., Huggel, C., Paul, F., Cogley, J. G., Frey, H., Kargel, J. S., Fujita, K., Scheel, M., Bajracharya, S., and Stoffel, M.: The state and fate of Himalayan glaciers, *Science*, 336, 310–314, 2012.
- Braithwaite, R. J.: Aerodynamic stability and turbulent sensible-heat flux over a melting ice surface, the Greenland ice sheet, *J. Glaciol.*, 41, 562–571, 1995.
- Brodzik, M. J., Armstrong, R., and Savoie, M.: Global EASE-Grid 8-day Blended SSM/I and MODIS Snow Cover, National Snow and Ice Data Center, Boulder, Colorado, USA, Digital media, 2007.
- Bryan, G. H., Wyngaard, J. C., and Fritsch, J.: Resolution requirements for simulations of deep moist convection, *Mon. Weather Rev.*, 131, 2394–2416, 2003.
- Chen, F. and Dudhia, J.: Coupling an advanced land surface-hydrology model with the Penn State – NCAR MM5 modelling system. Part I: Model implementation and sensitivity, *Mon. Weather Rev.*, 129, 569–585, 2001.

- Claremar, B., Obleitner, F., Reijmer, C., Pohjola, V., Waxegård, A., Karner, F., and Rutgersson, A.: Applying a mesoscale atmospheric model to Svalbard glaciers, *Adv. Meteorol.*, 2012, 321649, doi:10.1155/2012/321649, 2012.
- Cogley, J. G.: Present and future states of Himalaya and Karakoram glaciers, *Ann. Glaciol.*, 52, 69–73, 2011.
- Cogley, J. G., Hock, R., Rasmussen, L. A., Arendt, A. A., Bauder, A., Braithwaite, R. J., Jansson, P., Kaser, G., Müller, M., Nicholson, L., and Zemp, M.: Glossary of Glacier Mass Balance and Related Terms, IHP-VII Technical Documents in Hydrology No. 86, IACS Contribution No. 2, UNESCO-IHP, Paris, 2011.
- Craig, G. C. and Dörnback, A.: Entrainment in cumulus clouds: What resolution is cloud-resolving?, *J. Atmos. Sci.*, 65, 3978–3988, 2008.
- Dee, D. P., Uppala, S. M., Simmons, A. J., Berrisford, P., Poli, P., Kobayashi, S., Andrae, U., Balmaseda, M. A., Balsamo, G., Bauer, P., Bechtold, P., Beljaars, A. C. M., van de Berg, L., Bidlot, J., Bormann, N., Delsol, C., Dragani, R., Fuentes, M., Geer, A. J., Haimberger, L., Healy, S. B., Hersbach, H., Hlm, E. V., Isaksen, L., Kållberg, P., Köhler, M., Matricardi, M., McNally, A. P., Monge-Sanz, B. M., Morcrette, J.-J., Park, B.-K., Peubey, C., de Rosnay, P., Tavolato, C., Thpaut, J.-N., and Vitart, F.: The ERA-Interim reanalysis: configuration and performance of the data assimilation system, *Q. J. Roy. Meteorol. Soc.*, 137, 553–597, 2011.
- Frey, H., Paul, F., and Strozzi, T.: Compilation of a glacier inventory for the western Himalayas from satellite data: methods, challenges, and results, *Remote Sens. Environ.*, 124, 832–843, 2012.
- Gardelle, J., Berthier, E., and Arnaud, Y.: Slight mass gain of Karakoram glaciers in the early twenty-first century, *Nat. Geosci.*, 5, 322–325, 2012.
- Gardner, A. S., Sharp, M. J., Koerner, R. M., Labine, C., Boon, S., Marshal, S. J., Burgess, D. O., and Lewis, E.: Near-surface temperature lapse rates over Arctic glaciers and their implications for temperature downscaling, *J. Climate*, 22, 4281–4298, 2009.

- Hewitt, K.: The Karakoram anomaly? Glacier expansion and the “elevation effect” Karakoram Himalaya, *Mt. Res. Dev.*, 25, 332–340, 2005.
- Hewitt, K.: Glacier change, concentration, and elevation effects in the Karakoram Himalaya, Upper Indus Basin, *Mt. Res. Dev.*, 31, 188–200, 2011.
- ICIMOD (International Centre for Integrated Mountain Development): Inventory of glaciers, glacial lakes and identification of potential glacial lake outburst floods (GLOFs), affected by global warming in the Mountains of Himalayan Region, Kathmandu, DVD-ROM, 2007.
- Jiménez, P. A., Dudhia, J., González-Rouco, J. F., Navarro, J., Montávez, J. P., and García-Bustamante, E.: A revised scheme for the WRF surface layer formulation, *Mon. Weather Rev.*, 140, 898–918, 2012.
- Kääb, A., Berthier, E., Nuth, C., Gardelle, J., and Arnaud, Y.: Contrasting patterns of early twenty-first-century glacier mass change in the Himalayas, *Nature*, 488, 495–498, 2012.
- Kayastha, R. B., Takeuchi, Y., Nakawo, M., and Ageta, Y.: Practical prediction of ice melting beneath various thickness of debris cover on Khumbu Glacier, Nepal using a positive degree-day factor, *Symposium at Seattle 2000 – Debris-Covered Glaciers*, IAHS Publ., 264, 71–81, 2000.
- Kotlarski, S., Paul, F., and Jacob, D.: Forcing a distributed glacier mass balance model with the regional climate model REMO. Part I: Climate model evaluation, *J. Climate*, 23, 1589–1606, 2010a.
- Kotlarski, S., Jacob, D., Podzum, R., and Paul, F.: Representing glaciers in a regional climate model, *Clim. Dynam.*, 34, 27–46, 2010b.
- Knier, J. C., Bryan, G. H., and Hacker, J. P.: Explicit numerical diffusion in the WRF model, *Mon. Weather Rev.*, 135, 3808–3824, 2007.
- Livneh, B., Xia, Y., Mitchell, K. E., Ek, M. B., and Lettenmaier, D. P.: Noah LSM snow model diagnostics and enhancements, *J. Hydrometeorol.*, 11, 721–738, 2009.

- Machguth, H., Paul, F., Kotlarski, S., and Hoelzle, M.: Calculating distributed glacier mass balance for the Swiss Alps from regional climate model output: a methodical description and interpretation of the results, *J. Geophys. Res.*, 114, D19106, doi:10.1029/2009JD011775, 2009.
- Marshall, S. J., Sharp, M. J., Burgess, D. O., and Anslow, F. S.: Surface temperature lapse rate variability on the Prince of Wales Ice-eld, Ellesmere Island, Canada: implications for regional-scale downscaling of temperature, *Int. J. Climatol.*, 27, 385–398, 2007.
- Maussion, F., Scherer, D., Finkelnburg, R., Richters, J., Yang, W., and Yao, T.: WRF simulation of a precipitation event over the Tibetan Plateau, China – an assessment using remote sensing and ground observations, *Hydrol. Earth Syst. Sci.*, 15, 1795–1817, 2011.
- Mayer, C., Lambrecht, A., Belo, M., Smiraglia, C., and Diolaiuti, G.: Glaciological characteristics of the ablation zone of Baltoro glacier, Karakoram, Pakistan, *Ann. Glaciol.*, 43, 123–131, 2006.
- Mihalcea, C., Mayer, C., Diolaiuti, G., Smiraglia, C., and Tartari, G.: Ablation conditions on the debris covered part of Baltoro Glacier, Karakoram, *Ann. Glaciol.*, 43, 292–300, 2006.
- Mihalcea, C., Mayer, C., Diolaiuti, G., DAgata, C., Smiraglia, C., Lambrecht, A., Vuillermoz, E., and Tartari, G.: Spatial distribution of debris thickness and melting from remote-sensing and meteorological data, at debris-covered Baltoro glacier, Karakoram, Pakistan, *Ann. Glaciol.*, 48, 49–57, 2008.
- Molinari, J. and Dudek, M.: Parameterization of convective precipitation in mesoscale numerical-models – a critical-review, *Mon. Weather Rev.*, 120, 326–344, 1992.
- Mölg, T. and Kaser, G.: A new approach to resolving climate–cryosphere relations: downscaling climate dynamics to glacier-scale mass and energy balance without statistical scale linking, *J. Geophys. Res.*, 116, D16101, doi:doi:10.1029/2011JD015669, 2011.
- Mölg, T., Cullen, N. J., Hardy, D. R., Kaser, G., and Klok, E. J.: Mass balance of a slope glacier on Kilimanjaro and its sensitivity to climate, *Int. J. Climatol.*, 28, 881–892, 2008.

- Mölg, T., Cullen, N. J., Hardy, D. R., Winkler, M., and Kaser, G.: Quantifying climate change in the tropical midtroposphere over East Africa from glacier shrinkage on Kilimanjaro, *J. Climate*, 22, 4162–4181, 2009.
- Mölg, T., Maussion, F., Yang, W., and Scherer, D.: The footprint of Asian monsoon dynamics in the mass and energy balance of a Tibetan glacier, *The Cryosphere*, 6, 1445–1461, 2012a.
- Mölg, T., Grohauser, M., Hemp, A., Hofer, M., and Marzeion, B.: Limited forcing of glacier loss through land-cover change on Kilimanjaro, *Nat. Clim. Change*, 2, 254–258, 2012b.
- Nicholson, L. and Benn, D.: Calculating ice melt beneath a debris layer using meteorological data, *J. Glaciol.*, 52, 463–470, 2006.
- Niu, G.-Y., Yang, Z.-L., Mitchell, K. E., Chen, F., Ek, M. B., Barlage, M., Kumar, A., Manning, K., Niyogi, D., Rosero, E., Tewari, M., and Youlong, X.: The community Noah land surface model with multiparameterization options (Noah-MP): 1. Model description and evaluation with local-scale measurements, *J. Geophys. Res.*, 116, D12109, doi:10.1029/2010JD015139, 2011.
- Oerlemans, J. and Knap, W. H.: A 1 year record of global radiation and albedo in the ablation zone of Morteratschgletscher, Switzerland, *J. Glaciol.*, 44, 231–238, 1998.
- Østrem, G.: Ice melting under a thin layer of moraine, and the existence of ice cores in moraine ridges, *Geogr. Ann.*, 41, 228–230, 1959.
- Paul, F. and Kotlarski, S.: Forcing a distributed glacier mass balance model with the regional climate model REMO. Part II: Downscaling strategy and results for two Swiss glaciers, *J. Climate*, 23, 1607–1620, 2010.
- Petch, J. C.: Sensitivity study of developing convection in a cloud-resolving model, *Q. J. Roy. Meteorol. Soc.*, 132, 345–358, 2006.
- Petersen, L. and Pellicciotti, F.: Spatial and temporal variability of air temperature on a melting glacier: atmospheric controls, extrapolation methods and their effect on melt modeling, Juncal Norte Glacier, Chile, *J. Geophys. Res.*, 116, D23109, doi:10.1029/2011JD015842, 2011.

- Pritchard, M. S., Bush, A. B. G., and Marshall, S. J.: Neglecting ice-atmosphere interactions underestimates ice sheet melt in millennial-scale deglaciation simulations, *Geophys. Res. Lett.*, 35, L01503, doi:10.1029/2007GL031738, 2008.
- Radić, V. and Hock, R.: Regionally differentiated contribution of mountain glaciers and ice caps to future sea-level rise, *Nat. Geosci.*, 4, 91–94, 2011.
- Reid, T. D., Carenzo, M., Pellicciotti, F., and Brock, B. W.: Including debris cover effects in a distributed model of glacier ablation, *J. Geophys. Res.*, 117, D18105, doi:10.1029/2012JD017795, 2012.
- Ridley, J. K., Huybrechts, P., Gregory, J. M., and Lowe, J. A.: Elimination of the Greenland ice sheet in a high CO₂ climate, *J. Climate*, 18, 3409–3427, 2005.
- Scherler, D., Bookhagen, B., and Strecker, M. R.: Spatially variable response of Himalayan glaciers to climate change affected by debris cover, *Nat. Geosci.*, 4, 156–159, 2011.
- Shi, Y., Liu, C., and Kang, E.: The glacier inventory of China, *Ann. Glaciol.*, 50, 1–4, 2009.
- Skamarock, W. C. and Klemp, J. B.: A time-split nonhydrostatic atmospheric model for weather research and forecasting applications, *J. Comput. Phys.*, 227, 3465–3485, 2008.
- Stokes, C. R., Popovnin, V., Aleynikov, A., Gurney, S. D., and Shahgedanova, M.: Recent glacier retreat in the Caucasus Mountains, Russia, and associated increase in supraglacial debris cover and supra-/proglacial lake development, *Ann. Glaciol.*, 46, 195–203, 2007.
- Stroeve, J. C., Box, J. E., and Haran, T.: Evaluation of the MODIS (MOD10A1) daily snow albedo product over the Greenland ice sheet, *Remote Sens. Environ.*, 105, 155–171, 2006.
- Takeuchi, Y., Kayastha, R. B., and Nakawo, M.: Characteristics of ablation and heat balance in debris-free and debris-covered areas on Khumbu glacier, Nepal Himalayas, in the pre-monsoon season, in: *Debris-covered glaciers*, IAHS Publ., 264, 53–61, 2000.
- van Pelt, W. J. J., Oerlemans, J., Reijmer, C. H., Pohjola, V. A., Pettersson, R., and van Angelen, J. H.: Simulating melt, runoff and refreezing on Nordenskiöldbreen, Svalbard, using a coupled snow and energy balance model, *The Cryosphere*, 6, 641–659, 2012.

- Weisman, M. L., Skamarock, W. C., and Klemp, J. B.: The resolution dependence of explicitly modeled convective systems, *Mon. Weather Rev.*, 125, 527–548, 1997.
- Yao, T.: *Map of the Glaciers and Lakes on the Tibetan Plateau and Adjoining Regions*, Xian Cartographic Publishing House, Xian, China, 2007.
- Young, G. J. and Hewitt, K.: Glaciohydrological features of the Karakoram Himalaya: measurement possibilities and constraints, in: *Proceedings of the Kathmandu Symposium – Snow and Glacier Hydrology*, IAHS Publ., 218, 273–283, 1993.

Chapter 3

Representing moisture fluxes and phase changes in glacier debris cover using a reservoir approach

3.1 Introduction¹

Numerical modelling of debris-covered glaciers has received renewed scientific interest in recent years, because their contribution to changes in ice mass and water resources in many regions remains poorly understood (e.g. Kääb et al., 2012) and because the proportion of debris-covered glacier area is rising as glaciers recede (e.g. Stokes et al., 2007; Bolch et al., 2008; Bhambri et al., 2011).

It is well established that supraglacial debris exerts an important control on glacier melt rates. Subdebris ice melt is strongly enhanced when the debris thickness is less than a few centimetres, due to a reduction in surface albedo, an increase in absorption of shortwave radiation, and the rapid transfer of energy to the underlying ice. Melt decreases exponentially as the thickness increases, as a result of insulation of the underlying glacier ice from the overlying atmosphere (e.g. Østrem, 1959; Loomis, 1970; Fujii, 1977; Inoue and Yoshida, 1980; Mattson et al., 1993). The presence of debris also alters the glacier surface energy balance, by permitting surface

¹L.I. Nicholson, B.W. Brock, F. Maussion, R. Essery, and A. B. G. Bush contributed to this chapter.

temperatures to rise above the melting point and by altering surface heat and moisture exchanges with the atmosphere (e.g. Brock et al., 2010).

Numerous point models of the surface energy balance of debris-covered glaciers have been developed to simulate subdebris ice melt (e.g. Kraus, 1975; Nakawo and Young, 1982; Han et al., 2006; Nicholson and Benn, 2006; Reid and Brock, 2010). In recent years, models of debris cover have been extended to distributed simulations (Zhang et al., 2011), and to include both explicit calculation of heat conduction through debris layers resolved into multiple levels and snow accumulation on top of the debris (Reid et al., 2012; Lejeune et al., 2013; Fyffe et al., 2014).

However, due to the complexity of treating moisture in supraglacial debris cover, surface energy balance models to date have neglected the latent heat and surface moisture flux components, with the exception of (1) testing the two end-member cases of completely dry or completely saturated debris layers (e.g. Nakawo and Young, 1981; Kayastha et al., 2000; Nicholson and Benn, 2006), and (2) using measurements of surface relative humidity to calculate the flux when the surface is saturated (Reid and Brock, 2010; Reid et al., 2012). In addition, moisture inputs to the debris layer – by percolation of snowmelt and rainfall, or from the underlying melting ice via capillary action – and their phase changes have not been taken into account. Rather, any water is assumed to run off immediately, without influencing the thermal properties of the debris (e.g. Reid and Brock, 2010; Reid et al., 2012; Lejeune et al., 2013; Fyffe et al., 2014).

Both field observations and laboratory experiments indicate that debris covers can be partially or entirely saturated at times during the ablation season, depending on their thickness and the environmental conditions, with a minimum of a saturated region adjacent to the interface if the underlying ice is at the melting point (e.g. Nakawo and Young, 1981; Conway and Rasmussen, 2000; Kayastha et al., 2000; Reznichenko et al., 2010; Nicholson and Benn, 2012). The presence of interstitial water and ice modifies the thermal properties of the debris layer, particularly during transition seasons (e.g. Conway and Rasmussen, 2000; Nicholson and Benn, 2012). In addition, percolation of rain through a debris layer and other inputs of moisture can influence the thermal regime by heat advection (Reznichenko et al., 2010), and by providing a source of moisture for evaporation that cools the debris and therefore reduces heat transmission to the

ice below.

Surface vapour exchanges between the debris and the overlying atmosphere influence the surface energy balance and have been observed to be non-negligible at times. Sakai et al. (2004) estimated that the ablation calculated by an energy balance approach that neglects the latent heat flux, QL , would provide an overestimate of up to 100 %, since its lowering effect on surface temperature would not be captured. During the ablation season on the Miage Glacier in the Italian Alps, Brock et al. (2010) calculated large spikes in QL , of up to -800 W m^{-2} , that coincided with daytime rainfall events on the heated debris surface. Furthermore, while they estimated that energy inputs due to condensation and deposition were negligible, ground frosts were observed on a weekly to biweekly basis in the upper parts of the glacier, which may have slowed early daytime heating of the debris layer. Given the clear influence of moisture on the surface energy balance and the subsurface thermal regime, there is a need to develop a treatment for moisture fluxes into and within the debris layer, as well as for phase changes, that would allow for a variation in the thermal properties and energy sources and sinks of the debris layer with depth and time.

In this paper, we explore the utility of a reservoir scheme for parameterizing moisture fluxes and phase changes in a glacier debris layer that has been incorporated into a glacier climatic mass balance model. We exploit a short period of available in situ measurements over supraglacial debris to evaluate the model performance during an ablation season, with a second simulation of a fall season to fully demonstrate the capabilities of the model. Within the context of the simplified parameterization, we show the influence of moisture on heat transfer in the debris layer, its physical properties, and subdebris ice melt, as well as assess the scale of the impact of phase changes. The eventual goal of this work is to incorporate the debris modifications into an interactively coupled modelling system of the atmosphere and alpine glaciers at the regional scale (Collier et al., 2013). The inclusion of debris is essential for (1) accurately capturing surface conditions over debris-covered glaciers and, therefore, atmosphere–glacier feedbacks, and (2) rigorously assessing regional climatic influences on the CMB of debris-covered glaciers.

3.2 Methods

3.2.1 Debris-free glacier CMB model

The debris-free version of the glacier CMB model is described in detail by Mölg et al. (2008, 2009, 2012a). The model has been applied to simulating glaciers in a wide variety of climatic settings (e.g. Mölg et al., 2012a; Collier et al., 2013; Nicholson et al., 2013; MacDonell et al., 2013). The CMB model solves the surface energy balance equation to determine the energy available for melt and other mass fluxes, given by

$$S\downarrow \cdot (1 - \alpha) + \epsilon \cdot (L\downarrow - \sigma \cdot T_{\text{SFC}}^4) + \text{QS} + \text{QL} + \text{QG} + \text{QPRC} = F_{\text{NET}}, \quad (3.1)$$

where the terms correspond to, from left to right, net short- and longwave radiation, turbulent fluxes of sensible and latent heat, the ground heat flux (composed of conduction and penetrating shortwave radiation) and the heat flux from precipitation. Following the convention in mass balance modelling, fluxes are defined as positive when energy transfer is to the surface. The residual energy flux, F_{NET} , constitutes the energy available for melt provided the surface temperature has reached the melting point. The specific mass balance is calculated from solid precipitation, surface vapour fluxes, surface and subsurface melt, and refreeze of liquid water in the snowpack. Surface vapour fluxes (M_v ; i.e. sublimation or deposition (kg m^{-2}) depending on the sign of QL) at each time step Δt are calculated according to

$$M_v = \frac{\text{QL} \cdot \Delta t}{L_H}, \quad (3.2)$$

where L_H is the latent heat of sublimation ($2.84 \times 10^6 \text{ J kg}^{-1}$) or vaporization ($2.51 \times 10^6 \text{ J kg}^{-1}$), depending on the surface temperature. The CMB model treats numerous additional processes, including the evolution of surface albedo and roughness based on snow depth and age; snowpack compaction and densification by refreeze; and the influence of penetrating solar radiation, refreeze and conduction on the near-surface englacial temperature distribution. Physical parameter values for snow and ice are provided in Table 3.1.

Table 3.1: Physical parameter values used in the CMB models.

Density (kg m^{-3})		
ice	915	–
whole rock	1496	Brock et al. (2010)
water	1000	–
Specific heat capacity ($\text{J kg}^{-1} \text{K}^{-1}$)		
air	1005	–
ice	2106	–
whole rock	948	Brock et al. (2010)
water	4181	–
Thermal conductivity ($\text{W m}^{-1} \text{K}^{-1}$)		
air	0.024	–
ice	2.51	–
whole rock	0.94	Reid and Brock (2010)
water	0.58	–
Surface roughness length (m^{-1})		
ice	0.001	Reid and Brock (2010)
debris	0.016	Brock et al. (2010)
Albedo		
ice	0.34	Brock et al. (2010)
firn	0.52	Brock et al. (2010)
fresh snow	0.85	Mölg et al. (2012a)
debris	0.13	Brock et al. (2010)
Emissivity		
ice/snow	0.97	Brock et al. (2010)
debris	0.94	Brock et al. (2010)

3.2.2 Inclusion of debris

For this study, the glacier CMB model was modified to include a treatment for supraglacial debris according to two cases: (1) one with no treatment of moisture fluxes or phase changes in the debris layer, congruent with previous studies (CMB-DRY); and (2) one that introduces a reservoir to parameterize the moisture content of the debris layer and its phase, and also includes a latent heat flux calculation (CMB-RES). The simulations are performed as point simulations, due to the availability of both meteorological-forcing and evaluation data at a single location.

3.2.2.1 Surface temperature

Consistent with previous modelling studies of debris-covered glaciers (e.g. Nicholson and Benn, 2006; Reid and Brock, 2010; Reid et al., 2012; Zhang et al., 2011), the model employs an iterative approach to simulating surface temperature, with the solution yielding zero residual flux in the surface energy balance (Eq. 1). The model uses the Newton–Raphson method to calculate T_{SFC} at each time step, as implemented in Reid and Brock (2010), with a different termination criteria of $|F_{\text{NET}}| < 1 \times 10^{-3}$. When snow or ice are exposed at the surface, the resulting T_{SFC} is reset to the melting point if it exceeds this value, and energy balance closure is achieved by using the residual energy for surface melt.

3.2.2.2 Subsurface temperature

Both versions of the CMB model calculates the temperature distribution in the upper subsurface following the conservation of energy. The vertical levels selected for the case study in Sect. 3.2.3 are defined in Table 3.2, and are set at fixed depths in the subsurface, from 0.0 to 9.0 m, that track the glacier surface as it moves due to mass loss or gain. On this grid, the 1-D heat equation is

$$\rho c \frac{\partial T}{\partial t} = \frac{\partial}{\partial z} \left(k \frac{\partial T}{\partial z} \right) + \frac{\partial Q}{\partial z}, \quad (3.3)$$

where ρ is the density (kg m^{-3}); c is the specific heat capacity ($\text{J kg}^{-1} \text{K}^{-1}$); T is the englacial temperature (K); k is the thermal conductivity ($\text{W m}^{-1} \text{K}^{-1}$); and Q is the heat flux due to non-conductive processes (penetrating shortwave radiation; W m^{-2}).

Table 3.2: Subsurface layer distribution and debris thickness used in this study.

Layers
Every 0.01 m from 0 to .24 m, 0.3, 0.4, 0.5, 0.8, 1.0, 1.4, 2.0, 3.0, 5.0, 7.0, 9.0 m
Debris thickness
0.23 m

For these simulations, the numerical scheme used to solve Eq. (3) was updated from a centred-difference approach to a Crank–Nicolson scheme, which was solved following Smith (1985). The greater stability of the numerics permits the subsurface layer spacing throughout the debris to be decreased to 1 cm from ~ 10 cm previously. The vertical grid spacing is thus consistent with the small number of previous studies that explicitly simulate heat conduction in the debris (Reid and Brock, 2010; Reid et al., 2012; Lejeune et al., 2013), rather than assume that the temperature gradient is approximately linear. The convergence of the numerical solution down to a vertical grid spacing of 1 mm was checked; however, the results did not strongly differ from the 1 cm case.

With the exception of Lejeune et al. (2013), the ice temperature in previous modelling studies has been assumed to be at the melting point, due to the focus on the ablation season (e.g. Nicholson and Benn, 2006; Reid and Brock, 2010). Although this assumption has been validated by field measurements (e.g. Conway and Rasmussen, 2000; Brock et al., 2010), it limits the temporal applicability of the model and may contribute to the overestimation of night-time surface temperatures when the overlying air temperature drops below the melting point (Reid and Brock, 2010). The CMB models explicitly simulate heat conduction throughout the glacier column. Therefore, the ice temperature is a prognostic variable at all levels except the bottom boundary, where a zero-flux condition is imposed. Finally, subsurface heating due to penetrating shortwave radiation is not considered when glacier debris is exposed at the surface (e.g. Reid and Brock, 2010).

3.2.2.3 Physical and thermal properties

The important physical properties of the glacier subsurface in Eq. (3) – density ρ , thermal conductivity k , and specific heat capacity c – are non-uniform with depth. Defining m_s and m_d as the levels corresponding to the bottom of the snowpack and debris layers (Fig. 3.1), respectively, the column properties (generalized as $f(z)$) are specified as

$$f(z) = \begin{cases} f_{\text{snow}} & z \leq m_s \\ f_{\text{deb}} & m_s < z \leq m_d \\ f_{\text{ice}} & z > m_d \end{cases} \quad (3.4)$$

Standard values are selected for snow and glacial ice properties (Table 3.1), with the exception of snow density, which is a prognostic variable. Within the debris layer, the properties of each 1 cm layer are a weighted average of the depth-invariant whole-rock values, f_{wr} , and the content of the pore space, f_ϕ , as determined by an assumed linear porosity function, ϕ :

$$f_{\text{deb}}(z) = \phi(z) \cdot f_\phi(z) + (1 - \phi(z)) \cdot f_{\text{wr}}. \quad (3.5)$$

For CMB-DRY, the debris pore space contains only air ($f_\phi = f_{\text{air}}$), while the weighted average in CMB-RES also considers the bulk water and ice content of the debris of saturated layers. The porosity function is discussed further in Sect. 3.2.3.

3.2.2.4 Moisture in the debris layer

For CMB-DRY, rainfall or other liquid water inputs are instantaneously removed as runoff from the debris layer and do not accumulate or contribute to vapour exchanges between the debris and the atmosphere, similar to previous modelling studies (e.g. Reid and Brock, 2010; Reid et al., 2012; Lejeune et al., 2013).

For CMB-RES, a reservoir is introduced for moisture accumulation and phase changes (Fig. 3.1). The reservoir depth for each column is calculated as the sum of the debris porosity over the debris thickness. Thus, the pore space in the debris is represented as a single reservoir, rather than the storage in each 1 cm layer being treated individually. Liquid water, from rainfall or melt of the overlying snowpack, instantly infiltrates the reservoir. The location of the water

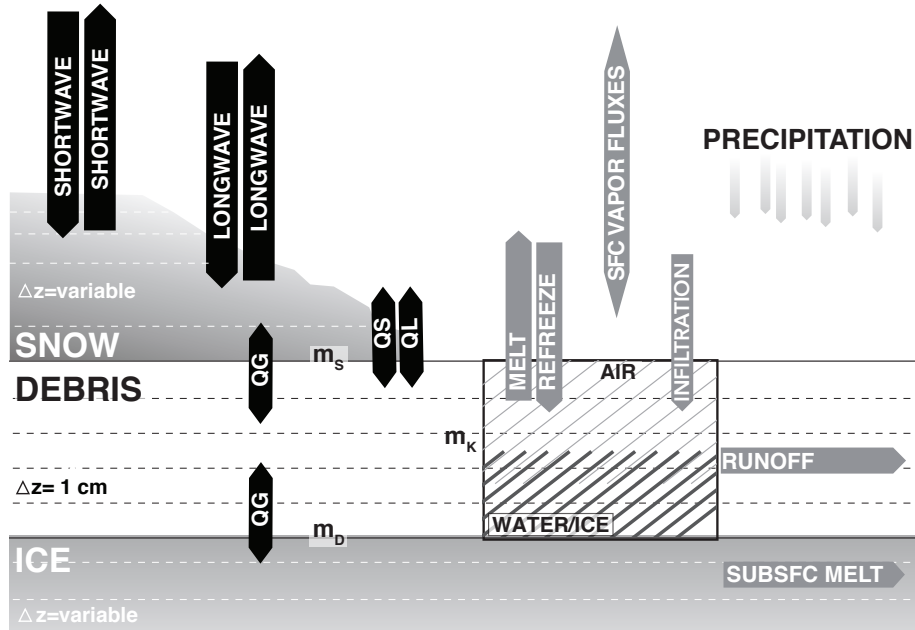


Figure 3.1: Schematic of the CMB-RES model and its treatment of the debris moisture content and its phase. The levels m_s , m_d , and m_k correspond to the bottom of the snowpack, the base of the debris layer, and the level of the saturated horizon, respectively.

and/or ice in the debris is not prognosed; rather, moisture is assumed to occupy the lowest debris layers, adjacent to the glacier ice.

In addition, when the ice–debris interface reaches the melting point, a minimum debris-water content is imposed to reflect field observations of a basal saturated layer during the ablation season (e.g. Nakawo and Young, 1981; Conway and Rasmussen, 2000; Kayastha et al., 2000; Reznichenko et al., 2010; Nicholson and Benn, 2012). As the water content of glacier debris cover is poorly constrained and no measurements are available, the minimum value is set to the amount of water needed to saturate the lowest 1 cm layer in the debris, given its porosity and ice content. The horizontal drainage of debris water is accounted for using a simplistic representation of the runoff timescale, which is a linear function of terrain slope and varies from 1 to 0 h^{-1} between 0° and 90° (Reijmer and Hock, 2008).

Congruent with the simple nature of the reservoir parameterization, the heat flux from precipitation is only applied at the surface in CMB-RES, and subsurface heat transport by water percolation is not included. This treatment is consistent with the findings of Sakai et al. (2004), namely that the heat flux due to rainfall percolation contributes minimally to subdebris

ice melt, although its influence may depend on debris permeability (Reznichenko et al., 2010).

3.2.2.5 Turbulent fluxes of latent and sensible heat

The turbulent fluxes of sensible heat (both models) and latent heat (CMB-RES) were computed using bulk aerodynamic formulae and corrected for atmospheric stability according to the bulk Richardson number, as is standard in glacier energy balance modelling (e.g. Braithwaite, 1995; Reid and Brock, 2010). The bulk Richardson number was constrained within reasonable limits following Fyffe et al. (2014), with the correction applied to fewer than 2.0% of total time steps in the simulations. The latent heat flux in CMB-DRY was set to zero, to be consistent with previous studies of debris-covered glaciers, as no measurements of surface relative humidity were available. For CMB-RES, the surface vapour pressure was needed but unknown.

For the case study described in Sect. 3.2.3, an automatic weather station (AWS) measured relative humidity at a height of $z_{\text{air}} = 2.16$ m, from which the partial vapour pressure was calculated. The density of water vapour was then obtained from

$$e_{\text{air}} = \rho_{\text{air}}^{\text{vap}} R_v T_{\text{air}}, \quad (3.6)$$

where the symbols correspond to, from left to right, the air's water vapour partial pressure, the partial density of water vapour, the specific gas constant for water vapour ($461.5 \text{ J kg}^{-1} \text{ K}^{-1}$), and the air temperature at a height of z_{air} . In this study, we assumed that $\rho_{\text{air}}^{\text{vap}}$ is constant between the sensor and the surface of the debris layer, i.e. that water vapour in the atmospheric surface layer is well mixed. The vapour pressure at the surface is therefore given by

$$e_{\text{sfc}}^* = \frac{e_{\text{air}} T_{\text{sfc}}}{T_{\text{air}}}. \quad (3.7)$$

For a completely unsaturated glacier debris layer in CMB-RES, a latent heat flux would nonetheless arise due to the vapour pressure gradient that results from the temperature difference between the surface and z_{air} . However, when water or ice are present in the debris, the final calculation of the surface vapour pressure, e_{sfc} , includes a linear correction towards the saturation value $e_{\text{sfc sat}}$ at T_{sfc} according to

$$e_{\text{sfc}} = e_{\text{sfc}}^* + (e_{\text{sfc sat}} - e_{\text{sfc}}^*) \cdot \left(1 - \frac{\Theta_{\text{air}}}{\phi_{\text{bulk}}}\right), \quad (3.8)$$

where e_{sfc}^* is the initial guess in Eq. (7); Θ_{air} is the void fraction of the bulk layer that is occupied by air; and ϕ_{bulk} is the bulk debris porosity, which is invariant under different debris thicknesses due to the linear specification of ϕ (as described in Sect. 3.2.3). Θ_{air} is given by

$$\Theta_{\text{air}} = \sum_{i=1}^{m_K} \frac{\phi_i}{N}, \quad (3.9)$$

where m_K is the level of the saturated horizon in the debris and N is the total number of layers in the debris. When the debris is completely unsaturated, $\Theta_{\text{air}} = \phi_{\text{bulk}}$, and when it is completely saturated, $\Theta_{\text{air}} = 0$.

Therefore, the surface vapour pressure in CMB-RES is a linear function of the moisture content of the reservoir rather than a wetted debris surface: as the reservoir fills from infiltration of rainfall or snowmelt, the distance between the surface and the saturated horizon (represented by Θ_{air}) decreases and e_{sfc} approaches saturation.

3.2.2.6 Mass balance

The total mass balance calculation in CMB-DRY and CMB-RES accounts for the following mass fluxes (kg m^{-2}) at each time step: solid precipitation, surface and vertically integrated subsurface melt, meltwater refreeze and formation of superimposed ice in the snowpack, changes in liquid water storage in the snowpack, and surface vapour fluxes. The contribution of surface vapour fluxes to or from the debris layer is zero when overlying snow cover is present and in CMB-DRY. In CMB-RES, these fluxes also contribute to changes in the debris water and ice content of the reservoir. For both models, subdebris ice melt is calculated as the vertical integral of melt in the ice column underlying the debris.

Liquid precipitation contributes indirectly to the mass balance in both CMB models through changes in storage in the snowpack, and contributes directly in CMB-RES via reservoir storage. However, changes in the debris water and ice content in CMB-RES are not included in the mass balance calculation, so as to allow for a more direct comparison between CMB-RES and CMB-DRY of the influence of including the latent heat flux. The impact of changes in the storage of water and ice in the debris is quantified in Sect. 3.3 and has a negligible influence on the total accumulated mass balance.

3.2.3 Miage Glacier case study

The study area is the Miage Glacier in the Italian Alps ($45^{\circ} 47' \text{ N}$, $6^{\circ} 52' \text{ E}$; Fig. 3.2). This glacier was selected due to the availability of meteorological data from an automatic weather station (AWS) located on the lower, debris-covered part of the glacier at an elevation of 2030 m a.s.l. The debris thickness was determined by a point measurement to be 23 cm. At the surface, the debris is composed mainly of coarse gravel and cobbles, ranging in size from a few centimetres to 25 cm, with occasional larger rocks, 1–2 m in size. The AWS site was deliberately chosen to be upwind from any nearby large boulders.

We performed two simulations, one for summer 2008 and one for fall 2011. The former covered the period of 25 June–11 August 2008, with the first 25 days discarded as model spin-up time. For much of the 2008 simulation, the AWS provided hourly values of air temperature, vapour pressure, wind speed, and incoming short- and longwave radiation (Fig. 3.3). However, during the spin-up period, wind speed and incoming longwave radiation were missing due to a programming error in the AWS. To provide this missing data, wind speed was generated synthetically using the hourly average from the measured data during the evaluation period. Incoming longwave radiation was obtained from the ERA-Interim reanalysis ($0.75^{\circ} \times 0.75^{\circ}$ resolution; Dee et al., 2011), using data from the closest model grid cell after interpolation from 12-hourly to hourly reference points. For the time period where both ERA-Interim and AWS data overlap (20 July–11 August 2008), the mean deviation (MD) and mean absolute deviation (MAD; ERA minus AWS) are ~ 13 and $\sim 35 \text{ W m}^{-2}$, with the deviation likely arising due to the difference between modelled and real terrain height of -450 m. Lastly, a rain gauge was not installed at the AWS site in 2008. We therefore used input data from another AWS located 4 km away (denoted as AWS2 in Fig. 3.2) and assumed that they were representative of conditions at the AWS on the Miage Glacier.

The 2008 simulation was intended to coincide with a supplementary field measurement program. Between 20 July and 11 August, surface temperature and the turbulent fluxes of latent and sensible heat were measured. The first field was measured with a CNR1 radiation sensor (Kipp & Zonen, Delft, the Netherlands), while the latter two fluxes were measured by an eddy covariance (EC) station. This comprised a CSAT three-dimensional sonic anemometer

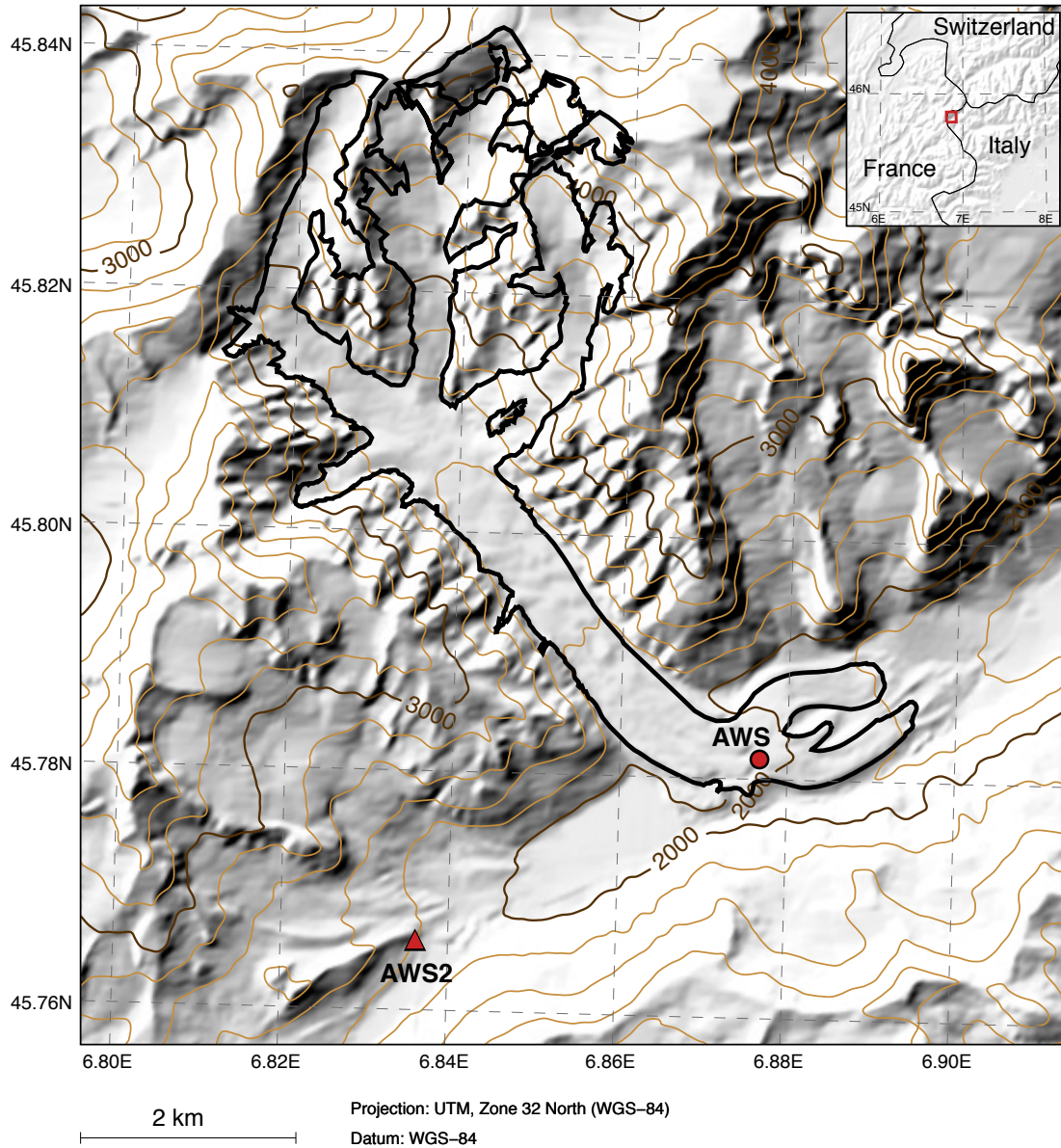


Figure 3.2: Map showing the location of the Miage Glacier. The AWS located on the glacier is denoted with a red circle and the AWS2 from which precipitation data were obtained is shown by a red triangle.

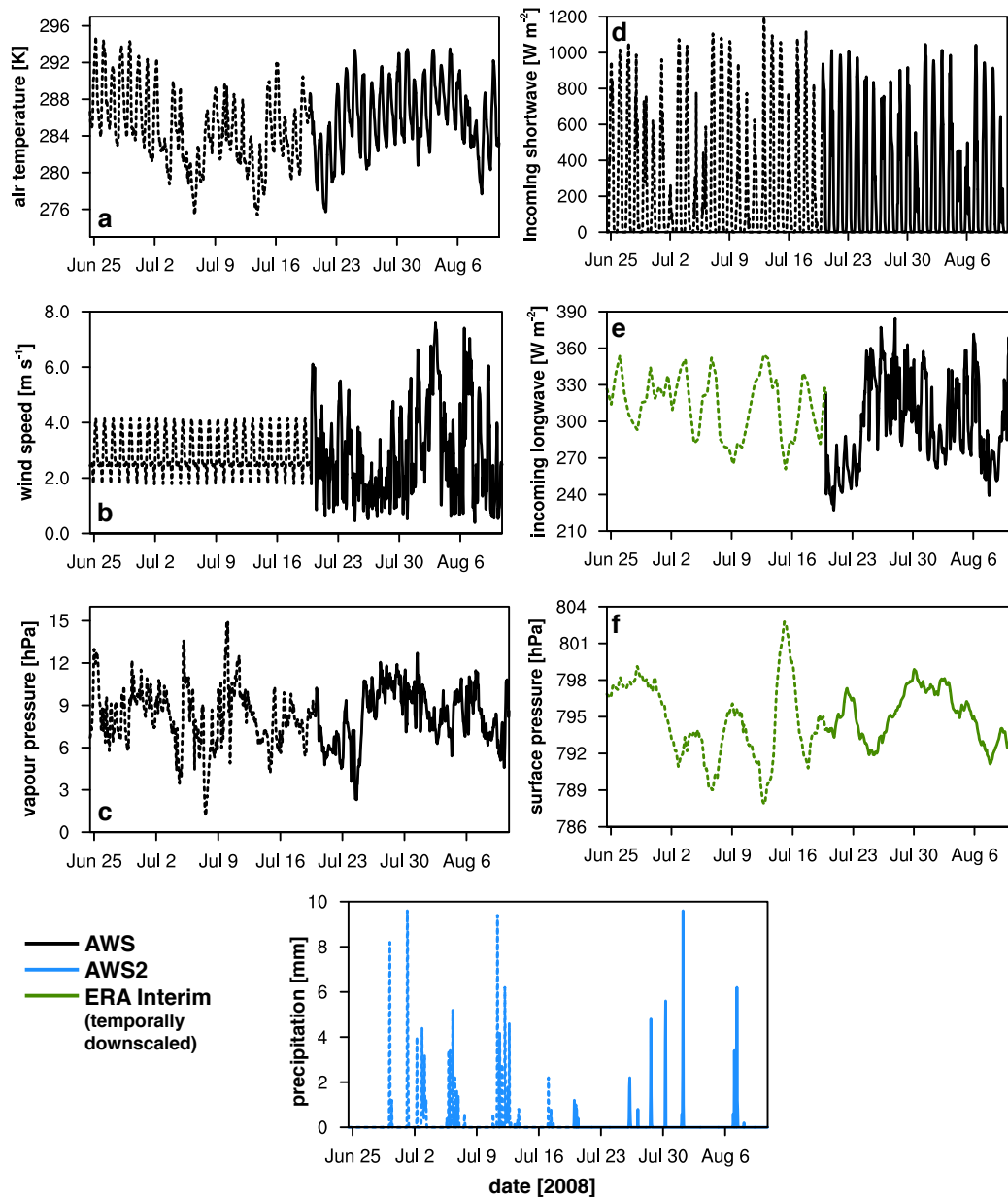


Figure 3.3: Time series from the 2008 simulation of the forcing variables of (a) 2 m air temperature (K), (b) wind speed (m s^{-1}), (c) 2 m vapour pressure (hPa), (d) incoming shortwave radiation (W m^{-2}), (e) incoming longwave radiation (W m^{-2}), (f) surface pressure (hPa), and (g) precipitation (mm). Data from the AWS on the Miage Glacier are shown in black, from the second AWS (4 km away) in blue, and temporally downsampled from the ERA-Interim reanalysis in green. Dashed curves indicate the discarded spin-up period, while solid curves indicate the simulation time.

and KH₂O Krypton Hygrometer (both Campbell Scientific Limited, Shephed, UK), installed at a height of 2 m above the debris surface. These sensors measured the three components of turbulent wind velocity, virtual temperature and water vapour concentrations at an interval of 50 ms. Raw data were processed using Campbell Scientific OPEC software, which included a “WPL” (Webb–Pearman–Leuning) correction for density effects (Webb et al., 1980) and 30 min averages of the 50 ms scans were stored. The data were filtered for outliers using three times their standard deviation before being used for evaluation (Brock et al., 2010). Surface temperature was calculated from the upwelling longwave radiation recorded by the CNR1, using an emissivity of 0.94. The AWS tripod provided a stable platform on the slowly melting glacier surface, although the possibility of tilting of the instrument mast cannot be excluded. These measurements provide a unique data set with which to evaluate the CMB models using direct measurement of turbulence in the surface atmospheric layer above a debris-covered glacier.

However, the 2008 simulation does not contain any phase changes, since the air temperature remained above freezing (cf. Fig. 3.3a). In order to fully demonstrate the model capabilities, we performed a second simulation from 6 June to 11 October 2011, discarding all but the period of 14 September–11 October as model spin-up time, due to the focus on the influence of phase changes. We focused our analysis on two freezing events, from 18 to 19 September and 7 to 9 October 2011. Incoming longwave radiation, precipitation and mean wind speed were available hourly from the AWS (forcing data not shown), and measured surface temperature data, estimated from the upwelling longwave radiation recorded by the CNR1, were available for model evaluation.

A final forcing variable for the calculation of the debris surface energy balance, surface pressure, was missing for both the 2008 and 2011 simulations. These data were obtained from the ERA-Interim reanalysis, at 6-hourly temporal resolution, and again from the closest grid cell. A correction was applied for the difference between the real and modelled terrain height using the hypsometric equation, assuming a linear temperature gradient calculated from the AWS and the air temperature on the first model level in the ERA-Interim. For both simulations, the same subsurface layer spacing was used and is provided in Table 3.2. The englacial temperature profile was initialized at the melting point, since both simulations began in June. Uncertainties

in the temperature initialization were addressed by the inclusion of long spin-up periods.

For both CMB-DRY and CMB-RES, we assumed that the debris porosity was a linear function of depth in the debris, decreasing from 40 % at the surface down to 20 % at the debris-ice interface. A range of 19–60 % percent void space by volume was measured on the Miage Glacier, by placing a known volume of surface debris in a graduated bucket and measuring the volume of water required to fill the air spaces (Brock et al., 2006). For this study, we used an upper bound of 40 %, such that the bulk porosity (30 %) was consistent with other reported values for glacier debris (Nicholson and Benn, 2012). A sensitivity study using the measured upper bound of 60 % showed that while subdebris ice melt was strongly affected (it decreased by $\sim 17\%$ in both simulations), the CMB model behaviour and the main results presented in Sect. 3 remained intact. Other physical and thermal properties of the column were either taken from field measurements or specified from values used in previous modelling studies of this glacier (e.g. Reid and Brock, 2010). The porosity value of 20 % in the lowest 1 cm layer in the debris gave a minimum water content of 2 kg m^{-2} that was imposed only when the subdebris ice was at the melting point. Subdebris ice melt changes by $\pm 1.8\%$ if the minimum value is removed or doubled in the 2008 simulation.

A slope of 7° at the AWS gives a runoff timescale of 0.92 h^{-1} . This simple representation of runoff timescales does not consider contributions from upslope regions in the glacier; however, we feel that this is an appropriate first step given that horizontal transport of water within the debris is poorly constrained and no measurements are available. Varying the runoff timescale by $\pm 4\%$ (equivalent to changing the slope from 4° to 10°) results in small changes in total accumulated mass balance and subdebris ice melt during the summer 2008 simulation, of less than ± 0.6 and $\pm 0.4\%$, respectively. The results in the transition season of fall 2011 are more sensitive, with changes in these variables of up to ± 1.0 and $\pm 2.0\%$, respectively.

Finally, although the CMB models are evaluated against a short summer period in 2008 and in fall 2011, they are applicable throughout the annual cycle and to glaciers of any temperature regime, as illustrated in Fig. 3.1.

Table 3.3: Mean deviation (MD), mean absolute deviation (MAD), and R value for the evaluation variables of surface temperature (T_{sfc}), and the turbulent fluxes of sensible (QS) and latent heat (QL).

2008		CMB-DRY	CMB-RES
T_{sfc}	MD	-0.5	-1.1
	MAD	2.3	2.4
	R	0.94	0.94
QS	MD	-65.2	-47.0
	MAD	71.1	54.2
	R	0.91	0.92
QL	MD	23.9	1.0
	MAD	28.2	19.1
	R	-	0.52
2011		CMB-DRY	CMB-RES
T_{sfc}	MD	1.1	0.9
	MAD	1.9	1.7
	R	0.97	0.97

3.3 Results

3.3.1 Comparison with in situ measurements

The surface temperatures (T_{sfc}) simulated by CMB-DRY and CMB-RES are in good agreement with measurements for both the 2008 and 2011 simulations (Fig. 3.4a,d; Table 3.3). The models tend to underestimate daily maximum temperatures in 2008 and night-time radiative cooling in 2011. However, for both simulations, the models reproduce the diurnal cycle and its variability well. The CMB models also capture the variability of the sensible heat flux (QS), but the simulated magnitude of heat transfer to the overlying atmosphere is greater than reported by the EC station (Fig. 3.4b). The overestimation of QS for the CMB-DRY run is in part attributable to the lack of latent heat flux (QL), which means that an average energy loss of $\sim 24 \text{ W m}^{-2}$ is not captured (Fig. 3.4c; cf. Table 3.3). CMB-RES has a greatly reduced but still non-negligible bias in QS, again, in part, because evaporative cooling is underestimated, by $\sim 6 \text{ W m}^{-2}$. The smaller simulated latent heat flux compared with the EC data results from the approach used to estimate surface vapour pressure (cf. Sect. 3.2.2), which produces an average gradient of only -0.5 hPa m^{-1} between the surface and overlying air (Fig. 3.5a).

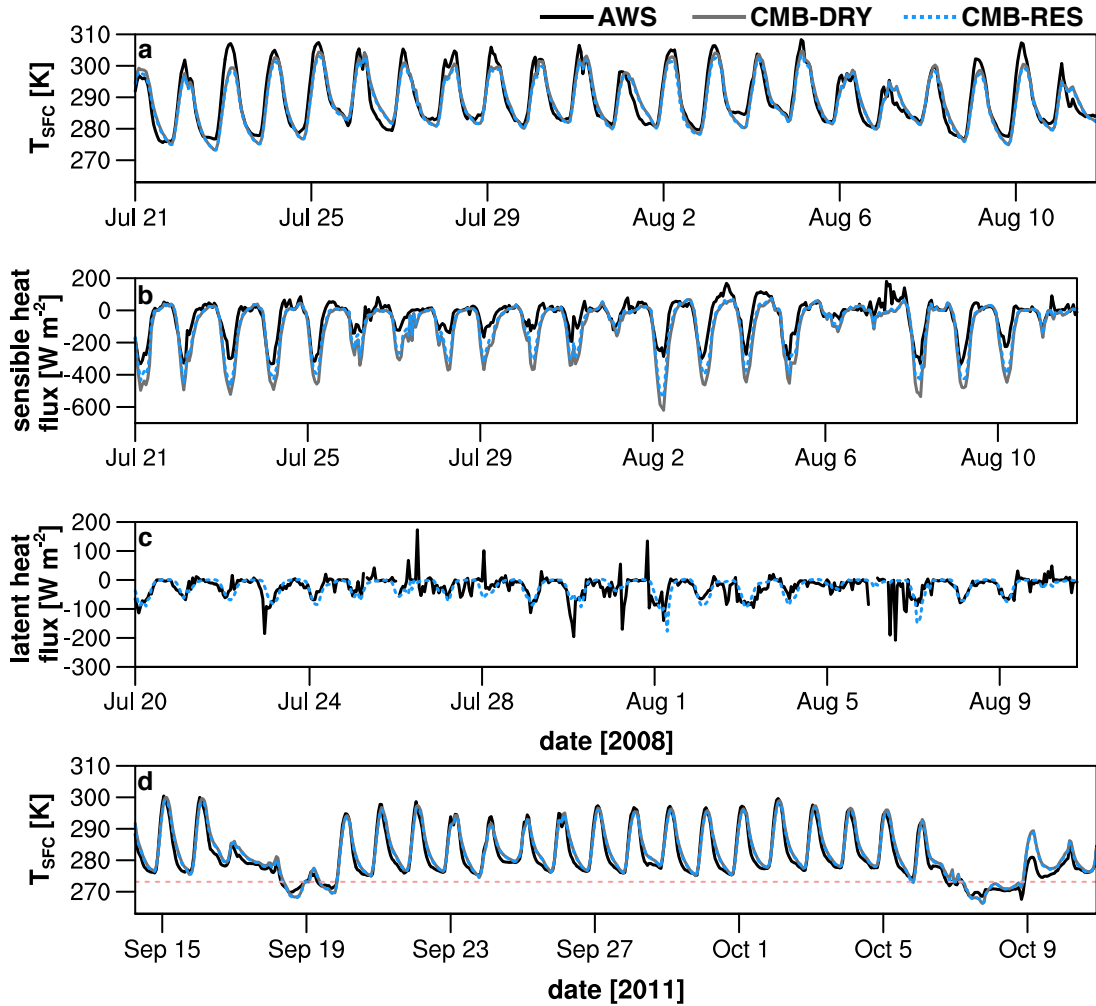


Figure 3.4: Time series from the 2008 simulation of (a) debris surface temperature (T_{sfc} ; K) and the turbulent fluxes of (b) sensible and (c) latent heat (W m^{-2}), for measurements (black curve), CMB-DRY (dark grey curve), and CMB-RES (blue, dashed curve). (d) Same as panel a, but for the 2011 simulation. The horizontal dashed red line indicates the freezing point, 273.15 K.

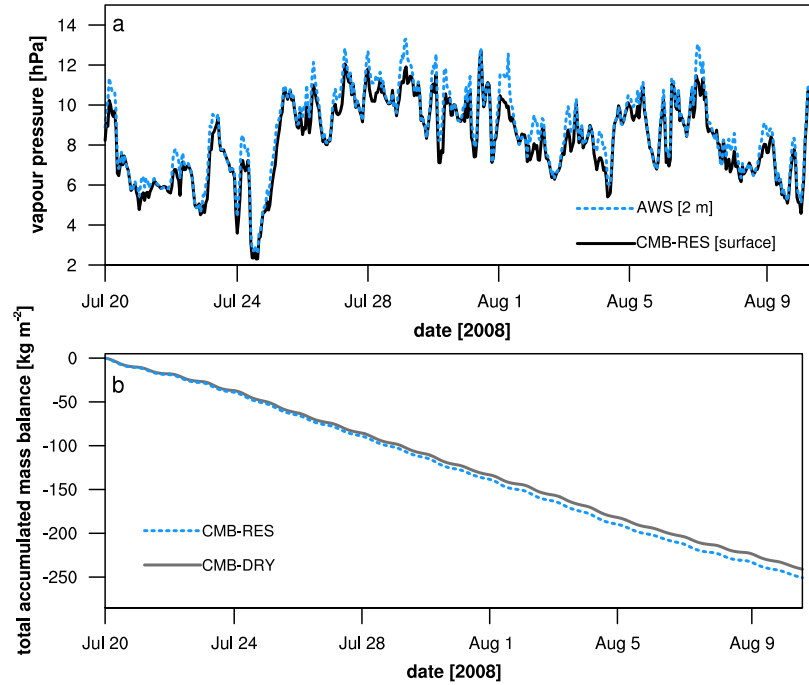


Figure 3.5: Time series from the 2008 simulation of (a) surface (dashed-blue curve) and 2 m air (black curve) vapour pressure (hPa) in CMB-RES, and (b) total accumulated mass balance (kg m^{-2}) for CMB-DRY (solid-grey curve) and CMB-RES (dashed-blue curve).

3.3.2 Modelling insights from the 2008 simulation

In total, the influence of the reservoir parameterization on the accumulated mass balance between 20 July and 11 August 2008 is small, increasing from -241.0 kg m^{-2} in CMB-DRY to -250.6 kg m^{-2} in CMB-RES (Fig. 3.5b). These values are equivalent to an ablation rate of approximately $11 \text{ mm w.e. d}^{-1}$ (w.e. water equivalent), which is in order of magnitude agreement with the value of $22 \text{ mm w.e. d}^{-1}$ reported by Fyffe et al. (2012) for the Miage Glacier, based on the entire ablation seasons of 2010 and 2011.

The mass fluxes underlying the simulated mass balance signal are determined by the surface energy balance, whose daily-mean components are shown in Fig. 3.6a for CMB-RES. Energy receipt, mainly through net shortwave radiation, is generally counteracted by energy losses through net longwave radiation, heat conduction (QC), and the turbulent fluxes QL and QS. The heat flux to the debris surface from precipitation (QPRC) has an average value of -12.5 W m^{-2} during rainfall events. However, since the precipitation temperature is assumed to be the same as

Table 3.4: Average-energy and accumulated-mass fluxes at the surface over the 2008 simulation for CMB-RES and CMB-DRY.

Average (W m^{-2})	CMB-DRY	CMB-RES
net shortwave (SWnet)	237.6	237.6
net longwave (LWnet)	-91.0	-87.8
conduction (QC)	-41.5	-40.1
sensible heat (QS)	-104.2	-86.0
latent heat (QL)	-	-22.9
precipitation (QPRC)	-0.9	-0.7
Sum (kg m^{-2})	CMB-DRY	CMB-RES
melt	-	0.
refreeze	-	0.
sublimation	-	0.
deposition	-	0.
evaporation	-	17.3
condensation	-	0.1
subdebris ice melt	241.3	233.8

T_{air} , QPRC is a stronger energy sink for daytime rainfall. These energy fluxes produce ablation that is dominated by subdebris ice melt and evaporation over the evaluation period (Fig. 3.6b; Table 3.4). Surface melt, refreeze, sublimation and deposition are zero, since there is no solid precipitation and both the debris surface and internal temperatures remain above the melting point.

Compared with CMB-DRY, CMB-RES simulates slightly lower daytime debris-surface temperatures, as a result of heat extraction by QL (cf. Fig. 3.4a, Table 3.3). Energy transfer to the debris-ice interface is therefore also lower, contributing to a small reduction in subdebris ice melt, of 7.5 kg m^{-2} (Table 3.4). However, the reduction in melt is more than compensated by surface vapour fluxes, with a total of 17.3 kg m^{-2} of evaporation over the evaluation period. Evaporation dominates during the day (95 % of the total), while smaller amounts of condensation occur mainly at night (64 %) or in the early morning.

Water accumulates in the supraglacial debris after rainfall events and is then removed, mainly by horizontal drainage but also by evaporation (Fig. 3.7). The total accumulated mass balance is negligibly altered if changes in debris-water content are considered in addition to surface vapour fluxes. Both models treat the physical properties of the debris layer – thermal conductivity,

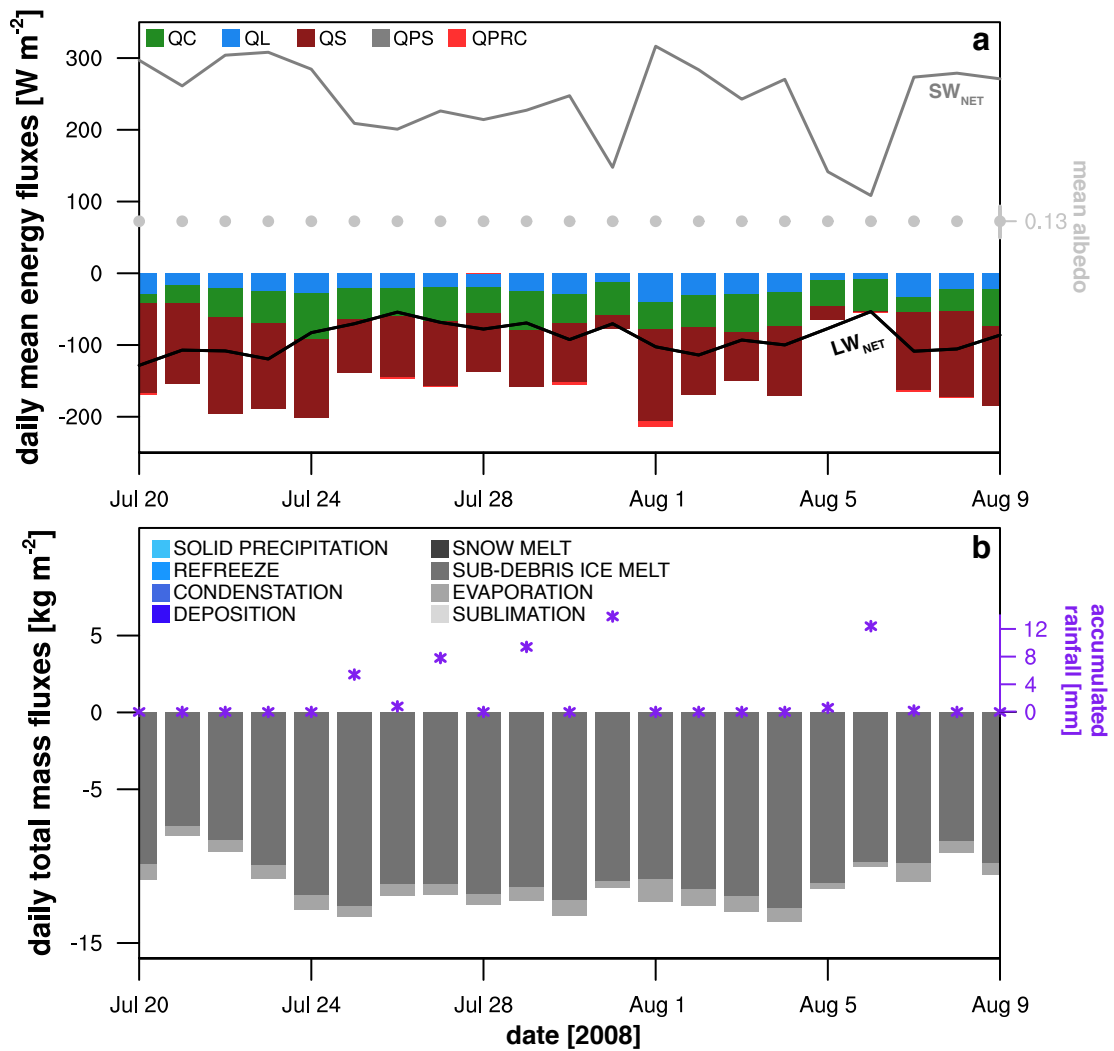


Figure 3.6: CMB-RES values for (a) daily mean energy fluxes over the evaluation period (W m^{-2}). The grey curve is net shortwave radiation, the black curve is net longwave radiation, and the grey dots show daily-mean surface albedo, which remains constant at the debris value because there is no solid precipitation. (b) Daily total mass fluxes (kg m^{-2}). Maximum daily values of evaporation and condensation are 1.4 and 0.02 kg m^{-2} , respectively, although the latter flux is not visible. Note that while daily-accumulated rainfall is shown (purple asterisks), it is not technically a mass flux, since the mass balance calculation in CMB-RES does not account for debris-water storage. Rather, this field is plotted to show its correspondence with other fields, such as net shortwave radiation.

density, and specific heat capacity – as functions of depth. Figure 3.8a–c show their variation with depth for “dry” conditions, when there is no significant debris-water storage, and for “wet” conditions, when there is significant water present, as a result of rainfall. “Dry” conditions prevail, comprising 76 % of the evaluation period (Fig. 3.8d–f), under which, as the porosity decreases with depth, the debris thermal conductivity and density increase while the specific heat capacity decreases. The debris physical properties in CMB-DRY and CMB-RES are the same, with the exception of the bottom layer adjacent to the debris–ice interface, which remains fully saturated in CMB-RES, as a result of the moisture source term described in Sect. 3.2.2. Water present in this layer acts to increase all three properties compared with CMB-DRY. Rainfall events and the associated moisture storage extend this influence upwards through the debris layer, with a significant alteration to the fully saturated layers (spanning the depth between 20 and 23 cm for the “wet” sample time slice) and a smaller effect on the partially saturated layer (at a depth of 19 cm). The debris-specific heat capacity is the most strongly affected physical property, since the value of water is approximately four times that of air (4181 vs. 1005 J kg⁻¹ K⁻¹).

The effective thermal diffusivity of the debris is inversely proportional to the specific heat capacity and the debris density. Increases in both these quantities, but particularly in the former, reduce heat diffusion over affected layers compared with CMB-DRY. Therefore, in combination with heat extraction by QL, the change in subsurface physical properties reduces the amplitude and depth penetration of the diurnal temperature cycle in the debris layer (Fig. 3.9). Fluctuations in the magnitude of QL have a correlation coefficient of 0.78 with the temperature difference between CMB-RES and CMB-DRY in the top 6 cm of the debris, while reductions in the effective thermal diffusivity have a correlation coefficient of 0.6 with the temperature difference in the bottom 6 cm.

3.3.3 Impact of phase changes in the 2011 simulation

Two freezing events occur during the 2011 simulation, between 18 September 23:00 LT (local time) and 19 September 14:00 LT and between 7 October 09:00 LT and 9 October 09:00 LT, at the end of two precipitation events with subzero air temperatures (cf. Fig. 3.4d). Energy

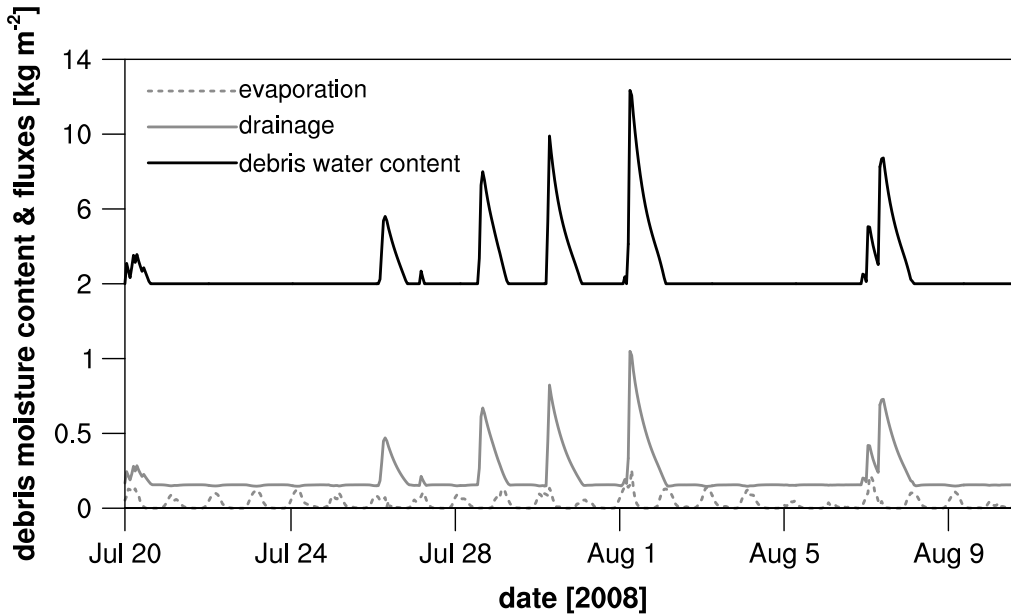


Figure 3.7: Time series of total debris-water content (black curve) as well as the two sources of debris-water loss: horizontal drainage (solid-grey curve) and evaporation (dashed-grey curve). Units are in kilograms per square metre (kg m^{-2}).

and mass fluxes for this simulation are summarized in Table 3.5. Net longwave and shortwave radiation are reduced, due to cooler surface temperatures and to small amounts of snowfall that increase the surface albedo (Fig. 3.10a). Rapid melt of the thin overlying snow cover (< 0.5 cm) and infiltration of rainfall at the beginning of the precipitation events provide the source water for refreeze in the debris (Figs. 3.10b, 3.11a). During the first event, a maximum of 1.0 kg m^{-2} of ice is produced, which persists in the basal debris layer for a further 3 days after the last time step with refreeze. In the second event, the debris ice content reaches 1.4 kg m^{-2} , and does not melt away before the end of the simulation.

The bulk presence of liquid water and ice in the debris layer influences the vertical temperature profile in two competing ways (Fig. 3.11b–d). Latent heat release due to refreezing warms the subsurface, on average by 0.3 K but exceeding 0.7 K for the hourly time steps with the greatest refreeze rates. However, the presence of ice in saturated basal layers constrains the maximum debris temperature to the melting point. In combination with a reduction in the effective thermal diffusivity of saturated layers, the modulation of debris temperature results in a decrease in subdebris ice melt of 7.0% in CMB-RES compared to CMB-DRY.

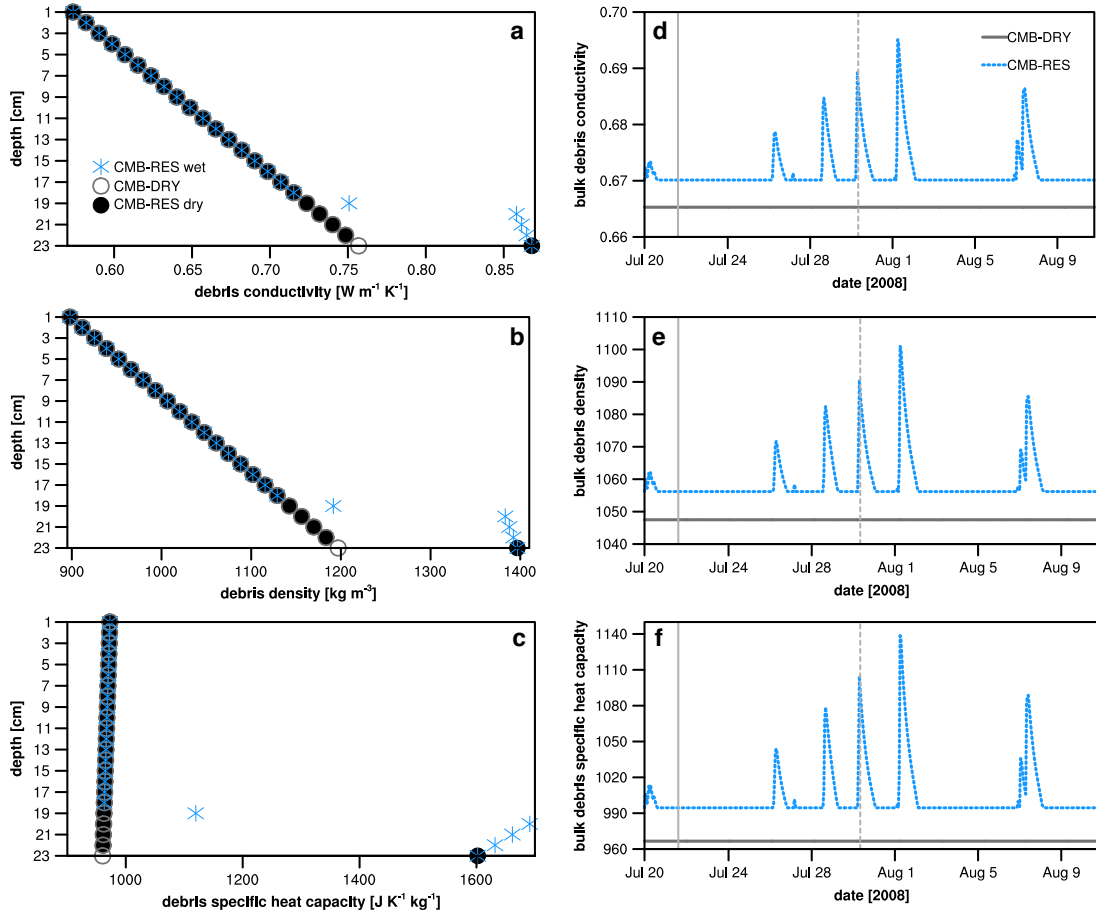


Figure 3.8: Depth variation of (a) debris thermal conductivity ($\text{W m}^{-1} \text{K}^{-1}$), (b) density (kg m^{-3}), and (c) specific heat capacity ($\text{J kg}^{-1} \text{K}^{-1}$), shown for CMB-DRY in grey-unfilled circles and for CMB-RES in both black-filled circles (“dry” time slice) and blue asterisks (“wet” time slice). Time series of bulk values for these same properties are shown in panels (d–f) for CMB-RES in blue and CMB-DRY in grey. The locations of the “dry” and “wet” time slices are indicated by the first (solid grey) and second (dashed grey) reference lines on the x axis, respectively.

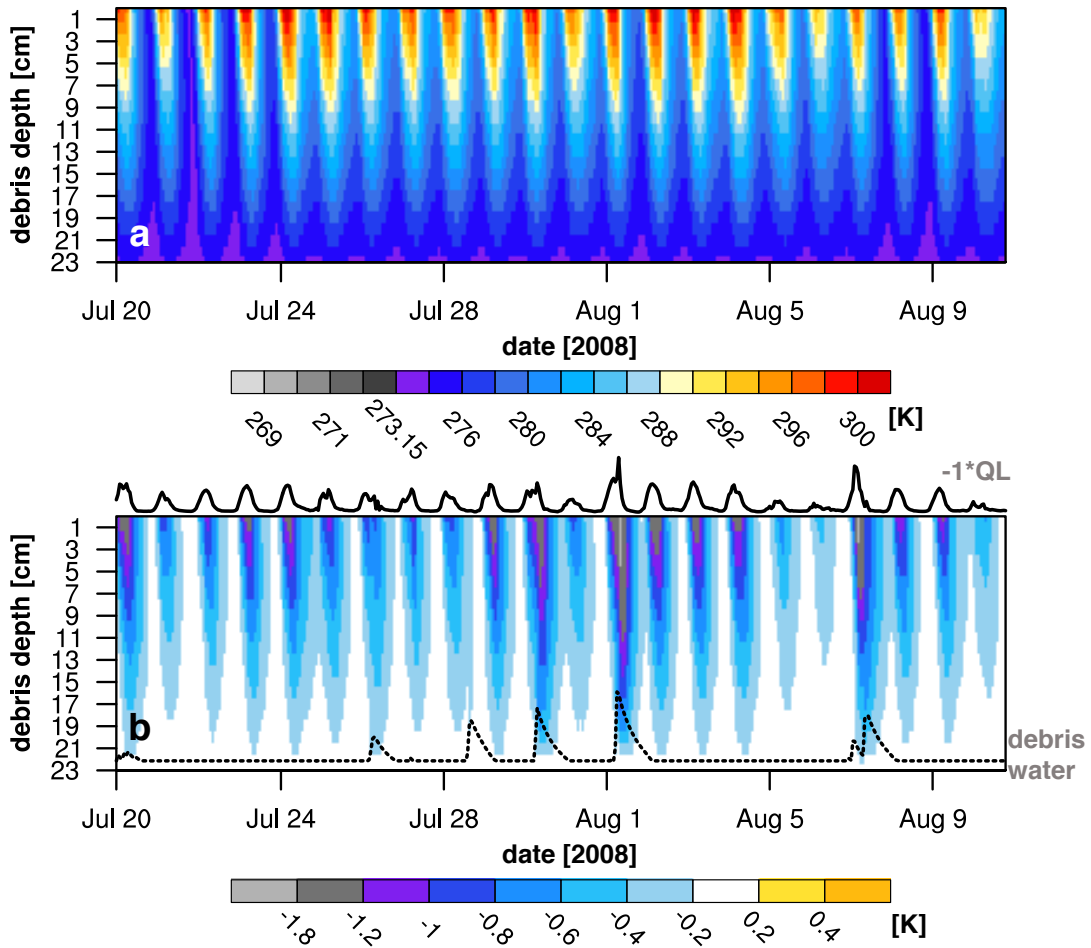


Figure 3.9: Temporal and depth variation of (a) CMB-RES debris temperature and (b) the difference between the model runs (CMB-RES minus CMB-DRY). Units are in Kelvin (K). For reference, $-1*QL$ (solid-black curve; now positive for energy loss from the surface) and debris-water content (black dashed) are plotted without y axes in panel (b). The height of the debris-water curve shows the estimated level of moisture in the reservoir.

Table 3.5: Average-energy and accumulated-mass fluxes at the surface over the 2011 simulation for CMB-RES and CMB-DRY.

Average (W m^{-2})	CMB-DRY	CMB-RES
net shortwave (SWnet)	133.0	133.0
net longwave (LWnet)	-80.2	-78.8
conduction (QC)	-23.0	-22.4
sensible heat (QS)	-27.0	-20.0
latent heat (QL)	-	-9.8
precipitation (QPRC)	-0.1	-0.1
Sum (kg m^{-2})	CMB-DRY	CMB-RES
melt	4.6	4.4
refreeze	0	0
sublimation	0.2	0.5
deposition	0	0
evaporation	-	8.6
condensation	-	0.1
subdebris ice melt	172.4	160.4

The accumulated mass balance between 14 September–11 October 2011 is -172.4 kg m^{-2} for CMB-DRY and -168.8 kg m^{-2} for CMB-RES. Changes in water and ice storage again have a negligible impact on simulated mass balance, resulting in a further ablation of 0.2 kg m^{-2} . Thus, for the fall transition season, surface vapour fluxes do not compensate for the reduction in subdebris ice melt due to the thermodynamic influence of ice in the debris. However, considering the same summer period in 2011 as in 2008 (20 July–11 August), the percent changes in accumulated mass balance and subdebris ice melt are +4.0 and -3.2% , respectively, consistent with the findings of the 2008 simulation. Therefore, the influence of the reservoir parameterization varies seasonally.

3.4 Discussion

Both the observed and simulated QL are non-zero over the simulation period, with regular fluctuations on the order of 10 W m^{-2} and occasional spikes of more than $\pm 100 \text{ W m}^{-2}$ (after filtering, as described in Sect. 3.2.3; cf. Fig. 3.4c). Among other sources of error, intense precipitation can cause erroneous spikes in the EC measurements, as a result of raindrops interfering with the path of the sonic anemometer (e.g. Aubinet et al., 2012). However, of the 15 occur-

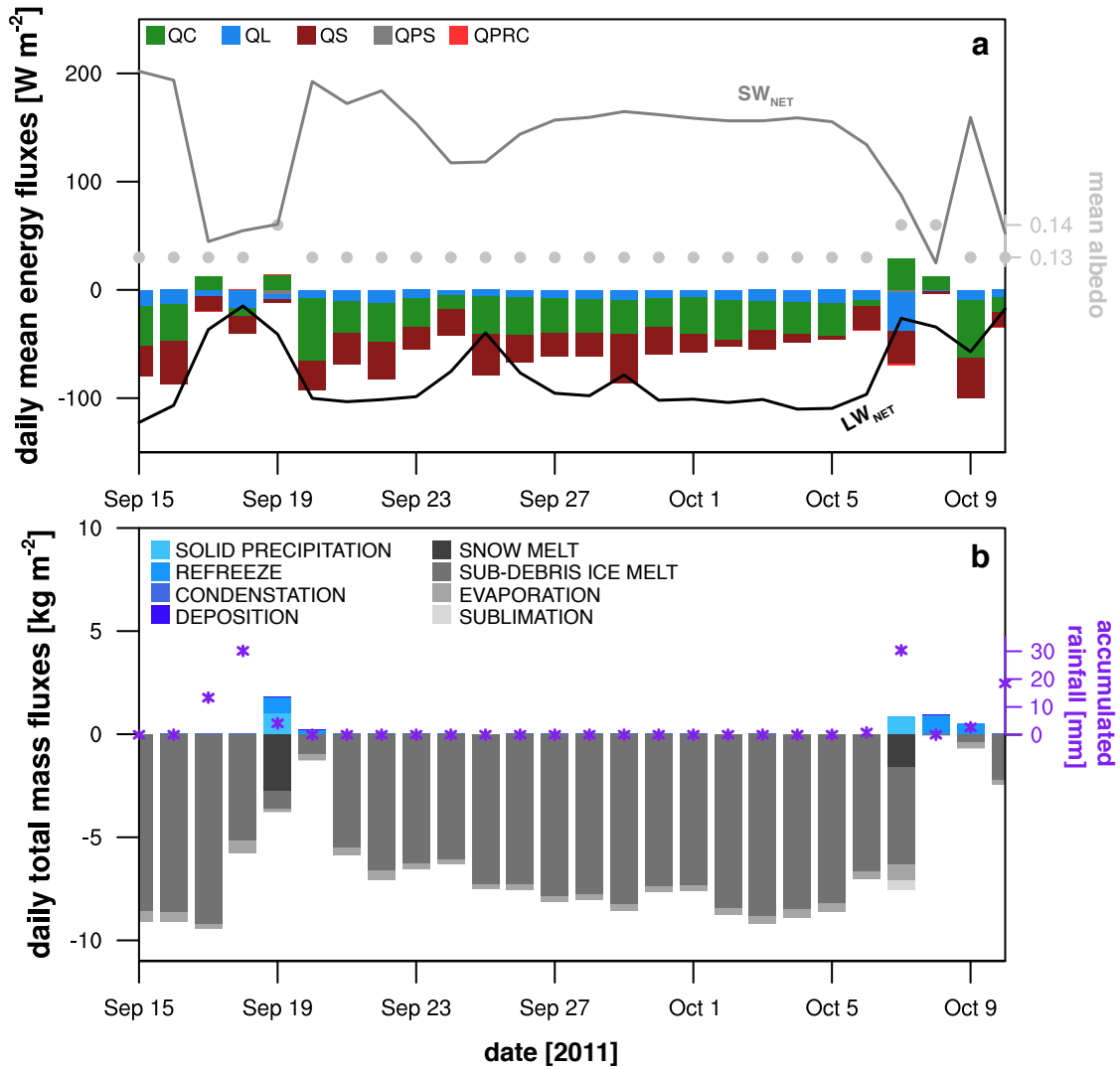


Figure 3.10: Same as Fig. 3.6 but for the 2011 simulation.

rences of spikes greater than $\pm 100 \text{ W m}^{-2}$ in the EC data, only two occur during or within 1 hour of precipitation. Given previously reported large QL values (up to -800 W m^{-2} during rainfall events on heated debris; Brock et al., 2010), neglecting QL in a surface energy balance calculation can be inappropriate, and under certain meteorological conditions is likely to have a significant impact on the calculated energy fluxes.

The difference in accumulated mass balance between CMB-RES and CMB-DRY is relatively small, for a point application in this configuration. However, the daily mean evaporation rate was $\sim 0.9 \text{ mm w.e.}$ in 2008 (June–early August) and $\sim 0.6 \text{ mm w.e.}$ in 2011 (June–September),

which is comparable to values reported for clean glaciers (e.g. Kaser, 1982). Scaled up to a larger debris-covered area, evaporation would represent a significant mass flux. Furthermore, the presence of debris ice, even in small amounts, has an important thermodynamic influence by suppressing subdebris ice melt, with implications for dry simulations of debris-covered glaciers in or close to transition seasons.

The simulated QL and surface vapour fluxes depend on the estimate of the surface vapour pressure, which is an important source of uncertainty in the CMB-RES model. In unsaturated soil sciences, the relative humidity is often treated as an exponential function of the liquid water pressure in the pore space using the thermodynamic relationship of Edlefsen and Anderson (1943) (e.g. Wilson et al., 1994; Karra et al., 2014). However, testing an exponential relationship with the moisture content of the debris in CMB-RES resulted in strong biases in QL (MD = 28; MAD = 96 W m^{-2}) and a shift from QL as an energy sink to a gain, which was inconsistent with the EC data. For simplicity, we employed a linear approach, and there may be some support for this treatment in coarser texture soil, as Yeh et al. (2008) found that the effective degree of saturation in sand decreased approximately linearly in the top 2 m above the water table.

In reality, water vapour fluxes occur at the saturated horizon, either at the surface or within the debris layer. However, in the 2008 simulation, the mean depth of the saturated horizon was 21.5 cm, where the proximity of glacier ice damped temperature fluctuations and constrained the mean temperature to $\sim 275 \text{ K}$. Therefore, computing vapour fluxes at this level produced a very small latent heat flux, of -3.1 W m^{-2} on average, that was also not in agreement with the EC data. CMB-RES likely provides an underestimate of the simulated location of the saturated horizon, since capillary action was not taken into account. For fine gravel soils (grain size of 2–5 mm), capillary rise is on the order of a few centimetres (Lohman, 1972), while for coarser, poorly sorted glacier debris, the effect may be smaller. Underestimation of the height of the saturated horizon, and therefore of both the debris temperature and the saturation vapour pressure, is consistent with the small latent heat flux when vapour fluxes are computed at this level. As a part of future work, there is a need to accurately compute the vapour fluxes at the level of the saturated horizon.

In addition to neglecting capillary action, CMB-RES also does not account for many inter-

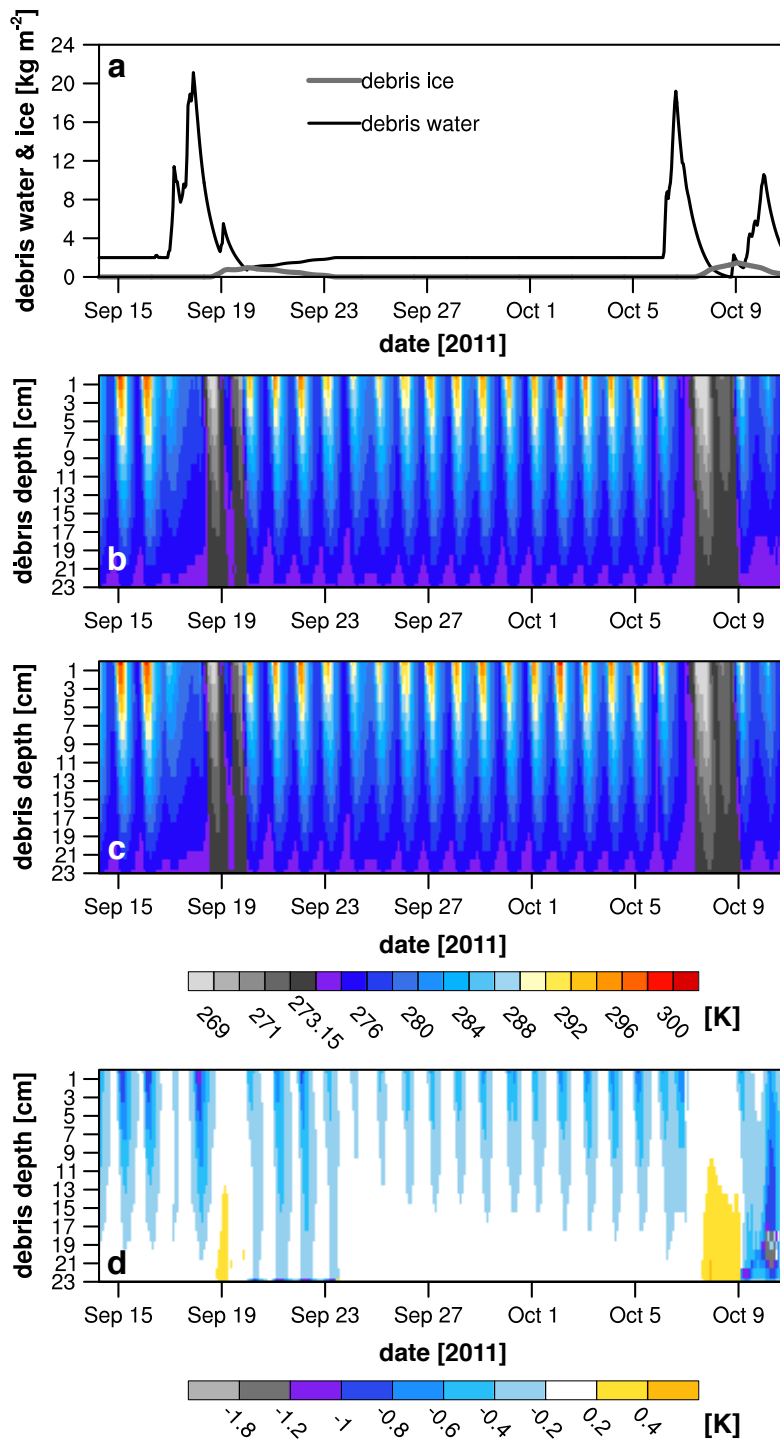


Figure 3.11: (a) Time series from the 2011 simulation of the debris water (black line) and ice (grey line) content (kg m^{-2}). Temporal and depth variation of the debris temperatures in (b) CMB-RES and (c) CMB-DRY, and (d) the difference between the model runs (CMB-RES minus CMB-DRY). Units are in Kelvin (K).

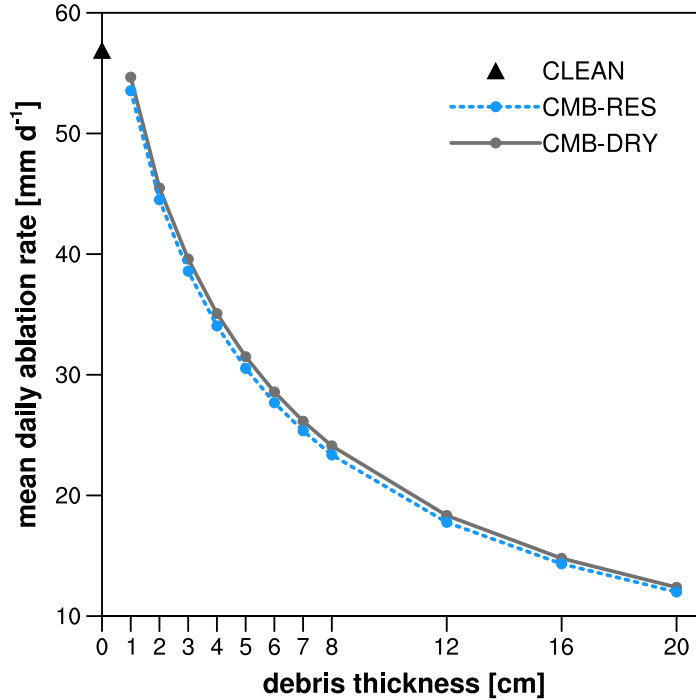


Figure 3.12: Daily mean subdebris ice ablation rate (mm w.e. d^{-1}) vs. debris thickness (cm), produced by the CMB models using the forcing data from the 2008 simulation. The clean-ice-melt rate is represented by a black triangle. CMB-DRY is the solid-grey curve and CMB-RES is the dashed-blue curve.

nal physical processes that have been highlighted in unsaturated soil sciences, including water vapour flow due to gradients in concentration and temperature, liquid water flow in response to hydraulic gradients, volume changes due to changes in the degree of saturation (e.g. Sheng, 2011), deposition of water vapour and its contribution to the formation of thin ice lenses (e.g. Karra et al., 2014), and heat or moisture advection as a result of airflow (e.g. Zeng et al., 2011). However, incorporation of these processes into CMB-RES is currently limited by a lack of appropriate evaluation data. Instead, we focus on including processes related to phase changes, which have been demonstrated to have an impact on the subsurface temperature field and ablation rate (Reznichenko et al., 2010; Nicholson and Benn, 2012). As a part of future work, CMB-RES could be improved by distinguishing the location of debris ice and water separately within saturated layers, thus potentially improving the simulated debris temperature profiles, as the melting point constraint would only be applied to saturated layers containing ice.

The magnitude of QS is sensitive to the choice of debris thickness, which was selected to be 0.23 m in this study based on a point measurement. However, the turbulent fluxes measured by the EC station respond to a larger area, with a variable and unknown debris thickness that likely ranges between 20 and 30 cm. The agreement between measured and modelled QS in 2008 is improved if the debris thickness in the models is reduced slightly. For example, using a thickness of 20 cm reduces the MD and the MAD by $\sim 7 \text{ W m}^{-2}$, for both model versions. Investigating additional causes of discrepancies between modelled QS and that measured by the EC is not directly related to the inclusion of moisture in CMB-RES and is reserved for future work.

There are no ablation measurements available for either of the two simulation periods. To examine the general behaviour of the CMB models, the 2008 simulation was repeated with debris thicknesses of 1–20 cm, holding the subdebris ice depth constant and scaling the minimum debris-water content as 3% of the reservoir capacity (consistent with the 23 cm simulation; Fig. 3.12). Total column melt is suppressed for all debris thicknesses compared with the clean-ice-melt rate, with less melt in CMB-RES than CMB-DRY due to heat extraction by QL and the reduced thermal diffusivity discussed in Sect. 3.3.2. Therefore, the CMB models do not reproduce the typical Østrem curve, wherein melt is enhanced below a critical debris thickness that ranges between 1.5 and 5 cm (e.g. Loomis, 1970; Fujii, 1977; Inoue and Yoshida, 1980; Mattson et al., 1993) and suppressed above this value. The rising limb of the Østrem curve is not reproduced for several reasons. First, in the clean-ice and thinly debris-covered simulations, lower night-time air temperatures in the beginning of the evaluation period (20–24 July 2008; cf. Fig. 3.4a) produce freezing events that cool the subsurface. Averaged over the entire evaluation period, a non-negligible amount of energy is expended to warm the ice column as a result. For example, in the clean-ice simulation, this heat flux amounts to 3.7 W m^{-2} . For CMB-RES (CMB-DRY) with debris thicknesses of 1 and 2 cm, the average energy required is 4.4 (5.3) and 3.1 (3.5) W m^{-2} , respectively. In addition, subzero englacial temperatures in the clean-ice simulation are eradicated more quickly, since penetrating shortwave radiation is considered. Finally, other processes that are not treated in the CMB models may be important to fully reproduce the rising limb of the Østrem curve, such as (1) changes in the surface albedo as the debris cover becomes more continuous, as in the albedo “patchiness” scheme introduced by Reid

and Brock (2010), and (2) wind-driven evaporation inside the debris layer (Evatt et al., working paper, 2014).

3.5 Conclusion

In this paper, we introduce a new model for the surface energy balance and CMB of debris-covered glaciers that includes surface vapour fluxes and a reservoir parameterization for moisture infiltration and phase changes. Although the parameterization is a simplification of the complex moist physics of debris, our model is a novel attempt to treat moisture within glacier debris cover, and one that permits two important advances: (1) it incorporates the effects of ice and water on the physical and thermal properties of the debris and therefore on ice ablation, and (2) it includes an estimate of the moisture exchanges between the surface and the atmosphere.

The inclusion of the water vapour flux opens up avenues of future research. For example, distributed simulations are required to more rigorously investigate relevant scientific questions about debris-covered glaciers, such as projecting their behaviour and runoff under changing climate conditions. A key constraint in performing such simulations is obtaining forcing data, since the highly heterogeneous surface of debris-covered glaciers makes the spatial distribution of air temperature and winds uncertain. Current approaches, employing elevation-based extrapolation, appear to be inadequate (Reid et al., 2012). Interactive coupling with a high-resolution atmospheric model provides one solution; however, the conventional modelling approach would introduce errors due to the absence of moisture exchange between the surface and the atmosphere. In incorporating that flux, CMB-RES is a step toward more precisely computing glacier–atmosphere feedbacks within coupled surface-and-atmosphere modelling schemes and more accurately predicting alterations in freshwater budgets and other potential impacts of glacier change.

References

- Aubinet, M., Vesala, T., and Papale, D. (Eds.): Eddy Covariance: a Practical Guide to Measurement and Data Analysis, Springer, Dordrecht, Heidelberg, London, New York, 2012.
- Bhambri, R., Bolch, T., Chaujar, R. K., and Kulshreshtha, S. C.: Glacier changes in the Garhwal Himalaya, India, from 1968 to 2006 based on remote sensing, *J. Glaciol.*, 57, 543–556, 2011.
- Bolch, T., Buchroithner, M., Pieczonka, T., and Kunert, A.: Planimetric and volumetric glacier changes in the Khumbu Himal, Nepal, since 1962 using Corona, Landsat TM and ASTER data, *J. Glaciol.*, 54, 592–600, 2008.
- Braithwaite, R. J.: Aerodynamic stability and turbulent sensible-heat flux over a melting ice surface, the Greenland ice sheet, *J. Glaciol.*, 41, 562–571, 1995.
- Brock, B., Mihalcea, C., Citterio, M., D’Agata, C., Cutler, M., Diolaiuti, G., Kirkbride, M. P., Maconachie, H., and Smiraglia, C.: Spatial and temporal patterns of thermal resistance and heat conduction on debris-covered Miage Glacier, Italian Alps, *Geophysical Research Abstracts*, European Geosciences Union General Assembly, Vienna, Austria, 2–7 April 2006, Vol. 8, ISSN: 1029-7006, 2006.
- Brock, B. W., Mihalcea, C., Kirkbride, M. P., Diolaiuti, G., Cutler, M. E., and Smiraglia, C.: Meteorology and surface energy fluxes in the 2005–2007 ablation seasons at the Miage debris-covered glacier, Mont Blanc Massif, Italian Alps, *J. Geophys. Res.*, 115, D09106, doi:10.1029/2009JD013224, 2010.
- Collier, E., Mölg, T., Maussion, F., Scherer, D., Mayer, C., and Bush, A. B. G.: High-resolution

- interactive modelling of the mountain glacier–atmosphere interface: an application over the Karakoram, *The Cryosphere*, 7, 779–795, 2013.
- Conway, H. and Rasmussen, L. A.: Summer temperature profiles within supraglacial debris on Khumbu Glacier, Nepal, *Debris-Covered Glaciers*, IAHS PUBLICATION no. 264, 89–97, 2000.
- Dall’Amico, M., Endrizzi, S., Gruber, S., and Rigon, R.: A robust and energy-conserving model of freezing variably-saturated soil, *The Cryosphere*, 5, 469–484, 2011.
- Dee, D. P., Uppala, S. M., Simmons, A. J., Berrisford, P., Poli, P., Kobayashi, S., Andrae, U., Balmaseda, M. A., Balsamo, G., Bauer, P., Bechtold, P., Beljaars, A. C. M., van de Berg, L., Bidlot, J., Bormann, N., Delsol, C., Dragani, R., Fuentes, M., Geer, A. J., Haimberger, L., Healy, S. B., Hersbach, H., Hlm, E. V., Isaksen, L., Kållberg, P., Köhler, M., Matricardi, M., McNally, A. P., Monge-Sanz, B. M., Morcrette, J.-J., Park, B.-K., Peubey, C., de Rosnay, P., Tavolato, C., Thpaut, J.-N., and Vitart, F.: The ERA-Interim reanalysis: configuration and performance of the data assimilation system, *Q. J. Roy. Meteor. Soc.*, 137, 553–597, 2011.
- Edlefsen, N. E. and Anderson, A. B. C.: Thermodynamics of soil moisture, *Hilgardia*, 15, 31–298, 1943.
- Fujii, Y.: Experiment on glacier ablation under a layer of debris cover, *J. Japan. Soc. Snow Ice (Seppyō)*, 39, 20–21, 1977.
- Fyffe, C., Brock, B. W., Kirkbride, M. P., Mair, D. W. F., and Diotri, F.: The hydrology of a debris-covered glacier, the Miage Glacier, Italy, *BHS Eleventh National Symposium, Hydrology for a changing world*, Dundee, 9–11 July 2012, doi:10.7558/bhs.2012.ns19, 2012.
- Fyffe, C., Reid, T. D. Brock, B. W., Kirkbride, M. P., Diolaiuti, G., Smiraglia, C., and Diotri, F.: A distributed energy balance melt model of an alpine debris-covered glacier, *J. Glaciol.*, 60, 587–602, 2014.
- Han, H. D., Ding, Y. J., and Liu, S. Y.: A simple model to estimate ice ablation under a thick debris layer, *J. Glaciol.*, 52, 528–536, 2006.

- Inoue, J. and Yoshida, M.: Ablation and heat exchange over the Khumbu Glacier, *J. Japan. Soc. Snow Ice (Seppyo)*, 39, 7–14, 1980.
- Kääb, A., Berthier, E., Nuth, C., Gardelle, J., and Arnaud, Y.: Contrasting patterns of early twenty-first-century glacier mass change in the Himalayas, *Nature*, 488, 495–498, 2012.
- Karra, S. and Painter, S. L. and Lichtner, P. C.: Three-phase numerical model for subsurface hydrology in permafrost-affected regions, *The Cryosphere Discussions*, 8, 1935–1950, 2014.
- Kaser, G.: Measurement of evaporation from snow, *Arch. Met. Geoph. Biokl. Ser. B.*, 30, 333–340, 1982.
- Kayastha, R. B., Takeuchi, Y., Nakawo, M., and Ageta, Y.: Practical prediction of ice melting beneath various thickness of debris cover on Khumbu Glacier, Nepal using a positive degree-day factor, *Symposium at Seattle 2000 – Debris-Covered Glaciers*, *IAHS Publ.*, 264, 71–81, 2000.
- Kraus, H.: An energy-balance model for ablation in mountainous areas, *Snow and Ice-Symposium-Neiges et Glaces*, August 1971, *IAHS-AISH PUBLICATION* no. 104, 1975.
- Lejeune, Y., Bertrand, J.-M., Wagnon, P., and Morin, S.: A physically based model of the year-round surface energy and mass balance of debris-covered glaciers, *J. Glaciol.*, 59, 327–344, 2013.
- Lohman, S. W.: Ground-water hydraulics. U.S. Geological Survey Professional Paper 708, 1972.
- Loomis, S. R.: Morphology and ablation processes on glacier ice, *Assoc. Am. Geogr. Proc.*, 2, 88–92, 1970.
- MacDonell, S., Kinnard, C., Mölg, T., Nicholson, L., and Abermann, J.: Meteorological drivers of ablation processes on a cold glacier in the semi-arid Andes of Chile, *The Cryosphere*, 7, 1513–1526, 2013.
- Mattson, L. E., Gardner, J. S., and Young, G. J.: Ablation on debris covered glaciers: an example from the Rakhiot Glacier, Punjab, Himalaya, *Snow and Glacier Hydrology*, *IAHS-IASH Publ.*, 218, 289–296, 1993.

- Mölg, T., Cullen, N. J., Hardy, D. R., Kaser, G., and Klok, E. J.: Mass balance of a slope glacier on Kilimanjaro and its sensitivity to climate, *Int. J. Climatol.*, 28, 881–892, 2008.
- Mölg, T., Cullen, N. J., Hardy, D. R., Winkler, M., and Kaser, G.: Quantifying climate change in the tropical midtroposphere over East Africa from glacier shrinkage on Kilimanjaro, *J. Climate*, 22, 4162–4181, 2009.
- Mölg, T., Maussion, F., Yang, W., and Scherer, D.: The footprint of Asian monsoon dynamics in the mass and energy balance of a Tibetan glacier, *The Cryosphere*, 6, 1445–1461, 2012.
- Nakawo, M. and Young, G. J.: Field experiments to determine the effect of a debris layer on ablation of glacier ice, *Ann. Glaciol.*, 2, 85–91, 1981.
- Nakawo, M. and Young, G. J.: Estimate of glacier ablation under a debris layer from surface temperature and meteorological variables, *J. Glaciol.*, 28, 29–34, 1982.
- Nicholson, L. and Benn, D.: Calculating ice melt beneath a debris layer using meteorological data, *J. Glaciol.*, 52, 463–470, 2006.
- Nicholson, L. and Benn, D.: Properties of natural supraglacial debris in relation to modelling sub-debris ice ablation, *EPSL*, 38, 490–501, 2012.
- Nicholson, L., Prinz, R., Mölg, T., and Kaser, G.: Micrometeorological conditions and surface mass and energy fluxes on Lewis glacier, Mt Kenya, in relation to other tropical glaciers. *The Cryosphere*, 7, 1205–1225, 2013.
- Østrem, G.: Ice melting under a thin layer of moraine, and the existence of ice cores in moraine ridges, *Geogr. Ann.*, 41, 228–230, 1959.
- Reid, T. D. and Brock, B. W.: An energy-balance model for debris-covered glaciers including heat conduction through the debris layer, *J. Glaciol.*, 56, 903–916, 2010.
- Reid, T. D., Carenzo, M., Pellicciotti, F., and Brock, B. W.: Including debris cover effects in a distributed model of glacier ablation, *J. Geophys. Res.*, 117, D18105, doi:10.1029/2012JD017795, 2012.

- Reijmer, C. H. and Hock, R.: Internal accumulation on Storglaciaren, Sweden, in a multi-layer snow model coupled to a distributed energy- and mass- balance model, *J. Glaciol.*, 54, 61–71, 2008.
- Reznichenko, N., Davies, T., Shulmeister, J., and McSaveney, M.: Effects of debris on ice-surface melting rates: an experimental study, *J. Glaciol.*, 56, 384–394, 2010.
- Sakai, A., Fujita, K., and Kubota, J.: Evaporation and percolation effect on melting at debris-covered Lirung Glacier, Nepal Himalayas, 1996, *Bull. Glaciol. Res.*, 21, 9–15, 2004.
- Sheng, D.: Review of fundamental principles in modelling unsaturated soil behaviour, *Comput. Geotech.*, 38, 757–776, 2011.
- Smith, G. D.: Numerical solution of partial differential equations: finite difference methods, 3rd Edn., Oxford, Oxford University Press, 1985.
- Stokes, C. R., Popovnin, V., Aleynikov, A., Gurney, S. D., and Shahgedanova, M.: Recent glacier retreat in the Caucasus Mountains, Russia, and associated increase in supraglacial debris cover and supra-/proglacial lake development, *Ann. Glaciol.*, 46, 195–203, 2007.
- Webb, E. K., Pearman, G. I., and Leuning, R.: Correction of flux measurements for density effects due to heat and water vapour transfer, *Q. J. Roy. Meteor. Soc.*, 106, 85–100, 1980.
- Wilson, G. W., Fredlund, D. G., and Barbour, S.L.: Coupled soil-atmosphere modelling for soil evaporation, *Can. Geotech. J.*, 31, 151–161, 1994.
- Yeh, .H-F., Lee, C.-C., and Lee, C.-H.: A rainfall-infiltration model for unsaturated soil slope stability, *J. Environ. Eng. Manage.*, 18, 261–268, 2008.
- Zhang, Y., Fujita, K., Liu, S., Liu, Q., and Nuimura, T.: Distribution of debris thickness and its effect on ice melt at Hailuogou glacier, southeastern Tibetan Plateau, using in situ surveys and ASTER imagery, *J. Glaciol.*, 57, 1147–1157, 2011.
- Zeng, Y., Su, Z., Wan, L., and Wen, J.: A simulation analysis of the advective effect on evaporation using a two-phase heat and mass flow model, *Water Resour. Res.*, 47, W10529, doi:10.1029/2011WR010701, 2011.

Chapter 4

Impact of debris cover on glacier ablation and atmosphere-glacier feedbacks in the Karakoram

4.1 Introduction¹

The Karakoram region of the greater Himalaya ($\sim 74^{\circ} 77' \text{ E}$, $34^{\circ} 37' \text{ N}$; Fig. 4.1) is extensively glacierized, with an ice-covered area of $\sim 18\,000 \text{ km}^2$ (Bolch et al., 2012). Supraglacial debris is widespread, and covers an estimated $\sim 18\text{--}22\%$ of the glacierized area (Scherler et al., 2011a; Hewitt, 2011), which is approximately twice the Himalayan average of $\sim 10\%$ (Bolch et al., 2012). The region has received a great deal of public and scientific attention in recent years due to evidence of stable or even slightly positive mass balances in the 2000s (Hewitt, 2005; Scherler et al., 2011a; Gardelle et al., 2012, 2013; Käab et al., 2012) that are in contrast with predominantly negative balances of glaciers in the rest of the Hindu Kush-Himalaya (HKH; Cogley, 2011). Knowledge of the hydrological response of Karakoram glaciers to climate change is critical, since their meltwater contributes to freshwater resources in the highly populated region of South Asia (Kaser et al., 2010; Lutz et al., 2014). However, due to logistical constraints and political instability, field observations of glaciological and meteorological conditions in the

¹F. Maussion, L.I. Nicholson, W. Immerzeel, and A. B. G. Bush contributed to this chapter.

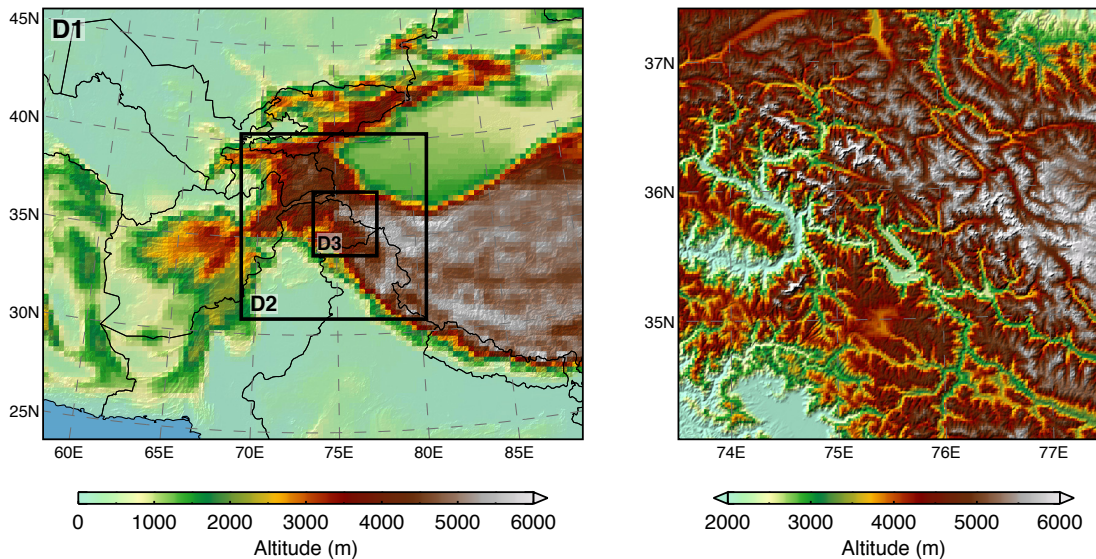


Figure 4.1: Topographic height shaded in units of m for **(a)** all three model domains in WRF-CMB, which are centered over the Karakoram and configured with grid spacings of 30-, 10- and 2-km resolution and grid dimensions of 84x105, 109x109 and 186x186, and **(b)** a zoom-in of the finest resolution domain, WRF D3.

Karakoram are sparse in space and time, in particular at high altitudes (Mihalcea et al., 2006, 2008; Mayer et al., 2014). Although observational records have been supplemented in recent decades by remote sensing data (e.g. Gardelle et al., 2012, 2013; Kääb et al., 2012), large gaps remain in our understanding of the important drivers of glacier change in this region, including regional atmospheric conditions, local topography and glacier debris cover, as well as interactions between them. Physically based numerical modelling has the potential to supplement observations and provide additional insight into contemporary glacier dynamics as well as to provide a methodology for predictions of future glacier response.

The prevalence of debris cover has a strong potential influence on glacier behaviour in the Karakoram, as field studies have shown that debris cover can significantly alter the ice ablation rate compared to that of clean ice (e.g. Østrem, 1959; Fujii, 1977; Inoue and Yoshida, 1980). Ice melt is enhanced beneath debris cover less than a few centimeters thick due to increased absorption of solar radiation. At greater thicknesses, ice ablation decreases exponentially with thickness due to insulation of the ice from atmospheric energy sources. The presence of debris also drastically alters glacier surface conditions, including the surface temperature, roughness

and saturation, with alterations to the surface energy fluxes (Inoue and Yoshida, 1980; Takeuchi et al., 2001; Brock et al., 2010) and the atmospheric boundary layer (Granger et al., 2002). Therefore, there is a strong potential for debris-covered ice to affect atmosphere-glacier feedbacks in this region.

Two main issues arise in attempting to include the influence of debris cover in simulations of Karakoram glaciers. First, the debris thickness, extent and thermal properties are largely unknown and their specification is highly uncertain. Second, the spatial distribution of meteorological conditions is uncertain due to the highly heterogeneous surface conditions in the ablation zone (e.g. Nicholson and Benn, 2012) and the complex topography, with current approaches using elevation-based extrapolation appearing to be inadequate (Reid et al., 2012). Here we investigate the influence of debris cover on Karakoram glacier surface-energy and mass exchanges and feedbacks with the atmosphere during an ablation season, using an interactively coupled atmosphere and glacier climatic mass balance (CMB) model that includes debris cover. By comparing a debris free simulation to a simulation where we include debris cover with an assumed idealized thickness, we first quantify differences in the surface energy balance and mass fluxes. We then assess (1) feedbacks between the atmosphere and glacier surfaces using the coupled model and (2) differences in boundary layer development and turbulent fluxes.

4.2 Methods

The modelling tool employed in this study is an interactively coupled, high-resolution, regional atmosphere and glacier climatic mass balance model that explicitly resolves the surface-energy and CMB processes of alpine glaciers at the regional scale (WRF-CMB; Collier et al., 2013). This model has been previously applied to the study region neglecting debris cover and was capable of reproducing the magnitudes of the few available observations of glacier CMB in this region. The changes introduced to the atmospheric and glacier CMB model components for this study are described in Sect. 4.2.1 and 4.2.2, respectively. Using WRF-CMB, we performed two simulations for the period of 1 April to 1 October 2004: the first treated all glacier surfaces as debris-free (**CLN**) and the second introduced an idealized debris thickness specification (**DEB**), which is described in Sect. 4.2.3. The first month of the simulation period was discarded as model

spin-up time, to address potential errors in the initial conditions, in particular the initial snow depth and density and subsurface temperatures. A brief evaluation of simulated land surface temperature (LST) is given in Sect. 4.2.4.

4.2.1 Regional atmospheric model

The atmospheric component of WRF-CMB is the Advanced Research version of the Weather Research and Forecasting (WRF) model version 3.6.1 (Skamarock and Klemp, 2008). WRF was configured with three nested domains, of 30–, 10–, and 2–km resolution, which were centered over the Karakoram region (Fig. 4.1). Yao (2007) estimated that the largest 15 glaciers in the Karakoram account for more than half of the ice-covered area, with nine glaciers exceeding 50 km in length (Copland et al., 2011), which makes the glaciers of this region optimal for representation in an atmospheric model at the finest grid spacing of 2 km. The domains had 40 vertical levels, with the lowest model level specified at a height of ~ 17 m.

The model physics and dynamics options were selected based on a previous application of WRF-CMB over this region (Collier et al., 2013, Table 4.1). However, in this study the land surface mode was updated to the Noah-MP scheme (Niu et al., 2011), which provides an improved treatment of snow physics in non-glacierized grid cells compared with the Noah scheme (Chen and Dudhia, 2001), by simulating the energy balance and skin temperature of the vegetation canopy and snowpack separately, introducing multiple layers in the snowpack, and providing an improved treatment of frozen soils. Note that the prognosis of surface and subsurface conditions for glacierized grid cells is performed by the CMB model, which is discussed in the next section. The adaptive time stepping scheme was used, which greatly increased the execution speed of the simulations. Horizontal diffusion was also changed to be computed in physical space rather than along model levels, since this option is recommended by WRF developers for applications in complex terrain where the terrain-following vertical levels are sloped. Finally, for the finest-resolution domain (hereafter WRF D3), slope effects on radiation and topographic shading were accounted for and a cumulus parameterization was neglected, since at this resolution the model is assumed to be convection permitting (e.g. Molinari and Dudek, 1992; Weisman et al., 1997).

The USGS land cover data used by WRF were updated to incorporate more recent glacier

Table 4.1: WRF configuration

Model configuration		
Horizontal grid spacing	30, 10, 2 km (domains 1–3)	
Min/max time step	30/200, 10/60, 2/13 s	
Vertical levels	40	
Model top pressure	50 hPa	
Model physics		
Radiation	CAM	Collins et al. (2004)
Microphysics	Thompson	Thompson et al. (2008)
Cumulus	Kain–Fritsch (none in D3)	Kain (2004)
Atmospheric boundary layer	Yonsei University	Hong et al. (2006)
Surface layer	Monin–Obukhov (revised MM5)	Jiménez et al. (2012)
Land surface	Noah–MP	Niu et al. (2011)
Dynamics		
Top boundary condition	Rayleigh damping	
Horizontal diffusion	Computed in physical space	
Lateral boundaries		
Forcing	ERA Interim, $0.75^\circ \times 0.75^\circ$ updated 6-hourly	Dee et al. (2011)

inventories for the region. Over the Himalayan region, we used the glacier outlines from the Randolph Glacier Inventory v3.2 (Pfeffer et al., 2014). For the Karakoram, we used the inventory of Rankl et al. (2014), which was obtained by updating the RGI manually on the basis of Landsat scenes. To determine which grid cells in each WRF domain were glacierized, the outlines were rasterized on a high-resolution (HR) grid with a resolution 50 times the original grid spacing of the domain. The fractional glacier coverage of pixels in each domain was calculated on the HR-grid, and a threshold of 40% coverage was used to classify a grid cell as glacier. The soil categories and vegetation parameters of these pixels were updated to be consistent with the glacier outlines, with glacierized pixels assigned as unvegetated “land-ice”.

The atmospheric model was forced at the boundaries of the coarse resolution domain with the ERA-Interim reanalysis from the European Centre for Medium-Range Weather Forecasts (ECMWF; Dee et al., 2011). The spatial and temporal resolution of the ERA-Interim data are $0.75^\circ \times 0.75^\circ$ and 6-hourly, respectively. Snow depths in ERA Interim over the Karakoram are unrealistic (more than 20 m; Collier et al., 2013). Therefore, an alternative initial snow

Table 4.2: Subsurface layer depths.

Snow	variable
Debris	every 0.01 m
Ice	0.1, 0.2, 0.3, 0.4, 0.5, 1.0, 1.5, 2.0, 2.5, 3.0, 3.5, 4.0, 5.0, 7.0 m

condition was estimated from the Global EASE-Grid 8-day blended SSM/I and MODIS snow cover dataset for snow water equivalent (Brodzik et al., 2007), by assuming a snow density of 300 kg m^{-3} and specifying a depth of 1 m for areas with missing data, such as over large glaciers.

4.2.2 Glacier CMB model with debris treatment

The original basis of the glacier CMB model is the physically based model of Mölg et al. (2008, 2009). The model solves the full energy balance equation to determine the energy available for snow and ice ablation. The computation of the total column mass balance accounts for surface and sub-surface melt, refreeze and changes in liquid water storage in the snowpack, surface vapor fluxes, and solid precipitation. The CMB model was adapted for interactive coupling with WRF by Collier et al. (2013) and modified to include glacier debris cover by Collier et al. (2014). For the version employed in this study, a time-varying snowpack is introduced on top of a static debris layer, both of which overlie a column of ice resolved down to a depth of 7.0 m. The vertical levels in the subsurface used for these simulations are presented in Table 4.2. Heat diffusion is explicitly modelled throughout the entire glacier column using a Crank-Nicolson approach.

Surface temperature is predicted using an iterative approach to determine the value that yields zero net flux in the surface energy balance equation. If the solution exceeds the melting point over snow or ice surfaces, it is reset to 273.15 K and the excess energy is used for melt. Initial test simulations with WRF-CMB over the Karakoram gave unrealistically cold surface temperatures as a result of excessive nighttime damping of the turbulent fluxes, in particular the sensible heat flux (QS). The stability corrections are based on the bulk Richardson number (Braithwaite, 1995)). In the most stable conditions, the corrections are equal to zero, which results in decoupling of the surface and the atmosphere and strong radiative cooling. However, even in less strongly stable conditions, the damping of modelled turbulent fluxes has been found

to be excessive in comparison with eddy covariance measurements over glaciers (Conway and Cullen, 2013). To prevent the stability corrections from being set to zero, we imposed a minimum windspeed of 1 m s^{-1} , consistent with previous modelling studies of glacier surface energy fluxes (Martin and Lejeune, 1998) and with the Noah-MP LSM (Niu et al., 2011). Furthermore, we limit the maximum amount of damping to 30 % (Martin and Lejeune, 1998; Giesen et al., 2009).

A full description of the debris treatment is described by Collier et al. (2014), however we provide a brief summary here. The debris layer is resolved into 1 cm layers and has an assumed porosity function that decreases linearly with depth. The properties of each layer in the debris are computed as weighted functions of whole-rock values and the contents of the pore space (air, water or ice) using values presented in Table 4.3. For the whole-rock values, the albedo was based on 50 spot measurements on a debris-covered glacier in Nepal (Nicholson and Benn, 2012); the density and thermal conductivity were selected as representative values spanning major rock types taken from Daly et al. (1966); Clark (1966), respectively; and, the specific heat capacity was taken from Conway and Rasmussen (2000). Moisture in the debris and its phase are modelled using a simple reservoir parameterization. When debris is exposed at the surface, the surface vapor pressure is parameterized as a simple linear function of the debris water and ice content.

To prevent errors arising from blended snow and debris layers (for example, constraints on the possible temperature values or excess melting), an adaptive vertical grid in the snowpack was introduced. For snow depths of up to one meter, the nearest integer number of 10 cm layers are assigned, while areas of the snowpack that exceed one meter are resolved into the nearest integer number of 50 cm layers. Snow depths between 1 and 10 cm are assigned a single computational layer, and depths less than 1 cm are not treated with a unique layer. Over regions of the snowpack where the layer depths have changed, linear interpolation is performed every timestep to calculate temperature changes, using the layer depths normalized by the total depth of the vertical grid that has changed. This procedure means that the bulk heat content of the snow pack is conserved, with the exception of when the snow depth crosses the minimum threshold depth of 1 cm. In the DEB simulation, changes in the bulk heat content of the snowpack in WRF D3 per timestep were small (less than 0.01 K). The CMB model is not designed for detailed

Table 4.3: Physical properties in the CMB model.

Density (kg m^{-3})		
ice	915	–
whole rock	2700	Daly et al. (1966)
water	1000	–
Specific heat capacity ($\text{J kg}^{-1} \text{K}^{-1}$)		
air	1005	–
ice	2106	–
whole rock	750	Clark (1966)
water	4181	–
Thermal conductivity ($\text{W m}^{-1} \text{K}^{-1}$)		
air	0.024	–
ice	2.51	–
whole rock	2.50	Conway and Rasmussen (2000)
water	0.58	–
Surface roughness length (m^{-1})		
ice	0.001	Reid and Brock (2010)
debris	0.016	Brock et al. (2010)
Albedo		
ice	0.30	Collier et al. (2013)
firn	0.55	Collier et al. (2013)
fresh snow	0.85	Collier et al. (2013)
debris	0.20	Nicholson and Benn (2012)
Emissivity		
ice/snow	0.97	Brock et al. (2010)
debris	0.94	Brock et al. (2010)

snowpack studies and therefore only prognoses a bulk snow density. Since the total snow depth is not modified by the interpolation scheme, snow mass is conserved.

The debris-free version of the CMB model normally has levels located at fixed depths in the subsurface, with the thermal and physical properties of each layer computed from a weighted average of the snow and ice content. However, to isolate the influence of debris on glacier energy and mass fluxes, the CLN simulation also employs the adaptive vertical grid in the snowpack in this study, with similar changes to the bulk heat content as reported for DEB. A test simulation from 1 April to 18 May 2004 was performed to compare the adaptive grid with the conventional CMB approach, with reasonable agreement in simulated snow depth ($R^2=0.99$; mean deviation MD = -1.9 cm; mean absolute deviation MAD = 5.4 cm), snow melt ($R^2=0.87$; MD = 6.8×10^{-4} kg m $^{-2}$; MAD = 1.2×10^{-3} kg m $^{-2}$), and surface temperature ($R^2=0.94$; MD = 0.6 K; MAD = 1.9 K).

The CMB model is a key component of this study, since it not only provides a treatment of debris cover but also permits snow-free conditions on glaciers, whereas the Noah-MP LSM imposes a minimum snow depth of 0.1 m w.e.. For these simulations, the CMB component treats glacier surfaces as debris free in WRF D1 and D2, while debris cover is introduced in the finest-resolution domain only, since D3 provides the best representation of both the complex topography and glacier extents.

4.2.3 Specification of debris extent and thickness in WRF D3

The RGI and the inventory of Rankl et al. (2014) provide glacier outlines that include debris-covered glacier areas when detected, but they do not delineate these areas. To define debris-covered areas in WRF D3, the clean ice/firn/snow mask of Kääb et al. (2012) was rasterized on the same HR (40-m) grid used to compute glacierized grid cells (cf. Sect. 4.2.1) For each WRF pixel, the percent coverage of debris was determined on the HR grid and the same threshold of 40 % was used to classify a glacier pixel as debris-covered. Figure 4.2a provides an example of the delineation for the Baltoro glacier $76^\circ 26' E$, $35^\circ 45' N$). We note that any debris-covered glacier areas that are not detected during the generation of the glacier outlines are missed.

Specifying the debris thickness was more complex, since this field varies strongly over small

spatial scales. For example, Nicholson and Benn (2012) reported very heterogeneous debris thickness varying between 0.5 and 2.0 m over distances of less than 100 m on the Ngozumpa glacier, Nepal. Spatial variability arises from many factors, including hillslope fluxes to the glacier; surface and subsurface transport; and, the presence of ice cliffs, melt ponds and crevasses (e.g. Brock et al., 2010; Zhang et al., 2011). The few available field measurements do not support a relationship between debris thickness and elevation (e.g. Mihalcea et al., 2006; Reid et al., 2012). However, measurements on the Tibetan plateau (Zhang et al., 2011), in Nepal (Nicholson and Benn, 2012), and in the Karakoram (Mihalcea et al., 2008) indicate that thicker values are more prevalent near glacier termini while thinner ones are more ubiquitous up-glacier.

Thus, in this study we adopt an idealized approach informed by the observed relationship to specify debris thickness over the areas identified as debris-covered in WRF D3, whereby the specified debris thickness increases along glacier centerlines, which were provided by Rankl et al. (2014). Moving down from the top of each glacier along its centerline, the distance down-glacier from the first debris-covered pixel was computed and a gradient of 1.0 cm of debris per 2-km grid cell was applied to obtain an average thickness for each grid cell of WRF D3. If a WRF grid cell contained more than one centerline, the highest thickness was taken. The value of the assumed gradient was selected to provide debris thicknesses of up to 40 cm at the termini of the longest glaciers in the Karakoram, such as the Baltoro glacier which has a length of ~ 60 km, in keeping with available field measurements on this glacier (Mihalcea et al., 2008). In addition, a minimum thickness of 2 cm was imposed over debris-covered pixels. Spatial maps of the result of the calculation are shown for the Baltoro glacier in Fig. 4.2b and for the entire WRF D3 in Fig. 4.2d, while the elevational distribution of debris and its thickness is shown in Fig. 4.2c. Where centerline information was unavailable (the region outside of the red contour in Fig. 4.2d), a constant thickness of 10 cm was assigned to each debris-covered pixel. For clarity, these data are not included in Fig. 4.2c.

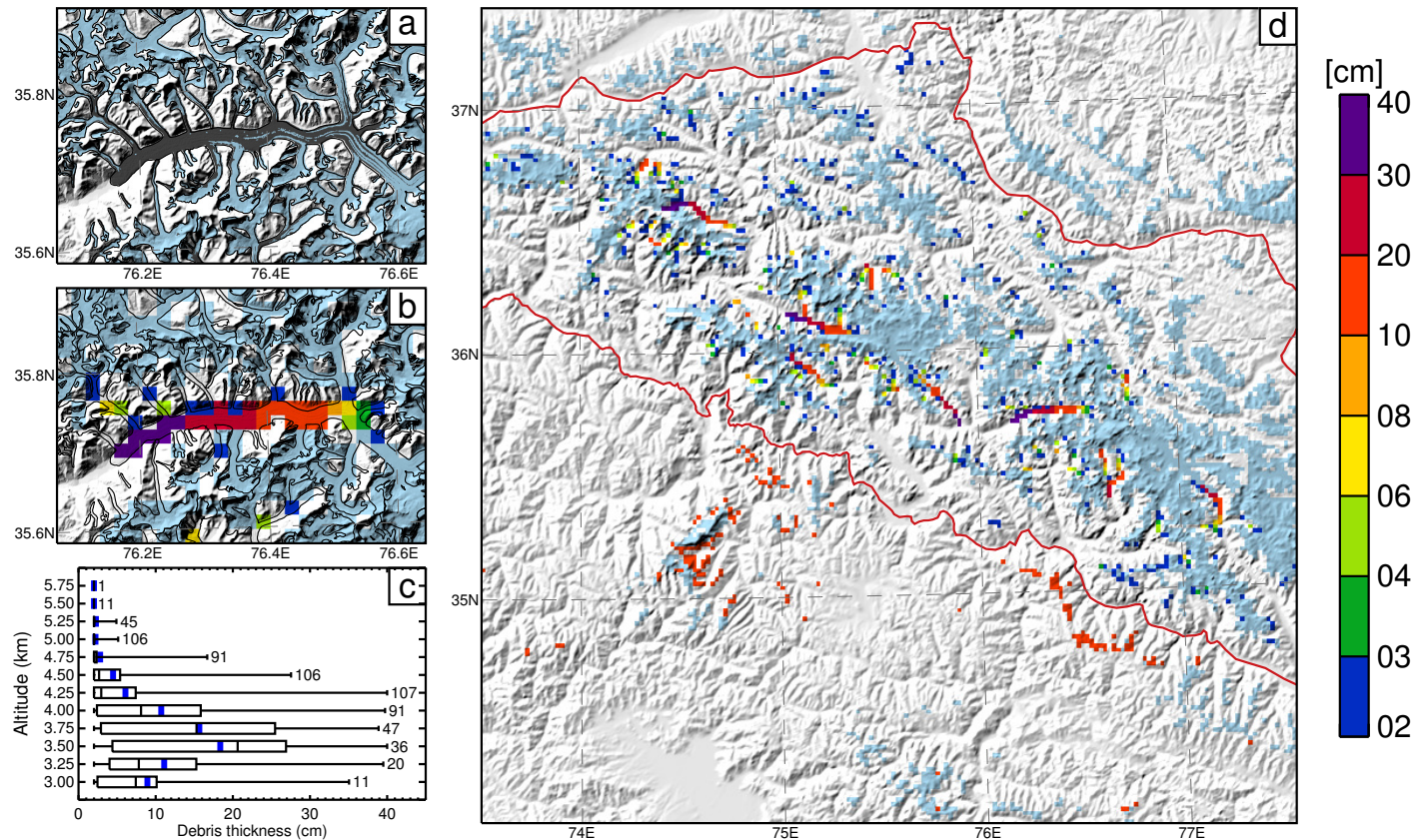


Figure 4.2: **(a)** debris-covered (grey) and debris-free (blue) glacier area, as calculated on the HR (40-m) grid for the Baltoro glacier and surrounding areas. The result of the debris thickness specification for **(b)** the Baltoro glacier and **(d)** the entire WRF-D3 region. In (d), the red line delineates the region where centerline information was available from (Rankl et al., 2014). **(c)** A box plot of debris thicknesses values for 250-m elevation bins in WRF D3. The thick-blue and thin-black lines indicate the mean and median thickness value in each bin and the total number of debris-covered pixels is given as a text string at the upper end of the range.

Although measurements indicate that debris thicknesses at the termini of Karakoram glaciers can exceed one meter (e.g. Mihalcea et al., 2008), it is well established that ablation decreases exponentially with debris thickness (e.g. Østrem, 1959; Loomis, 1970; Mattson et al., 1993). As the debris layer is resolved into 1–cm layers, including thickness values of up to 1 m would therefore greatly increase the computational expense of the CMB model with only a small change to the amount of sub-debris ice melt. In addition, features such as meltwater ponds and ice cliffs in the ablation zone absorb significantly more energy than adjacent debris-covered surfaces. These features may give compensatory high-melt rates (e.g. Inoue and Yoshida, 1980; Sakai et al., 1998, 2000; Pellicciotti et al., 2014; Immerzeel et al., 2014) that support using a thinner average or effective debris thickness when assigning an average value to each 2-km grid cell in WRF-D3.

Following the glacier outline update described in Sect. 4.2.1 and the approach for specifying debris thickness, WRF D3 contains a total of 5273 glacierized grid cells and 821 debris-covered glacier cells, giving a proportion of debris-covered glacier area in WRF D3 of $\sim 16\%$.

4.2.4 Evaluation of simulated land surface temperature

For model evaluation, we compared simulated LST over glacierized grid cells with daily daytime LST from the MODIS Terra MOD11A1 and Aqua MYD11A1 datasets, which are provided at a spatial resolution of 1 km. Only MODIS data with the highest quality flag were used for comparison and WRF-CMB data were taken from the closest available time step in local solar time. We focus our comparison on daytime values, to show the largest differences between CLN and DEB and because this field had the highest number of valid pixels at lower elevations between 1 May and 1 Oct 2004.

Figure 4.3a shows mean elevational profiles of LST over glacierized pixels for composite MODIS data and for the CLN and DEB simulations. Although the modelled profiles are significantly colder than the MODIS data, the simulated profile in DEB is in much closer agreement than CLN, as LST exceeds the melting point below the simulated mean snow line at ~ 4500 m a.s.l.. A spatial examination of MODIS LST suggests that these data may contain a warm bias as a result of blending of different glacier surface types as well as glacierized and

non-glacierized areas on the 1 km resolution grid. Figure 4.3b shows an example of MODIS Terra LST on 5 August 2004 around the Baltoro glacier, a time slice that was selected for the low number of missing values in this region. MODIS exceeds the melting point over most of the glacier, including over smaller, largely debris-free tributary glaciers, due to blending with valley rock walls. The data are also warmer over glacier areas with debris-covered fractions that fall below the threshold of 40 % used to define a WRF pixel as a debris-covered (cf. Fig. 4.2b). Therefore, the binary definition of debris-free and debris-covered glacier surface types likely contributes to a cold bias in WRF-CMB.

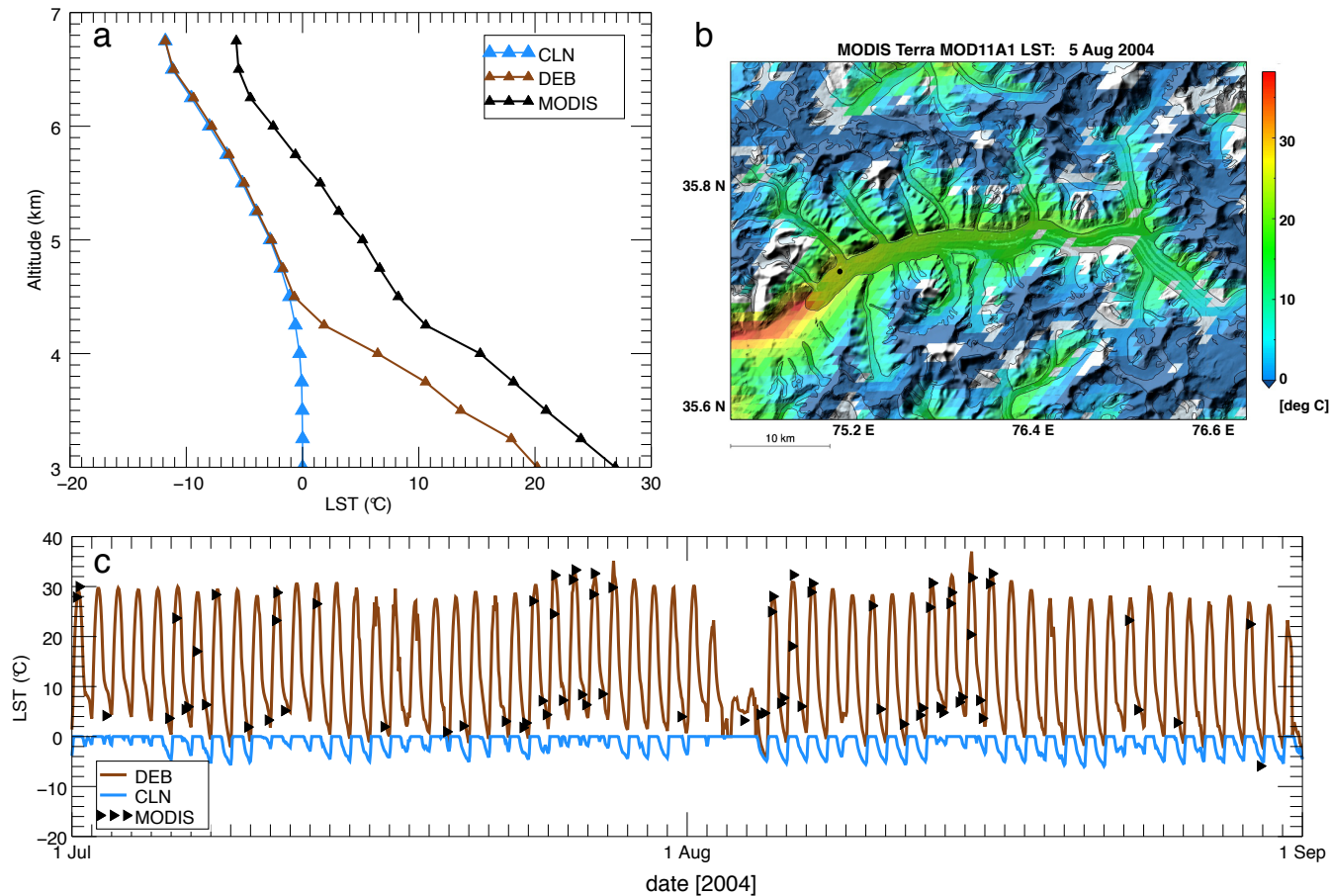


Figure 4.3: **(a)** Mean elevational profiles of land surface temperature from DEB, CLN, and composite MODIS Terra MOD11A1/Aqua MYD11A1 datasets, averaged from 1 May to 1 October 2004 and in 250-m elevation bins over glacierized pixels in WRF. MODIS data with the highest quality flag are projected on to the WRF D3 grid prior to averaging and compared with WRF data points from the same [local solar] time step. **(b)** A sample time slice of MODIS Terra LST from 5 August 2004 on its native grid, overlaid on the Baltoro glacier outline and debris-covered area. **(c)** Time series of LST from 1 July to 31 August 2004 from the same datasets in panel (a), taken from the pixel on the Baltoro tongue denoted by a black circle in panel (b).

To examine temporal variations, Fig. 4.3c shows a time series of LST for July and August 2004 from all three datasets at a pixel on the Baltoro glacier tongue denoted by a black circle on Fig. 4.3b, selected for the high temporal availability of MODIS data. Simulated surface temperature in DEB shows close agreement with MODIS, with daytime maxima exceeding 30°C and nighttime values frequently around or above the melting point, while CLN fails to capture LST variability in the ablation zone. However, comparison of earlier time slices indicates that simulated snow cover removal at this pixel occurs approximately one month later than in MODIS (not shown). Furthermore, a time series at a high-altitude snow-covered pixel at the top of the Baltoro South branch indicates that modelled daily minimum temperatures are too low in both simulations, despite the steps outlined in Sect. 4.2.2. Both of these features contribute to the overall cold bias in Fig. 4.3a.

4.3 Results

4.3.1 Meteorological drivers of glacier fluctuations

A time series of meteorological fields, area-averaged over glacier grid cells in WRF D3 in the DEB simulation, is presented as the black curve in Fig. 4.4. Variability over the simulation period is driven by the occurrence of precipitation events, which are associated with decreases in mean air temperature, incoming shortwave radiation, and surface pressure, and with increases in incoming longwave radiation and wind speeds. Strong precipitation events during which daily total precipitation exceeds 5 mm are most frequent in spring, in agreement with the findings of Maussion et al. (2014) of significant spring accumulation in this region.

The mean synoptic-scale flow over the simulation period is zonal in the vicinity of the Karakoram (Fig. 4.5a). Averaging over days where total precipitation exceeds 5 mm in WRF D3 indicates that such events coincide with the passage of low pressure systems, which result in a strengthening of the meridional geopotential gradient and stronger, more southwesterly flow aloft into D3 (Fig. 4.5b). A similar pattern is present in the lower level (lowest 500-hPa) circulation in the Karakoram, with a mean zonal flow (not shown) and a southwesterly component during hours with precipitation events exceeding 0.5 mm (Fig. 4.5c) that is closer to perpendic-

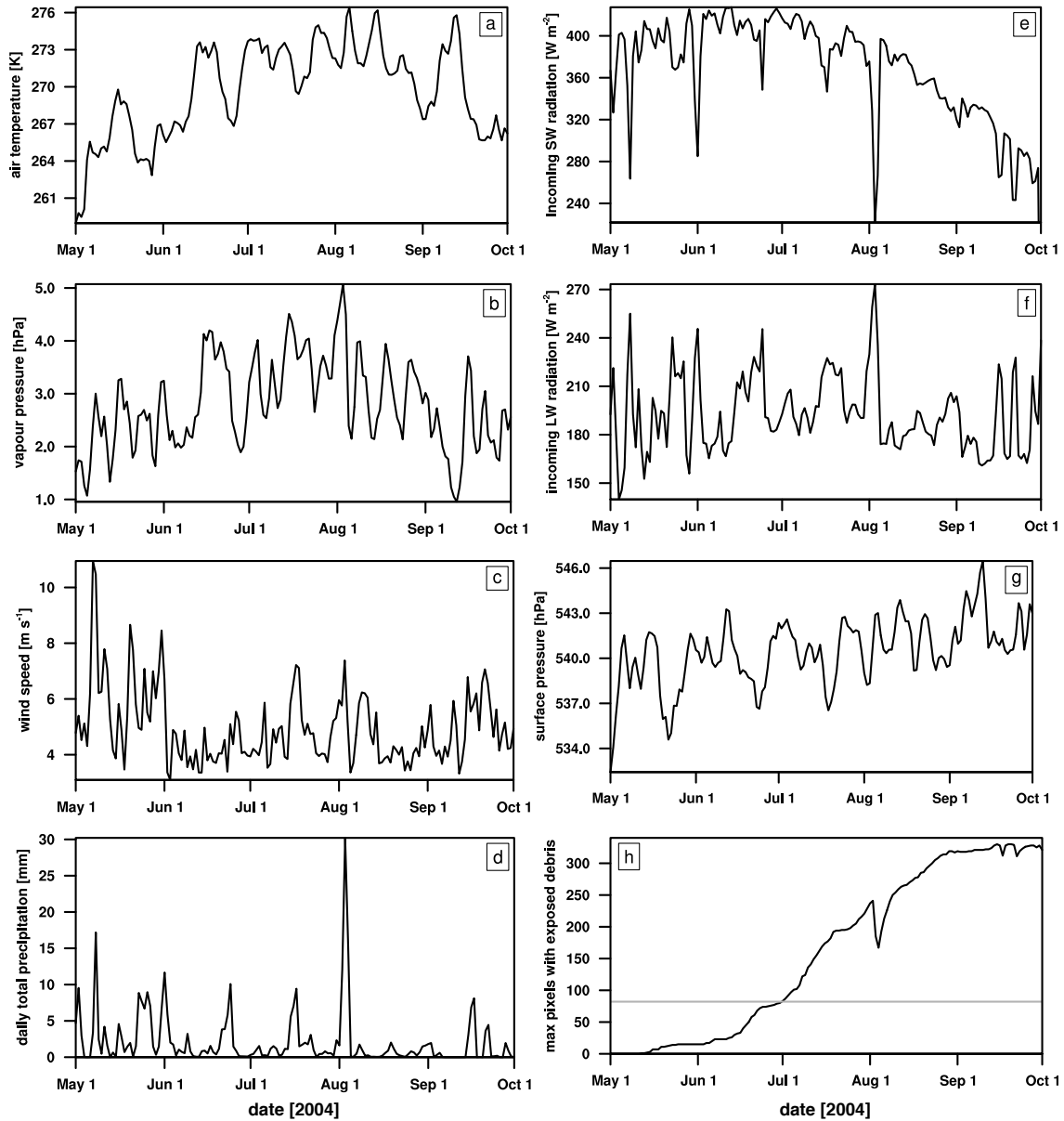


Figure 4.4: Time series of daily-mean meteorological data in the DEB simulation, area-averaged over glacierized grid cells: **(a)** air temperature [K], **(b)** vapour pressure [hPa], **(c)** wind speed [m s^{-1}], incoming **(e)** short- and **(f)** long-wave radiation [W m^{-2}], and **(g)** pressure [hPa]. Data were taken from the lowest model level, which was specified at a height of ~ 17 m. Panel **(d)** shows daily total precipitation in [mm]. Panel **(h)** shows the daily maximum number of exposed debris pixels in DEB, with the grey reference line on the y-axis indicating the 10% threshold for temporal averaging of subsequent results.

ular with the topographic arc and contributes to enhanced orographic precipitation. Consistent with this circulation pattern, total accumulation in WRF D3 is greatest in the western and southern parts of the domain and at higher elevations. Our results suggest, contrary to other studies [e.g.] (Mayer et al., 2014), that for this particular year summer precipitation is not the result from monsoon incursions but originates from the westerly circulation.

Area-averaged differences between meteorological forcing fields in DEB and CLN over the simulation are small, since more than 50% of the debris pixels remain snow covered over the simulation period (Fig. 4.4h). To elucidate the influence of debris cover on glaciological and meteorological dynamics, temporal averages presented in the remainder of Sect. 4.3 are performed for the period of 1 July to 1 October, when more than 10% of the total debris pixels are exposed. In addition, we focus on elevational profiles of relevant results, averaged from 3000 to 7500 m a.s.l. in 250-m bins that include a maximum of ~ 1200 (~ 200) clean-glacier (debris-covered) pixels (Fig. 4.6a).

4.3.2 Glacier surface energy and climatic mass dynamics

The introduction of debris cover has only a small impact on mean surface-energy fluxes from 1 July to 1 October 2004 (Table 4.4) due to overlying snow cover. However, elevational profiles of surface-energy fluxes reveal a strong influence of debris in lower ablation areas (Fig. 4.6b). Net shortwave radiation (SWnet) increases due to the lower surface albedo, while net longwave radiation (LWnet) becomes more negative due to stronger emission from warmer surface temperatures. The latent heat flux (QL) becomes a larger energy sink, reaching -20.0 W m^{-2} on average in the lowest elevational bands compared with only $2\text{--}8 \text{ W m}^{-2}$ in CLN. Both the turbulent flux of sensible heat (QS) and the conductive heat flux (QC) transition from small energy gains in CLN to strong energy sinks in DEB, as heat is transferred on average from the debris surface to the subsurface and to the atmosphere, with the latter flux extracting as much energy from the surface as LWnet at the lowest glacierized elevations. Penetrating shortwave radiation (QPS) becomes negligible as the overlying snow cover goes to zero. Above the mean elevation of the snow line at $\sim 4500 \text{ m a.s.l.}$, surface-energy fluxes in the two simulations are indistinguishable.

Snow and ice melt at lower elevations is the most strongly affected mass flux, with the

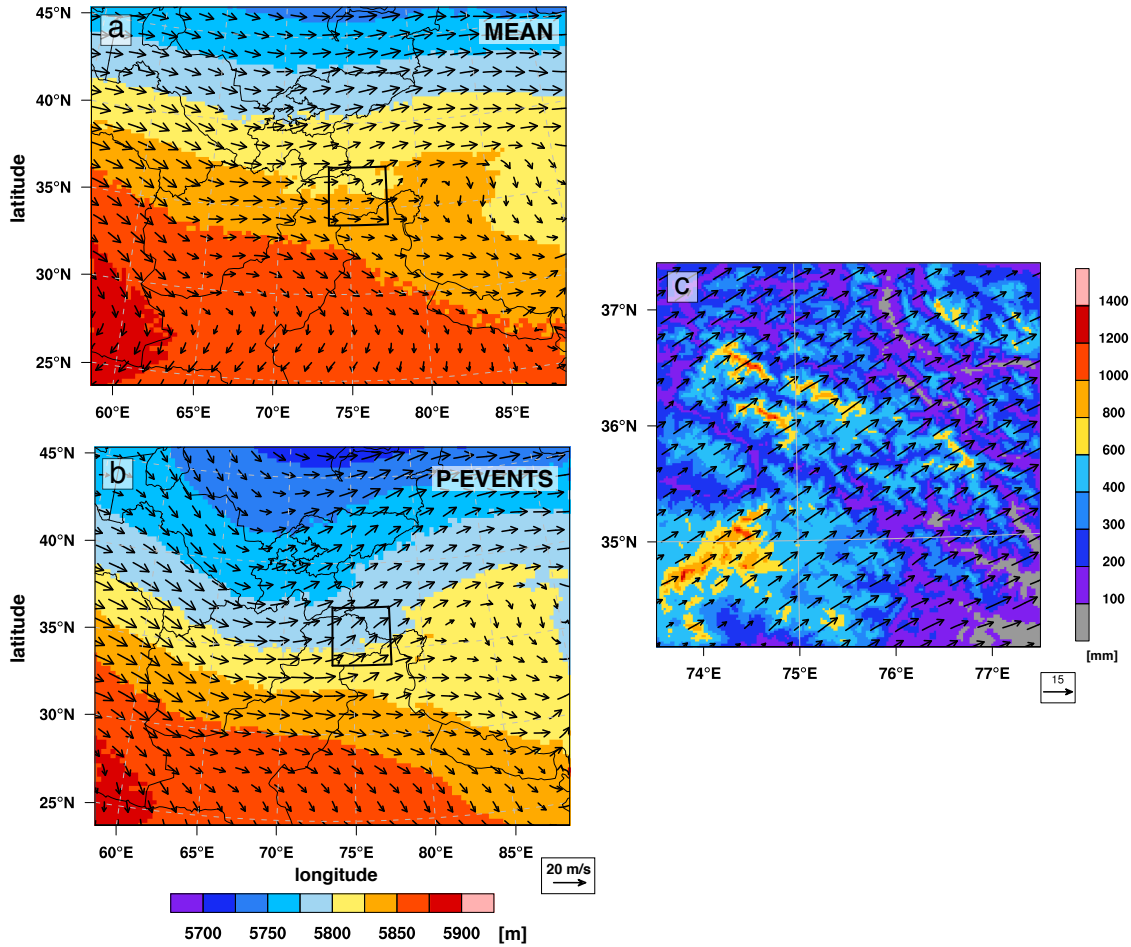


Figure 4.5: Geopotential height contours shaded in units of [m] and wind vectors at 500 hPa in WRF D1 averaged over (a) the whole simulation period of 1 May to 1 October 2004, and over (b) days with total precipitation exceeding 5 mm. The extent of WRF D3 is delineated by the black box. (c) Total accumulated precipitation in WRF D3 over the simulation, overlaid by wind vectors averaged over the lowest 500 hPa above the surface and over hours with basin-mean precipitation exceeding 0.25 mm.

Table 4.4: Mean glacier surface-energy and climatic-mass fluxes.

Surface energy fluxes (W m^{-2})	DEB	CLN
net shortwave (SWnet)	89.5	88.2
net longwave (LWnet)	-75.9	-74.6
sensible heat (QS)	8.2	10.7
latent heat (QL)	-6.2	-5.8
conduction (QC)	10.9	14.8
penetrating SW (QPS)	-11.1	-12.5
precipitation (QPRC)	~ 0	~ 0
Mass fluxes (kg m^{-2})	DEB	CLN
snow & ice melt	-0.22	-0.26
snowmelt refreeze	0.12	0.12
sublimation	-0.01	-0.01
deposition	~ 0	~ 0
evaporation	~ 0	-
condensation	~ 0	-
surface accumulation	0.03	0.03

total below 5000 m decreasing from 11.4 kg m^{-1} in CLN to 7.6 in DEB (Table 4.4; Fig. 4.6c). The difference largely reflects a strong decrease in surface melt, from 10.1 to 2.9 kg m^{-1} in DEB. Surface vapour fluxes are small when spatially and temporally averaged; however, they represent a non-negligible mass flux in total, with $\sim 2.0 \times 10^5 \text{ kg}$ of sublimation and $5.2 \times 10^4 \text{ kg}$ of deposition at snow and ice surfaces. Vapour fluxes between the debris and the atmosphere contribute an additional net loss of $1.4 \times 10^4 \text{ kg}$ over the simulation period.

Simulated daily mean ice ablation (corresponding to sub-debris or surface values in DEB and CLN, respectively, for the same snow-free pixels) shows a general decrease with both topographic height and debris thickness increase. Although melt rates below 3500 m have been estimated to be small as a result of insulation by thick debris cover (Hewitt 2005), our results indicate that appreciable values of $\sim 10 \text{ mm w.e. d}^{-1}$ occur under the thickest layers at lower elevations. The CMB model in DEB does not reproduce enhanced ablation under thinner debris layers, consistent with its behaviour in a previous application (Collier et al., 2014) and because these layers tend to be located at colder, higher elevations where melt energy is low and the debris is snow-covered (not shown). Nonetheless, the values fall in the range of the few available field measurements of glacier ablation in this region: Mayer et al. (2010) report rates from 110 to

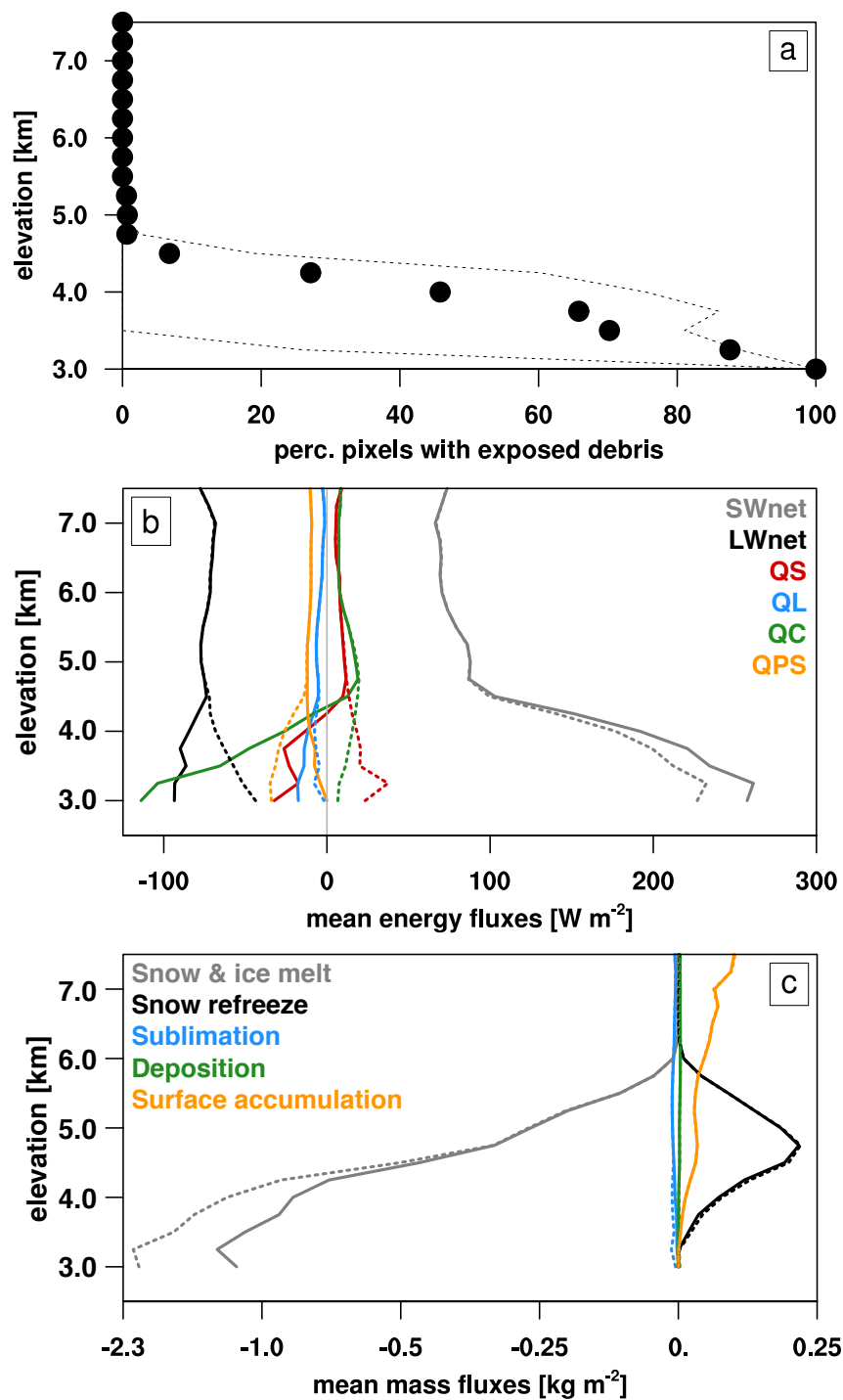


Figure 4.6: (a) The mean percentage of pixels containing in each 250-m elevation bin between 3000 and 7500 m a.s.l., with min and max values delineated by the dashed lines. Elevational profiles of mean glacier (b) surface-energy and (c) mass fluxes., with the solid (dashed) line denoting data from DEB (CLN). Note the non-linear x axis in panel (c).

23 mm w.e. d⁻¹ under debris covers of ~ 1 to 38 cm on the Hinarche glacier (74° 43' E, 36° 5' N) in 2008, while Mihalcea et al. (2006) reported rates of 10–60 mm w.e. d⁻¹ on the Baltoro glacier in 2004 over elevations of ~ 4000 –4700 m and thicknesses of 0 to 18 cm.

The mean vertical balance profile indicates the equilibrium line altitude (ELA) between 1 July and 1 October 2004 is located at approximately ~ 5250 m a.s.l. (Fig. 4.7b). Previously reported estimates of annual ELAs in the Karakoram range between 4200–4800 m (Young and Hewitt 1993), which is lower than our simulated value due to the focus on the ablation season and to the absence of avalanche accumulation, which is regionally important and produces ELAs that are often located hundreds of meters below the climatic snowline (e.g. Benn and Lehmkuhl, 2000; Hewitt, 2005, 2011). Summed below the simulated summertime ELA, there is a strong reduction in ablation in DEB compared with CLN, of $\sim 38\%$ or 10.8 m w.e..

A spatial plot of the total accumulated mass balance in DEB delineates regions of glacier mass gain and loss (Fig. 4.8a). Accumulation is higher in the western part of the domain, where more precipitation falls over the simulation period (cf. Fig. 4.5). Differences between DEB and CLN are small over most of the basin, with the exception of lower altitude glacier tongues where differences exceed of 3 m w.e. (Fig. 4.8b). The strong decrease in mass loss in these areas changes the basin-mean final mass balance from -221.4 kg m^{-2} in CLN to -146.5 in DEB.

4.3.3 Atmosphere-glacier feedbacks

The onset of surface melt occurs at a similar time in the DEB and CLN simulations, ranging from shortly after May 1 below 4000 m to late June above 5500 m (Fig. 4.9a). The simulated timing at higher altitudes is consistent with snow-pit observations between 5250 and 5400 m that were taken during the 2006 ablation season in the central Karakoram and which showed the onset of melt after mid-June (Mayer et al., 2014). The total number of hours for which surface temperature reaches or exceeds the melting point (here denoted as melt hours) ranges from more than 3000 at low-altitude glacier termini to less than 50 above 6000 m, with no melt occurring above ~ 7000 m (Fig. 4.9b). Heat transfer and storage by the debris layer results in upwards of 800 additional melt hours compared with CLN (Fig. 4.9c). These additional melt hours provide a strong heat flux to the atmosphere as demonstrated by the elevational profile

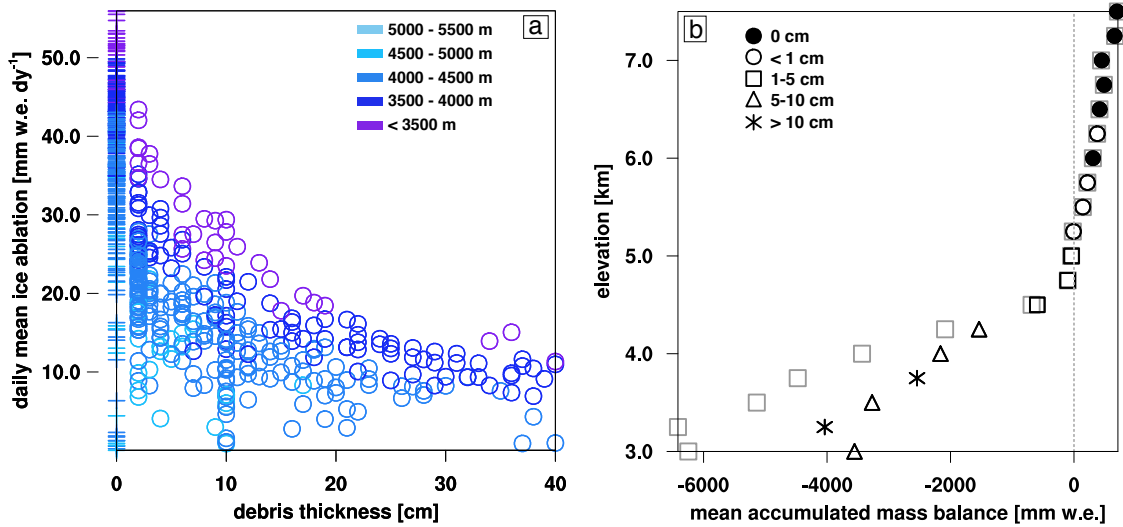


Figure 4.7: **(a)** Daily mean ice melt rate versus debris thickness for DEB (circle markers) and CLN (line markers), colored by their topographic height values. DEB values represent sub-debris ice ablation, while CLN values represent surface melt, considering only snow-free pixels (333 in total). **(b)** Vertical balance profile, averaged over all glacier pixels and in 250-m elevation bins. Grey-square markers denote results from the CLN simulation, while those from DEB are plotted with black markers, with the marker shape determined by the mean debris thickness.

of QS in Fig. 4.6a.

In total, the change in surface boundary conditions between DEB and CLN provides an additional 3.6×10^7 W of energy to the atmosphere. The result is much higher near-surface air temperatures over exposed debris, of up to 2–4 K at the lowest glacier termini (Fig. 4.10a), consistent with observations of warmer air temperatures over debris-covered glacier areas during the ablation season (Takeuchi et al., 2000, 2001; Reid et al., 2012). Despite the increase in temperature, 2-m relative humidity below the snow line is much higher in DEB than in CLN, as a result of the additional moisture flux (evaporation) provided by the more negative QL (Fig. 4.10b). Higher surface roughness values over debris result in a small decrease of near-surface horizontal wind speeds (Fig. 4.10c). Total accumulated precipitation is similar between the two simulations and ranges from 200–300 mm below 5000 m and increasing linearly with elevation above this level. These values are consistent with the few available records of annual precipitation, which indicate values of 150–200 mm in the semi-arid valleys and more than 1–2 m in the accumulation zones (Winiger et al., 2005; Hewitt, 2005). The simulated frozen fraction of precipitation increases approximately linearly from 10% at 3000 m to more than

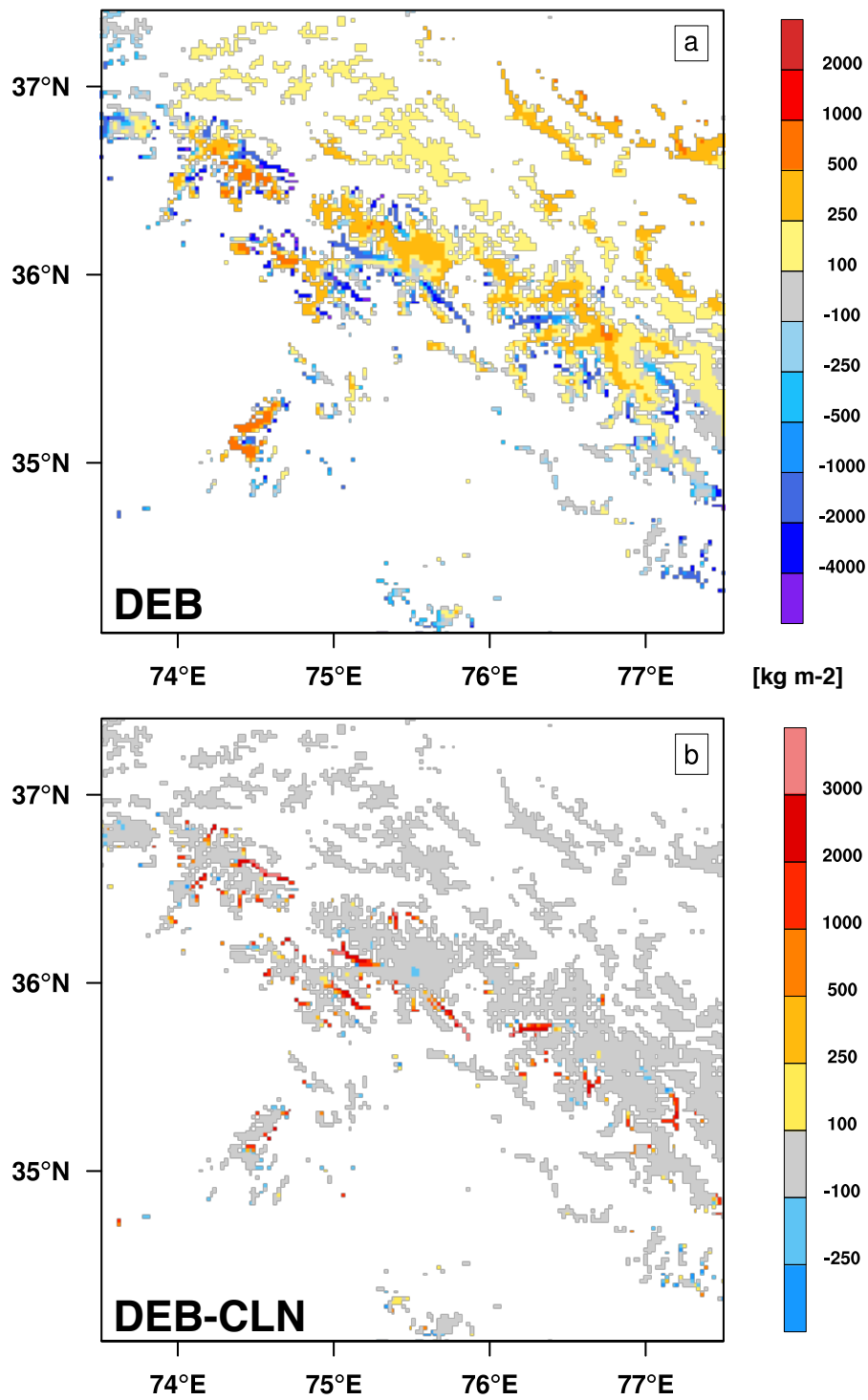


Figure 4.8: Total accumulated mass balance in $[\text{kg m}^{-2}]$ between 1 July–1 October 2004 for (a) the DEB simulation and (b) the difference between DEB and CLN.

Table 4.5: Elevational lapse rates.

	Below 4500 m		
	DEB	CLN	4500–7500 m BOTH
2-m air temperature [K m^{-1}]	-0.0087	-0.0061	-0.0073
2-m relative humidity [$\% \text{ m}^{-1}$]	-0.012	0.011	0.0051
10-m wind speed [$\text{m s}^{-1} \text{ m}^{-1}$]	0.0008	0.0005	0.0016
Accumulated precipitation [mm]	0.069	0.063	0.15 (5000–7000 m)
Frozen fraction [$\% \text{ m}^{-1}$]	0.043	0.043	–

90 % at ~ 5250 m, after which point the fraction remains approximately constant with increasing elevation, again consistent with reported observations for the Karakoram (Winiger et al., 2005). Mean elevational lapse rates in near-surface meteorological fields are provided in Table 4.5 where the variation is approximately linear. Elevations above 7000 m are excluded due to the small number of glacier pixels present in these bins (cf. Fig. 4.6a).

The atmospheric surface layer becomes less stable in DEB due to strong solar heating of exposed debris, which results in stronger turbulent mixing and convective overturning. As a result, the mean planetary boundary layer (PBL) height exceeds 2 km during the day compared with only a few hundred meters in CLN (Fig. 4.11a). The development of a convective mixed layer also starts approximately three hours earlier on average over exposed debris, shortly after 7 am compared with 10 am over glacier ice. The influence of debris on the atmosphere is greatest over thicker covers at lower altitudes, and thus the elevational gradient in mean PBL height below 4500 m is reversed in DEB, with a mixed layer depth of more than six times that in CLN at 3000 m (Fig. 4.11b).

4.4 Discussion

The findings presented in this study have important implications for glacio-hydrological studies in the Karakoram, as they suggest that neglecting supraglacial debris will result in a strong overestimation, of more than a third, of glacier mass loss during the ablation season. In addition, exposed debris alters near-surface meteorological fields and their elevational lapse rates, which are often key modelling parameters used to extrapolate forcing data from a point location (e.g., an automatic weather station) over the rest of the glacier surface (e.g. Marshall et al., 2007;

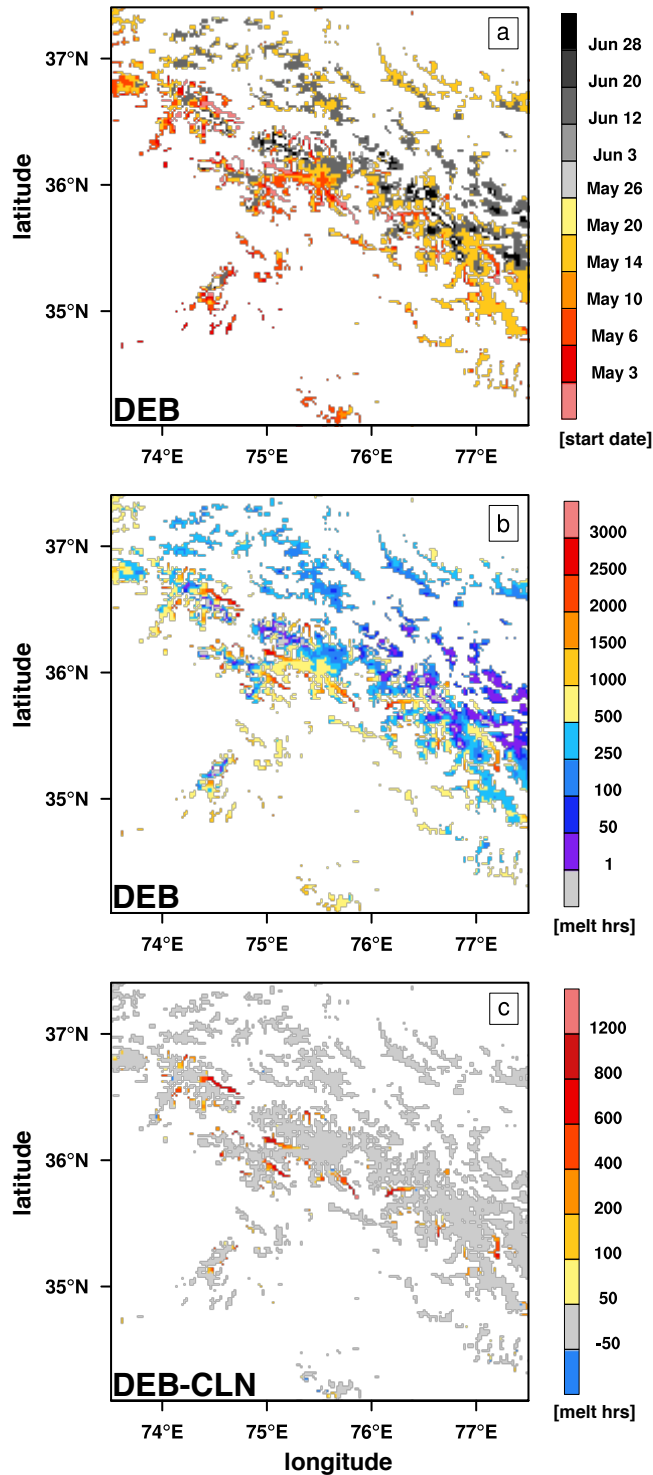


Figure 4.9: For the DEB simulation, (a) date of the start of the summer melt season and (b) total number of hours where surface temperatures reach or exceed the melting point (melt hours). (c) Difference in total melt hours between the two simulations.

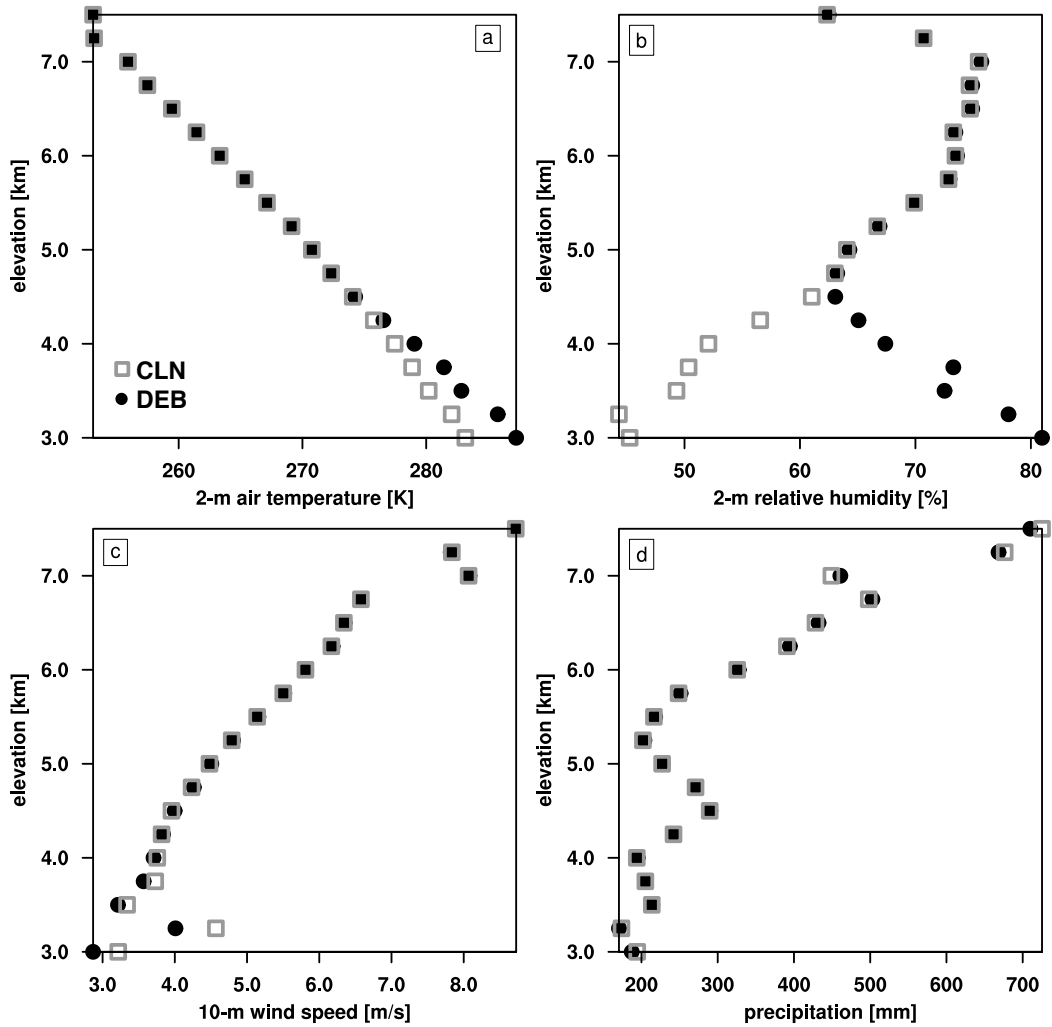


Figure 4.10: Elevation profiles of (a) air temperature [K] and (b) relative humidity [%] at a height of 2m; (c) wind speed at a height of 10 m; (d) accumulated precipitation, from the DEB (black-circle markers) and CLN (grey-square) simulations. The temporal averaging period is 1 July to 1 October 2004.

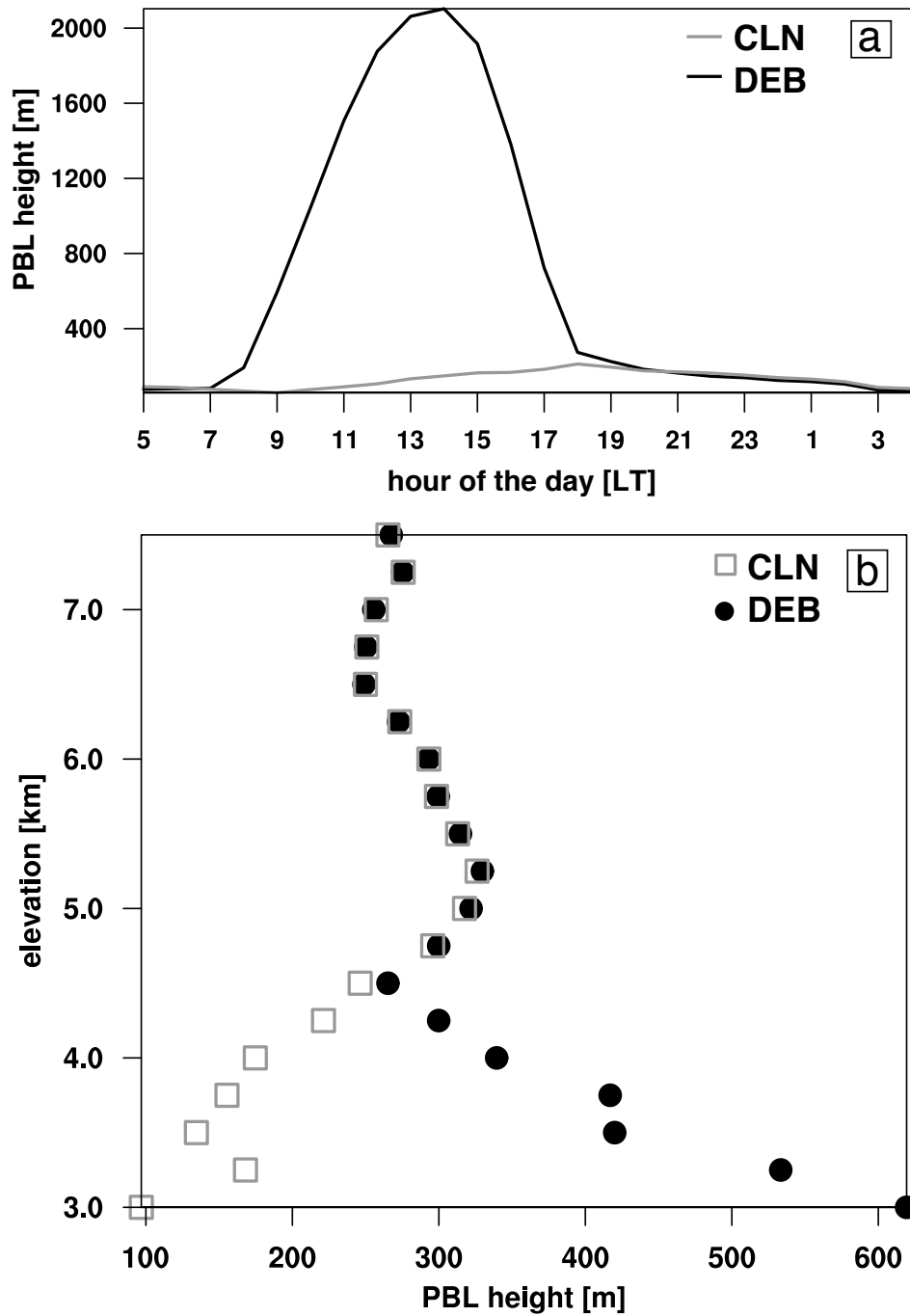


Figure 4.11: (a) Elevation profile and (b) diurnal cycle of the planetary boundary layer height over exposed debris in DEB (black markers and curve) and their equivalent pixels in CLN (grey).

Gardner et al., 2009; Reid et al., 2012). For temperature, the lapse rate at lower elevations is significantly steeper in DEB, as a result of surface temperatures exceeding the melting point and a net turbulent transfer of sensible heat to the atmosphere that gives higher near-surface air temperatures (cf. Fig. 4.10a, Table 4.5). Debris also supports the development of a deeper convective mixed layer during the daytime, which gives an elevational lapse rate in temperature approaching the dry adiabatic lapse rate. The simulated temperature gradients are steeper than values reported for debris-covered glaciers spanning a smaller elevational extent (Reid et al., 2012) and in high-altitude catchments in the eastern Himalaya, where the monsoon circulation system plays a more pronounced role (Immerzeel et al., 2014). For near-surface humidity, evaporation from the debris layer contributes to a reversal of the near-surface humidity gradient in the ablation zone, with implications for studies that neglect QL in their calculation of the surface energy balance as is frequently done in numerical studies of debris cover (e.g. Reid and Brock, 2010; Reid et al., 2012; Lejeune et al., 2013).

Simulated ice ablation rates in DEB under thicker debris covers at lower elevations are consistent with the findings of Mihalcea et al. (2006) of non-negligible melt energy under debris covers exceeding 1 m using a degree-day modelling approach for the Baltoro glacier, and with the measured rates under the thickest debris reported by Mayer et al. (2010). The authors of the latter study suggest the mechanism is more efficient heat transfer in the debris in the presence of moisture during the ablation season despite its thickness. However, previous point simulations with the CMB model showed that under the same forcing, moisture decreased heat transfer through the debris layer by a reduction in the effective thermal diffusivity of saturated layers (i.e., increases in the layer density and specific heat dominated over increases in the thermal conductivity; Collier et al., 2014). In this study, daily mean ice melt rates for pixels with debris thickness exceeding 20 cm have a small inverse correlation with debris ice content ($R^2=0.37$). However, near-surface air temperature ($R^2=0.74$) seems to be a stronger driver of melt rates below thick debris. This result may arise from the interactive nature of the simulation, which permits a positive feedback mechanism: warmer surface temperatures over thicker debris transfer heat energy to the atmosphere that in turn promotes further melt. In combination with surface heterogeneity in the ablation zone (e.g., the presence of meltwater

ponds and ice cliffs) and recent changes in ice flow velocities (Quincey et al., 2009; Scherler and Strecker, 2012), the simulated melt rates under thicker debris help to explain the lack of significant differences in recent elevation changes between debris-free and debris-covered glacier surfaces in the Karakoram (Gardelle et al., 2013).

The impact on glacier mass fluxes and on atmosphere-glacier interactions presented in this study may represent an underestimate, since more than 50 % of debris-covered pixels remained snow-covered during the study period. Absolute values may be affected by the fact that the clean snow/ice mask of Kääb et al. (2012) used to delineate debris-covered areas was generated from Landsat data from the year 2000, therefore some differences may arise due to different snow accumulation between the two periods or to our binary assignment of surface types as debris-covered or debris-free. In addition, although measurements are unavailable, wind redistribution of snow and sublimation of blowing snow are thought to play important roles in snow removal in the Karakoram (Winiger et al., 2005) and Nepalese Himalaya (Wagnon et al., 2013) but are not included in WRF-CMB. Finally, overestimation of nighttime cooling resulting from excessive damping of QS in stable conditions could contribute to an underestimation of snowmelt, which points to the need to improve the stability corrections for applications at high altitudes.

The exact changes to ablation-season glacier surface-energy and mass dynamics are sensitive to the debris thickness specification, which is represented as an idealized field in this study. There have been numerous recent efforts to more precisely determine debris thickness fields using satellite-derived surface temperature fields (e.g. Suzuki et al., 2007; Mihalcea et al., 2008; Foster et al., 2012; Brenning et al., 2012), which is an appealing solution due to the wide spatial and temporal coverage of remote sensing data. However, none of these studies has successfully reproduced field measurements without using empirically-determined relationships or calibration factors (Mihalcea et al., 2008; Foster et al., 2012). These methods are therefore best suited for debris-covered glaciers for which the necessary measurements to compute the relationships or factors are available, and their applicability for regional-scale studies such as this one is uncertain. Generating a more detailed debris thickness field for the Karakoram, as well as accounting for sub-grid scale heterogeneity (for example, by introducing a treatment of ice cliffs; Reid and Brock, 2014), remain important future steps for more spatially detailed studies of glacier CMB

in this region.

4.5 Conclusions

The introduction of debris to the coupled atmosphere-glacier modelling system WRF-CMB provides a novel tool to investigate the influence of debris cover on both Karakoram glaciers and atmosphere-glacier interactions in an explicitly resolved framework. Robust feedbacks between the glacier surface and atmosphere were simulated over exposed debris pixels, with strong alterations to the surface energy balance, near-surface meteorological fields and boundary layer dynamics. Of particular note is the manner in which debris affects the altitudinal lapse rates of atmospheric fields, as lapse rates are often used to extrapolate point meteorological measurements over glacier surfaces. It could prove particularly important to account for modifications in the lapse rates when modelling melt rates at location of enhanced subaerial melt within the debris covered terminus, such as at exposed ice cliffs. Furthermore, a large impact was demonstrated on glacier ablation, in particular at lower elevations, with a 30% reduction in mass loss at the end of the ablation season. By providing an estimate of the controlling influence of debris on glaciers, these simulations contribute to a greater understanding of glacier behaviour in the Karakoram.

References

- Benn, D.I., and Lehmkuhl, F.: Mass balance and equilibrium-line altitudes of glaciers in high-mountain environments, *Quat. Int.*, 65, 15-29, 2000.
- Bolch, T., Kulkarni, A., Käab, A., Huggel, C., Paul, F., Cogley, J. G., Frey, H., Kargel, J. S., Fujita, K., Scheel, M., Bajracharya, S., and Stoffel, M.: The state and fate of Himalayan glaciers, *Science*, 336, 310–314, 2012.
- Braithwaite, R. J.: Aerodynamic stability and turbulent sensible-heat flux over a melting ice surface, the Greenland ice sheet, *J. Glaciol.*, 41, 562–571, 1995.
- Brenning, A., Pea, M. A., Long, S., and Soliman, A.: Thermal remote sensing of ice-debris landforms using ASTER: an example from the Chilean Andes. *The Cryosphere*, 6, 367-382, 2012.
- Brock, B. W., Mihalcea, C., Kirkbride, M. P., Diolaiuti, G., Cutler, M. E., and Smiraglia, C.: Meteorology and surface energy fluxes in the 2005–2007 ablation seasons at the Miage debris-covered glacier, Mont Blanc Massif, Italian Alps. *J. Geophys. Res.*, 115, D09106, doi:10.1029/2009JD013224, 2010.
- Brodzik, M. J., Armstrong, R., and Savoie, M.: Global EASE-Grid 8-day Blended SSM/I and MODIS Snow Cover, National Snow and Ice Data Center, Boulder, Colorado, USA, Digital media, 2007.
- Chen, F. and Dudhia, J.: Coupling an advanced land surface-hydrology model with the Penn State – NCAR MM5 modelling system. Part I: Model implementation and sensitivity, *Mon. Weather Rev.*, 129, 569–585, 2001.

- Clark, S. P. Jr. (Eds): Thermal conductivity. In: Handbook of Physical Constants – Revised Edition, The Geological Society of America Memoir 97, New York, Geological Society of America, 459–482, 1966.
- Cogley, J. G.: Present and future states of Himalaya and Karakoram glaciers, *Ann. Glaciol.*, 52, 69–73, 2011.
- Collier, E., Mölg, T., Maussion, F., Scherer, D., Mayer, C., and Bush, A. B. G.: High-resolution interactive modelling of the mountain glacier–atmosphere interface: an application over the Karakoram, *The Cryosphere*, 7, 779–795, 2013.
- Collier, E., Nicholson, L. N., Brock, B. W., Maussion, F., Essery, R., and Bush, A., B., G.: Representing moisture fluxes and phase changes in glacier debris cover using a reservoir approach, *The Cryosphere*, 8, 1429–1444, 2014.
- Collins, W. D., Rasch, P. J., Boville, B. A., Hack, J. J., McCaa, J. R., Williamson, D., L., Kiehl, J., T., Briegleb, B., Bitz, C., Lin, S-J., Zhang, M., and Dai, Y.: Description of the NCAR Community Atmosphere Model (CAM3.0). Technical Note TN-464+STR, National Center for Atmospheric Research, Boulder, CO, 214 pp.
- Conway, J. P., and Cullen, N. J.: Constraining turbulent heat flux parameterization over a temperate maritime glacier in New Zealand, *Ann. Glaciol.*, 54, 41–51, 2013.
- Conway, H. and Rasmussen, L. A.: Summer temperature profiles within supraglacial debris on Khumbu Glacier, Nepal, *Debris-Covered Glaciers*, IAHS PUBLICATION no. 264, 89–97, 2000.
- Copland, L., Sylvestre, T., Bishop, M. P., Shroder, J. F., Seong, Y. B., Owen, L. A., Bush, A., and Kamp, U.: Expanded and recently increased glacier surging in the Karakoram, *Arct. Antarct. Alp. Res.*, 43, 503516, 2011.
- Daly, R. A., Manger, G. E., Clark, S. P. Jr.: Density of Rocks. In: Handbook of Physical Constants – Revised Edition, The Geological Society of America Memoir 97, Clark, S. P. Jr. (Eds), New York, Geological Society of America, 19–26, 1966.

- Dee, D. P., Uppala, S. M., Simmons, A. J., Berrisford, P., Poli, P., Kobayashi, S., Andrae, U., Balmaseda, M. A., Balsamo, G., Bauer, P., Bechtold, P., Beljaars, A. C. M., van de Berg, L., Bidlot, J., Bormann, N., Delsol, C., Dragani, R., Fuentes, M., Geer, A. J., Haimberger, L., Healy, S. B., Hersbach, H., Hlm, E. V., Isaksen, L., Kållberg, P., Köhler, M., Matricardi, M., McNally, A. P., Monge-Sanz, B. M., Morcrette, J.-J., Park, B.-K., Peubey, C., de Rosnay, P., Tavolato, C., Thpaut, J.-N., and Vitart, F.: The ERA-Interim reanalysis: configuration and performance of the data assimilation system, *Q. J. Roy. Meteorol. Soc.*, 137, 553–597, 2011.
- Foster, L. A., Brock, B. W., Cutler, M. E. J., and Diotri, F.: A physically based method for estimating supraglacial debris thickness from thermal band remote-sensing data, *J. Glaciol.*, 58, 677–691, 2012.
- Fujii, Y.: Experiment on glacier ablation under a layer of debris cover, *J. Japan. Soc. Snow Ice (Seppyo)*, 39, 20–21, 1977.
- Gardelle, J., Berthier, E., and Arnaud, Y.: Slight mass gain of Karakoram glaciers in the early twenty-first century, *Nat. Geosci.*, 5, 322–325, 2012.
- Gardelle, J., Berthier, E., and Arnaud, Y.: Region-wide glacier mass balances over the Pamir-Karakoram-Himalaya during 1999-2011, *The Cryosphere*, 7, 1263–1286, 2013.
- Gardner, A. S., Sharp, M. J., Koerner, R. M., Labine, C., Boon, S., Marshal, S. J., Burgess, D. O., and Lewis, E.: Near-surface temperature lapse rates over Arctic glaciers and their implications for temperature downscaling, *J. Climate*, 22, 4281–4298, 2009.
- Giesen, R. H., Andreassen, L. M., Van den Broeke, M. R., and Oerlemans, J.: Comparison of the meteorology and surface energy balance at Storbreven and Midtdalsbreen, two glaciers in southern Norway, *The Cryosphere*, 3, 57-74, 2009.
- Granger, R. J., Pomeroy, J. W., and Parviainen, J.: Boundary layer integration approach to advection of sensible heat to a patchy snow cover, 59th Eastern Snow Conference, Stowe, Vermont, 2002.
- Hewitt, K.: The Karakoram anomaly? Glacier expansion and the “elevation effect” Karakoram Himalaya, *Mt. Res. Dev.*, 25, 332–340, 2005.

- Hewitt, K.: Glacier change, concentration, and elevation effects in the Karakoram Himalaya, Upper Indus Basin, *Mt. Res. Dev.*, 31, 188–200, 2011.
- Hong, S.-Y., Noh, Y., and Dudhia, J.: A new vertical diffusion package with an explicit treatment of entrainment processes, *Mon. Wea. Rev.*, 134, 2318–2341, 2006.
- Immerzeel, W. W., Kraaijenbrink, P. D. a., Shea, J. M., Shrestha, A. B., Pellicciotti, F., Bierkens, M. F. P., and de Jong, S. M.: High-resolution monitoring of Himalayan glacier dynamics using unmanned aerial vehicles, *Remote Sens. Environ.*, 150, 93-103, 2014.
- Immerzeel, W. W., Petersen, L., Ragettli, S., and Pellicciotti, F.: The importance of observed gradients of air temperature and precipitation for modeling runoff from a glacierized watershed in the Nepalese Himalaya, *Water Resour. Res.*, 50, 2212-2226, doi::10.1002/2013WR014506, 2014.
- Inoue, J. and Yoshida, M.: Ablation and heat exchange over the Khumbu Glacier, *J. Japan. Soc. Snow Ice (Seppyo)*, 39, 7–14, 1980.
- Jiménez, P. A., Dudhia, J., González-Rouco, J. F., Navarro, J., Montávez, J. P., and García-Bustamante, E.: A revised scheme for the WRF surface layer formulation, *Mon. Weather Rev.*, 140, 898–918, 2012.
- Kain, J. S.: The KainFritsch convective parameterization: An update, *J. Appl. Meteor.*, 43, 170-181, 2004.
- Kääb, A., Berthier, E., Nuth, C., Gardelle, J., and Arnaud, Y.: Contrasting patterns of early twenty-first-century glacier mass change in the Himalayas, *Nature*, 488, 495–498, 2012.
- Kaser, G., Großhauser, M., and Marzeion, B.: Contribution potential of glaciers to water availability in different climate regimes, *Proc. Natl. Acad. Sci.*, 107, 20223-20227, 2010.
- Lejeune, Y., Bertrand, J.-M., Wagnon, P., and Morin, S.: A physically based model of the year-round surface energy and mass balance of debris-covered glaciers, *J. Glaciol.*, 59, 327–344, 2013.

- Loomis, S. R.: Morphology and ablation processes on glacier ice, *Assoc. Am. Geogr. Proc.*, 2, 88–92, 1970.
- Lutz, A. F., Immerzeel, W. W., Shrestha, A. B., and Bierkens, M. F. P.: Consistent increase in High Asia's runoff due to increasing glacier melt and precipitation, *Nat. Clim. Chang.*, 4, 16, 2014.
- Marshall, S. J., Sharp, M. J., Burgess, D. O., and Anslow, F. S.: Surface temperature lapse rate variability on the Prince of Wales Ice-eld, Ellesmere Island, Canada: implications for regional-scale downscaling of temperature, *Int. J. Climatol.*, 27, 385–398, 2007.
- Martin, E., and Lejeune, Y.: Turbulent fluxes above the snow surface, *Ann. Glaciol.*, 26, 179–183, 1998.
- Mattson, L. E., Gardner, J. S., and Young, G. J.: Ablation on debris covered glaciers: an example from the Rakhiot Glacier, Punjab, Himalaya, *Snow and Glacier Hydrology, IAHS-IASH Publ.*, 218, 289–296, 1993.
- Maussion, F., Scherer, D., Mlg, T., Collier, E., Curio, J., and Finkelnburg, R.: Precipitation seasonality and variability over the Tibetan Plateau as resolved by the High Asia Reanalysis, *J. Climate*, 27, 1910–1927, 2014.
- Mayer, C., Lambrecht, A., Mihalcea, C., Belo, M., Diolaiuti, G., Smiraglia, C., and Bashir, F.: Analysis of Glacial Meltwater in Bagrot Valley, Karakoram, *Mtn. Res. Dev.*, 30, 169–177, 2010.
- Mayer, C., Lambrecht, A., Oerter, H., Schwikowski, M., Vuillermoz, E., Frank, N., and Diolaiuti, G.: Accumulation Studies at a High Elevation Glacier Site in Central Karakoram, *Adv. Meteorol.*, 2014, 1–12, 2014.
- Mihalcea, C., Mayer, C., Diolaiuti, G., Smiraglia, C., and Tartari, G.: Ablation conditions on the debris covered part of Baltoro Glacier, Karakoram, *Ann. Glaciol.*, 43, 292–300, 2006.
- Mihalcea, C., Mayer, C., Diolaiuti, G., DAgata, C., Smiraglia, C., Lambrecht, A., Vuillermoz, E., and Tartari, G.: Spatial distribution of debris thickness and melting from remote-sensing and

- meteorological data, at debris-covered Baltoro glacier, Karakoram, Pakistan, *Ann. Glaciol.*, 48, 49–57, 2008.
- Molinari, J. and Dudek, M.: Parameterization of convective precipitation in mesoscale numerical-models – a critical-review, *Mon. Weather Rev.*, 120, 326–344, 1992.
- Mölg, T., Cullen, N. J., Hardy, D. R., Kaser, G., and Klok, E. J.: Mass balance of a slope glacier on Kilimanjaro and its sensitivity to climate, *Int. J. Climatol.*, 28, 881–892, 2008.
- Mölg, T., Cullen, N. J., Hardy, D. R., Winkler, M., and Kaser, G.: Quantifying climate change in the tropical midtroposphere over East Africa from glacier shrinkage on Kilimanjaro, *J. Climate*, 22, 4162–4181, 2009.
- Nicholson, L. and Benn, D.: Properties of natural supraglacial debris in relation to modelling sub-debris ice ablation, *EPSL*, 38, 490–501, 2012.
- Niu, G.-Y., Yang, Z.-L., Mitchell, K. E., Chen, F., Ek, M. B., Barlage, M., Kumar, A., Manning, K., Niyogi, D., Rosero, E., Tewari, M., and Youlong, X.: The community Noah land surface model with multiparameterization options (Noah-MP): 1. Model description and evaluation with local-scale measurements, *J. Geophys. Res.*, 116, D12109, doi:10.1029/2010JD015139, 2011.
- Østrem, G.: Ice melting under a thin layer of moraine, and the existence of ice cores in moraine ridges, *Geogr. Ann.*, 41, 228–230, 1959.
- Pellicciotti, F., Stephan, C., Miles, E., Immerzeel, W. W., and Bolch, T.: Mass balance changes of the debris-covered glaciers in the Langtang Himal in Nepal between 1974 and 1999, *J. Geophys. Res.*, in Press., 127.
- Pfeffer, W. T., Arendt, A., Bliss, A., Bolch, T., Cogley, J. G., Gardner, A. S., Hagen, J.-O., Hock, R., Kaser, G., Kienholz, C., Miles, E. S., Moholdt, G., Mölg, N., Paul, F., Radic, V., Rastner, P., Raup, B. H., Rich, J., and Sharp, M. J.: The Randolph Glacier Inventory: a globally complete inventory of glaciers, *J. Glaciol.*, 221, 537–552, 2014.

- Quincey, D. J., Copland, L., Mayer, C., Bishop, M., Luckman, A., and Belo, M.: Ice velocity and climate variations for Baltoro Glacier, Pakistan, *J. Glaciol.*, 55, 1061–1071, 2009.
- Rankl, M., Kienholz, C., and Braun, M.: Glacier changes in the Karakoram region mapped by multimission satellite imagery, *The Cryosphere*, 8, 977–989, 2014.
- Reid, T. D. and Brock, B. W.: An energy-balance model for debris-covered glaciers including heat conduction through the debris layer, *J. Glaciol.*, 56, 903–916, 2010.
- Reid, T. D., Carenzo, M., Pellicciotti, F., and Brock, B. W.: Including debris cover effects in a distributed model of glacier ablation, *J. Geophys. Res.*, 117, D18105, doi:10.1029/2012JD017795, 2012.
- Reid, T. D. and Brock, B. W.: Assessing ice-cliff backwasting and its contribution to total ablation of debris-covered Miage glacier, Mont Blanc massif, Italy, *J. Glaciol.*, 60, 3–13, 2014.
- Sakai, A., Nakawo, M., and Fujita, K.: Melt rate of ice cliffs on the Lirung Glacier, Nepal Himalayas, 1996. *Bull. Glacier Res.*, 16, 57-66, 1998.
- Sakai, A., Takeuchi, N., Fujita, K., and Nakawo, N.: Role of supraglacial ponds in the ablation process of a debris-covered glacier in the Nepal Himalaya. *Debris-Covered Glaciers*, IAHS PUBLICATION no. 264, 119–130, 2000.
- Scherler, D., Bookhagen, B., and Strecker, M. R.: Spatially variable response of Himalayan glaciers to climate change affected by debris cover, *Nat. Geosci.*, 4, 156–159, 2011.
- Scherler, D., and Strecker, M. R.: Large surface velocity fluctuations of Biafo Glacier, central Karakoram, at high spatial and temporal resolution from optical satellite images, *J. Glaciol.*, 58, 569-580, 2012.
- Skamarock, W. C. and Klemp, J. B.: A time-split nonhydrostatic atmospheric model for weather research and forecasting applications, *J. Comput. Phys.*, 227, 3465–3485, 2008.
- Suzuki, R., Fujita, K., and Ageta, Y.: Spatial distribution of thermal properties on debris-covered glaciers in the Himalayas derived from ASTER data, *Bull. Glaciol. Res.*, 24, 13–22, 2007.

- Takeuchi, Y., Kayastha, R. B., and Nakawo, M.: Characteristics of ablation and heat balance in debris-free and debris-covered areas on Khumbu glacier, Nepal Himalayas, in the pre-monsoon season, in: *Debris-covered glaciers*, IAHS Publ., 264, 53–61, 2000.
- Takeuchi, Y., Kayastha, R. B., Naito, N., Kadota, T., and Izumi, K.: Comparison of meteorological features in the debris-free and debris-covered areas at Khumbu Glacier, Nepal Himalayas, in the premonsoon season, 1999, *Bull. Glaciol. Res.*, 18, 15–18, 2001.
- Thompson, G., Field, P. R., Rasmussen, R. M., and Hall, W. D.: Explicit forecasts of winter precipitation using an improved bulk microphysics scheme. Part II: Implementation of a new snow parameterization, *Mon. Wea. Rev.*, 136, 5095–5115, 2008.
- Wagnon, P., Vincent, C., Arnaud, Y., Berthier, E., Vuillermoz, E., Gruber, S., Ménégoz, M., Gilbert, A., Dumont, M., Shea, J. M., Stumm, D., and Pokhrel, B. K.: Seasonal and annual mass balances of Mera and Pokalde glaciers (Nepal Himalaya) since 2007, *The Cryosphere*, 7, 1769–1786, 2013.
- Weisman, M. L., Skamarock, W. C., and Klemp, J. B.: The resolution dependence of explicitly modeled convective systems, *Mon. Weather Rev.*, 125, 527–548, 1997.
- Winiger, M., Gumpert, M., and Yamout, H.: KarakorumHindukushwestern Himalaya: assessing highaltitude water resources, *Hydrol. Process.*, 19, 2329–2338, 2005.
- Yao, T.: *Map of the Glaciers and Lakes on the Tibetan Plateau and Adjoining Regions*, Xian Cartographic Publishing House, Xian, China, 2007.
- Zhang, Y., Fujita, K., Liu, S., Liu, Q., and Nuimura, T.: Distribution of debris thickness and its effect on ice melt at Hailuoguo glacier, southeastern Tibetan Plateau, using in situ surveys and ASTER imagery, *J. Glaciol.*, 57, 1147–1157, 2011.

Chapter 5

Perspectives for future research

The interactively coupled atmosphere-glacier model is a promising, multi-scale approach to simulations of alpine glacier CMB. At the time of its development, WRF-CMB represented an important interdisciplinary advancement, as it was the first explicit treatment of alpine glaciers in a regional atmospheric model. The coupled model provides a more consistent approach to obtaining meteorological forcing data for simulations of glacier CMB than does an atmospheric model alone, as changing glacier surface conditions (e.g., the exposure of glacier ice or debris) can influence the atmosphere.

Short simulations of the Karakoram showed that WRF-CMB is capable of reproducing observed magnitudes of glacier CMB during an ablation season, with small improvements arising from the inclusion of glacier feedbacks. The results highlighted the strong potential impact of debris on ablation and atmosphere-glacier feedbacks, and underscored the importance of treating debris for accurate simulations of Karakoram glacier response to climate change. This finding is especially relevant given observations of a rising proportion of debris-covered area in the HKH, concurrent with glacier retreat (Bolch et al., 2008; Bhambri et al., 2011).

However, the research presented in this thesis has relied on a number of simplifying assumptions. For seasonal and annual simulations with WRF-CMB, for example, a grid-spacing on the order of one kilometer is computationally practical. At this resolution, the largest glaciers in the Karakoram are represented by only 1 to 2 pixels in width compared with ~ 30 pixels in length and, thus, longitudinal rather than transverse gradients in glacier surface conditions

are captured. In addition, many important features remain unresolved, including debris-covered areas in the upper ablation zone that fall below the 40% threshold used to classify a pixel as debris-covered, as well as the presence of features such as ice cliffs and meltwater ponds further down-glacier. Furthermore, supraglacial debris has been treated as having horizontally homogeneous whole-rock thermal and optical properties, while in reality the lithology shows strong spatial variability. In the vicinity of the Baltoro glacier, for example, the debris is likely a mixture of granites, gneisses and sedimentary rocks (Searle, 1991). These limitations could be improved upon in future work by introducing a subgrid-scale glacier treatment, in which debris-free and debris-covered solutions are averaged in each pixel according to the fractional debris coverage and using representative values for the thickness and lithological properties.

An additional key assumption of this work is that the simple parameterization of the latent heat flux at the debris surface developed in Chapter 3 using field data from the Alps is both transferrable to the Karakoram and valid over the range of debris thicknesses used in Chapter 4. The appropriateness of this assumption should be investigated by gathering eddy covariance measurements of the turbulent fluxes over areas with a range of debris thicknesses in the Karakoram. As the glacier model does not treat horizontal transport of liquid water, we have also assumed that any water that exceeds the snowpack holding capacity runs off instantaneously from the glacier. Therefore, the accuracy of simulations of glacier runoff could be improved by accounting for the horizontal transport and potential refreeze of liquid water elsewhere on the glacier. Finally, over longer simulation periods, two additional factors should be accounted for: (1) the dynamical response of Karakoram glaciers, including flow instabilities, as Copland et al. (2011) found that this region contains the second largest concentration of surge-type glaciers at mid-latitudes; and, (2) temporal variability in debris distribution, due to sources (e.g., deposition by avalanches; Scherler et al., 2011b) as well as to both surficial and englacial transport.

Despite these simplifications, the coupled model provides one of the most comprehensive tools currently available for determining the causes of the Karakoram anomaly, as it permits the direct attribution of glacier CMB fluctuations to regional atmospheric drivers and to the local influences of debris cover and orography. The next step for understanding recent glacier

change in the Karakoram is to perform a longer simulation using WRF-CMB, spanning the 1990s and 2000s. The availability of glacier CMB over a longer time span will permit evaluation of the results against recent geodetic studies (Gardelle et al., 2012, 2013; Kääb et al., 2012). In addition, such a simulation would facilitate the following aims:

(1) *Investigation of seasonal and interannual variability in precipitation dynamics*

The Karakoram, and HKH in general, is influenced by two main circulation systems: the westerlies and the Asian monsoon (Bookhagen et al., 2010). The influence of the monsoon system on precipitation has been reported to be minimal west of 77°E (e.g. Barros et al., 2004), congruent with high-resolution atmospheric modelling of glacier accumulation regimes whose results emphasize the importance of the winter and spring seasons (Chapter 4; Maussion et al., 2014). However, analysis of the chemical composition of snow in the central Karakoram points to seasonally differentiated marine sources for precipitation (Wake, 1989), with at least occasional moisture inputs from the monsoon circulation system during the summer. Therefore, there is a need to elucidate the relative contribution of these circulation systems on a seasonal basis as well as variations from year to year under the influence of large-scale internal atmospheric variability.

(2) *Linking interannual variations in atmospheric conditions to changes in glacier CMB*

Interannual variability in the westerlies as well as the timing of the onset of the monsoon have been linked via a similar modelling chain to fluctuations in annual glacier balances on the Tibetan Plateau (Mölg et al., 2013). A similar analysis should be performed for the Karakoram, by comparing the insights gained in the first step with the simulated interannual variability in glacier CMB to elucidate the most relevant dynamics in the Karakoram.

References

- Barros, A. P., Kim, G., Williams, E., and Nesbitt, S. W.: Probing orographic controls in the Himalayas during the monsoon using satellite imagery, *Nat. Hazards Earth Syst. Sci.*, 4, 29-51, 2004.
- Bhambri, R., Bolch, T., Chaujar, R. K., and Kulshreshtha, S. C.: Glacier changes in the Garhwal Himalaya, India, from 1968 to 2006 based on remote sensing, *J. Glaciol.*, 57, 543–556, 2011.
- Bolch, T., Buchroithner, M., Pieczonka, T., and Kunert, A.: Planimetric and volumetric glacier changes in the Khumbu Himal, Nepal, since 1962 using Corona, Landsat TM and ASTER data, *J. Glaciol.*, 54, 592–600, 2008.
- Bookhagen, B., and Burbank, D. W.: Toward a complete Himalayan hydrological budget: Spatiotemporal distribution of snowmelt and rainfall and their impact on river discharge, *J. Geophys. Res.*, 115, doi:10.1029/2009JF001426, 2010.
- Copland, L., Sylvestre, T., Bishop, M. P., Shroder, J. F., Seong, Y. B., Owen, L. A., Bush, A., and Kamp, U.: Expanded and recently increased glacier surging in the Karakoram, *Arct. Antarct. Alp. Res.*, 43, 503516, 2011.
- Kääb, A., Berthier, E., Nuth, C., Gardelle, J., and Arnaud, Y.: Contrasting patterns of early twenty-first-century glacier mass change in the Himalayas, *Nature*, 488, 495–498, 2012.
- Maussion, F., Scherer, D., Mlg, T., Collier, E., Curio, J., and Finkelnburg, R.: Precipitation seasonality and variability over the Tibetan Plateau as resolved by the High Asia Reanalysis, *J. Climate*, 27, 1910–1927, 2014.

Mölg, T., Maussion, F., and Scherer, D.: Mid-latitude westerlies as a driver of glacier variability in monsoonal High Asia, *Nat. Clim. Change*, 4, 68–73, 2013.

Searle, M. P.: *Geology and Tectonics of the Karakoram Mountains*, John Wiley and Sons, Chichester, 1991.

Wake, C. P.: Glaciochemical investigations as a tool for determining the spatial and seasonal variation of snow accumulation in the central Karakoram, northern Pakistan. *Ann. Glaciol.*, 13, 279–284, 1989.

Works Cited

- Adhikary, S., Seko, K., Nakawo, M., Ageta, Y., and Miyazaki, N.: Effect of surface dust on snow melt, *Bull. Glacier Res.*, 15, 85–92, 1997.
- Archer, D. R., and Fowler, H. J.: Spatial and temporal variations in precipitation in the Upper Indus Basin, global teleconnections and hydrological implications, *Hydrol. Earth Syst. Sci.*, 8, 47-61, 2004.
- Aubinet, M., Vesala, T., and Papale, D. (Eds.): *Eddy Covariance: a Practical Guide to Measurement and Data Analysis*, Springer, Dordrecht, Heidelberg, London, New York, 2012.
- Azam, M. F., Wagnon, P., Ramanathan, A., Vincent, C., Sharma, P., Arnaud, Y., Linda, A., Pottakkal, J. G., Chevallier, P., Singh, V. B., and Berthier, E.: From balance to imbalance: a shift in the dynamic behaviour of Chhota Shigri glacier, western Himalaya, India, *J. Glaciol.*, 58, 315–324, 2012.
- Barros, A. P., Kim, G., Williams, E., and Nesbitt, S. W.: Probing orographic controls in the Himalayas during the monsoon using satellite imagery, *Nat. Hazards Earth Syst. Sci.*, 4, 29-51, 2004.
- Benn, D.I., and Lehmkuhl, F.: Mass balance and equilibrium-line altitudes of glaciers in high-mountain environments, *Quat. Int.*, 65, 15-29, 2000.
- Bhambri, R., Bolch, T., Chaujar, R. K., and Kulshreshtha, S. C.: Glacier changes in the Garhwal Himalaya, India, from 1968 to 2006 based on remote sensing, *J. Glaciol.*, 57, 543–556, 2011.
- Bolch, T., Buchroithner, M., Pieczonka, T., and Kunert, A.: Planimetric and volumetric glacier

- changes in the Khumbu Himal, Nepal, since 1962 using Corona, Landsat TM and ASTER data, *J. Glaciol.*, 54, 592–600, 2008.
- Bolch, T., Kulkarni, A., Kääb, A., Huggel, C., Paul, F., Cogley, J. G., Frey, H., Kargel, J. S., Fujita, K., Scheel, M., Bajracharya, S., and Stoffel, M.: The state and fate of Himalayan glaciers, *Science*, 336, 310–314, 2012.
- Bookhagen, B., and Burbank, D. W.: Toward a complete Himalayan hydrological budget: Spatiotemporal distribution of snowmelt and rainfall and their impact on river discharge, *J. Geophys. Res.*, 115, doi:10.1029/2009JF001426, 2010.
- Braithwaite, R. J.: Aerodynamic stability and turbulent sensible-heat flux over a melting ice surface, the Greenland ice sheet, *J. Glaciol.*, 41, 562–571, 1995.
- Brenning, A., Pea, M. A., Long, S., and Soliman, A.: Thermal remote sensing of ice-debris landforms using ASTER: an example from the Chilean Andes. *The Cryosphere*, 6, 367-382, 2012.
- Brock, B., Mihalcea, C., Citterio, M., D’Agata, C., Cutler, M., Diolaiuti, G., Kirkbride, M. P., Maconachie, H., and Smiraglia, C.: Spatial and temporal patterns of thermal resistance and heat conduction on debris-covered Miage Glacier, Italian Alps, *Geophysical Research Abstracts*, European Geosciences Union General Assembly, Vienna, Austria, 2–7 April 2006, Vol. 8, ISSN: 1029-7006, 2006.
- Brock, B. W., Mihalcea, C., Kirkbride, M. P., Diolaiuti, G., Cutler, M. E., and Smiraglia, C.: Meteorology and surface energy fluxes in the 2005–2007 ablation seasons at the Miage debris-covered glacier, Mont Blanc Massif, Italian Alps. *J. Geophys. Res.*, 115, D09106, doi:10.1029/2009JD013224, 2010.
- Brodzik, M. J., Armstrong, R., and Savoie, M.: Global EASE-Grid 8-day Blended SSM/I and MODIS Snow Cover, National Snow and Ice Data Center, Boulder, Colorado, USA, Digital media, 2007.
- Bryan, G. H., Wyngaard, J. C., and Fritsch, J.: Resolution requirements for simulations of deep moist convection, *Mon. Weather Rev.*, 131, 2394–2416, 2003.

- Chen, F. and Dudhia, J.: Coupling an advanced land surface-hydrology model with the Penn State – NCAR MM5 modelling system. Part I: Model implementation and sensitivity, *Mon. Weather Rev.*, 129, 569–585, 2001.
- Claremar, B., Obleitner, F., Reijmer, C., Pohjola, V., Waxegård, A., Karner, F., and Rutgersson, A.: Applying a mesoscale atmospheric model to Svalbard glaciers, *Adv. Meteorol.*, 2012, 321649, doi:10.1155/2012/321649, 2012.
- Clark, S. P. Jr. (Eds): Thermal conductivity. In: *Handbook of Physical Constants – Revised Edition*, The Geological Society of America Memoir 97, New York, Geological Society of America, 459–482, 1966.
- Cogley, J. G.: Present and future states of Himalaya and Karakoram glaciers, *Ann. Glaciol.*, 52, 69–73, 2011.
- Cogley, J. G., Hock, R., Rasmussen, L. A., Arendt, A. A., Bauder, A., Braithwaite, R. J., Jansson, P., Kaser, G., Müller, M., Nicholson, L., and Zemp, M.: *Glossary of Glacier Mass Balance and Related Terms*, IHP-VII Technical Documents in Hydrology No. 86, IACS Contribution No. 2, UNESCO-IHP, Paris, 2011.
- Collier, E., Mölg, T., Maussion, F., Scherer, D., Mayer, C., and Bush, A. B. G.: High-resolution interactive modelling of the mountain glacier–atmosphere interface: an application over the Karakoram, *The Cryosphere*, 7, 779–795, 2013.
- Collier, E., Nicholson, L. N., Brock, B. W., Maussion, F., Essery, R., and Bush, A., B., G.: Representing moisture fluxes and phase changes in glacier debris cover using a reservoir approach, *The Cryosphere*, 8, 1429-1444, 2014.
- Collins, W. D., Rasch, P. J., Boville, B. A., Hack, J. J., McCaa, J. R., Williamson, D., L., Kiehl, J., T., Briegleb, B., Bitz, C., Lin, S-J., Zhang, M., and Dai, Y.: *Description of the NCAR Community Atmosphere Model (CAM3.0)*. Technical Note TN-464+STR, National Center for Atmospheric Research, Boulder, CO, 214 pp.
- Conway, J. P., and Cullen, N. J.: Constraining turbulent heat flux parameterization over a temperate maritime glacier in New Zealand, *Ann. Glaciol.*, 54, 41–51, 2013.

- Conway, H. and Rasmussen, L. A.: Summer temperature profiles within supraglacial debris on Khumbu Glacier, Nepal, *Debris-Covered Glaciers*, IAHS PUBLICATION no. 264, 89–97, 2000.
- Copland, L., Sylvestre, T., Bishop, M. P., Shroder, J. F., Seong, Y. B., Owen, L. A., Bush, A., and Kamp, U.: Expanded and recently increased glacier surging in the Karakoram, Arct. Antarct. Alp. Res., 43, 503516, 2011.
- Craig, G. C. and Dörnback, A.: Entrainment in cumulus clouds: What resolution is cloud-resolving?, *J. Atmos. Sci.*, 65, 3978–3988, 2008.
- Dall’Amico, M., Endrizzi, S., Gruber, S., and Rigon, R.: A robust and energy-conserving model of freezing variably-saturated soil, *The Cryosphere*, 5, 469–484, 2011.
- Daly, R. A., Manger, G. E., Clark, S. P. Jr.: Density of Rocks. In: *Handbook of Physical Constants – Revised Edition*, The Geological Society of America Memoir 97, Clark, S. P. Jr. (Eds), New York, Geological Society of America, 19–26, 1966.
- Dee, D. P., Uppala, S. M., Simmons, A. J., Berrisford, P., Poli, P., Kobayashi, S., Andrae, U., Balmaseda, M. A., Balsamo, G., Bauer, P., Bechtold, P., Beljaars, A. C. M., van de Berg, L., Bidlot, J., Bormann, N., Delsol, C., Dragani, R., Fuentes, M., Geer, A. J., Haimberger, L., Healy, S. B., Hersbach, H., Hlm, E. V., Isaksen, L., Kållberg, P., Köhler, M., Matricardi, M., McNally, A. P., Monge-Sanz, B. M., Morcrette, J.-J., Park, B.-K., Peubey, C., de Rosnay, P., Tavolato, C., Thpaut, J.-N., and Vitart, F.: The ERA-Interim reanalysis: configuration and performance of the data assimilation system, *Q. J. Roy. Meteorol. Soc.*, 137, 553–597, 2011.
- Edlefsen, N. E. and Anderson, A. B. C.: Thermodynamics of soil moisture, *Hilgardia*, 15, 31–298, 1943.
- Foster, L. A., Brock, B. W., Cutler, M. E. J., and Diotri, F.: A physically based method for estimating supraglacial debris thickness from thermal band remote-sensing data, *J. Glaciol.*, 58, 677–691, 2012.
- Fowler, H., and Archer, D.: Conflicting signals of climatic change in the Upper Indus Basin, *J. Clim.*, 19, 4276–4293, 2006.

- Frey, H., Paul, F., and Strozzi, T.: Compilation of a glacier inventory for the western Himalayas from satellite data: methods, challenges, and results, *Remote Sens. Environ.*, 124, 832–843, 2012.
- Fujii, Y.: Experiment on glacier ablation under a layer of debris cover, *J. Japan. Soc. Snow Ice (Seppyo)*, 39, 20–21, 1977.
- Fyffe, C., Brock, B. W., Kirkbride, M. P., Mair, D. W. F., and Diotri, F.: The hydrology of a debris-covered glacier, the Miage Glacier, Italy, BHS Eleventh National Symposium, Hydrology for a changing world, Dundee, 9–11 July 2012, doi:10.7558/bhs.2012.ns19, 2012.
- Fyffe, C., Reid, T. D. Brock, B. W., Kirkbride, M. P., Diolaiuti, G., Smiraglia, C., and Diotri, F.: A distributed energy balance melt model of an alpine debris-covered glacier, *J. Glaciol.*, 60, 587–602, 2014.
- Gardelle, J., Berthier, E., and Arnaud, Y.: Slight mass gain of Karakoram glaciers in the early twenty-first century, *Nat. Geosci.*, 5, 322–325, 2012.
- Gardelle, J., Berthier, E., and Arnaud, Y.: Region-wide glacier mass balances over the Pamir-Karakoram-Himalaya during 1999-2011, *The Cryosphere*, 7, 1263–1286, 2013.
- Gardner, A. S., Sharp, M. J., Koerner, R. M., Labine, C., Boon, S., Marshal, S. J., Burgess, D. O., and Lewis, E.: Near-surface temperature lapse rates over Arctic glaciers and their implications for temperature downscaling, *J. Climate*, 22, 4281–4298, 2009.
- Giesen, R. H., Andreassen, L. M., Van den Broeke, M. R., and Oerlemans, J.: Comparison of the meteorology and surface energy balance at Storbreen and Midtdalsbreen, two glaciers in southern Norway, *The Cryosphere*, 3, 57-74, 2009.
- Granger, R. J., Pomeroy, J. W., and Parviainen, J.: Boundary layer integration approach to advection of sensible heat to a patchy snow cover, 59th Eastern Snow Conference, Stowe, Vermont, 2002.
- Han, H. D., Ding, Y. J., and Liu, S. Y.: A simple model to estimate ice ablation under a thick debris layer, *J. Glaciol.*, 52, 528–536, 2006.

- Hewitt, K.: The Karakoram anomaly? Glacier expansion and the “elevation effect” Karakoram Himalaya, *Mt. Res. Dev.*, 25, 332–340, 2005.
- Hewitt, K.: Glacier change, concentration, and elevation effects in the Karakoram Himalaya, Upper Indus Basin, *Mt. Res. Dev.*, 31, 188–200, 2011.
- Hong, S.-Y., Noh, Y., and Dudhia, J.: A new vertical diffusion package with an explicit treatment of entrainment processes, *Mon. Wea. Rev.*, 134, 2318–2341, 2006.
- ICIMOD (International Centre for Integrated Mountain Development): Inventory of glaciers, glacial lakes and identification of potential glacial lake outburst floods (GLOFs), affected by global warming in the Mountains of Himalayan Region, Kathmandu, DVD-ROM, 2007.
- Immerzeel, W. W., Kraaijenbrink, P. D. a., Shea, J. M., Shrestha, A. B., Pellicciotti, F., Bierkens, M. F. P., and de Jong, S. M.: High-resolution monitoring of Himalayan glacier dynamics using unmanned aerial vehicles, *Remote Sens. Environ.*, 150, 93–103, 2014.
- Immerzeel, W. W., Petersen, L., Ragettli, S., and Pellicciotti, F.: The importance of observed gradients of air temperature and precipitation for modeling runoff from a glacierized watershed in the Nepalese Himalaya, *Water Resour. Res.*, 50, 2212–2226, doi:10.1002/2013WR014506, 2014.
- Inoue, J. and Yoshida, M.: Ablation and heat exchange over the Khumbu Glacier, *J. Japan. Soc. Snow Ice (Seppyo)*, 39, 7–14, 1980.
- Jiménez, P. A., Dudhia, J., González-Rouco, J. F., Navarro, J., Montávez, J. P., and García-Bustamante, E.: A revised scheme for the WRF surface layer formulation, *Mon. Weather Rev.*, 140, 898–918, 2012.
- Karra, S. and Painter, S. L. and Lichtner, P. C.: Three-phase numerical model for subsurface hydrology in permafrost-affected regions, *The Cryosphere Discussions*, 8, 1935–1950, 2014.
- Kääb, A., Berthier, E., Nuth, C., Gardelle, J., and Arnaud, Y.: Contrasting patterns of early twenty-first-century glacier mass change in the Himalayas, *Nature*, 488, 495–498, 2012.

- Kain, J. S.: The KainFritsch convective parameterization: An update, *J. Appl. Meteor.*, 43, 170-181, 2004.
- Kaser, G.: Measurement of evaporation from snow, *Arch. Met. Geoph. Biokl. Ser. B.*, 30, 333–340, 1982.
- Kaser, G., Großhauser, M., and Marzeion, B.: Contribution potential of glaciers to water availability in different climate regimes, *Proc. Natl. Acad. Sci.*, 107, 20223-20227, 2010.
- Kayastha, R. B., Takeuchi, Y., Nakawo, M., and Ageta, Y.: Practical prediction of ice melting beneath various thickness of debris cover on Khumbu Glacier, Nepal using a positive degree-day factor, *Symposium at Seattle 2000 – Debris-Covered Glaciers, IAHS Publ.*, 264, 71–81, 2000.
- Klok, E. J., and Oerlemans, J.: Model study of the spatial distribution of the energy and mass balance of Morteratschgletscher, Switzerland, *J. Glaciol.*, 48, 505–518, 2002.
- Kotlarski, S., Paul, F., and Jacob, D.: Forcing a distributed glacier mass balance model with the regional climate model REMO. Part I: Climate model evaluation, *J. Climate*, 23, 1589–1606, 2010a.
- Kotlarski, S., Jacob, D., Podzum, R., and Paul, F.: Representing glaciers in a regional climate model, *Clim. Dynam.*, 34, 27–46, 2010b.
- Knierel, J. C., Bryan, G. H., and Hacker, J. P.: Explicit numerical diffusion in the WRF model, *Mon. Weather Rev.*, 135, 3808–3824, 2007.
- Kraus, H.: An energy-balance model for ablation in mountainous areas, *Snow and Ice-Symposium-Neiges et Glaces, August 1971, IAHS-AISH PUBLICATION no. 104*, 1975.
- Lejeune, Y., Bertrand, J.-M., Wagnon, P., and Morin, S.: A physically based model of the year-round surface energy and mass balance of debris-covered glaciers, *J. Glaciol.*, 59, 327–344, 2013.
- Livneh, B., Xia, Y., Mitchell, K. E., Ek, M. B., and Lettenmaier, D. P.: Noah LSM snow model diagnostics and enhancements, *J. Hydrometeorol.*, 11, 721–738, 2009.

- Lohman, S. W.: Ground-water hydraulics. U.S. Geological Survey Professional Paper 708, 1972.
- Loomis, S. R.: Morphology and ablation processes on glacier ice, *Assoc. Am. Geogr. Proc.*, 2, 88–92, 1970.
- Lutz, A. F., Immerzeel, W. W., Shrestha, A. B., and Bierkens, M. F. P.: Consistent increase in High Asia's runoff due to increasing glacier melt and precipitation, *Nat. Clim. Chang.*, 4, 16, 2014.
- MacDonell, S., Kinnard, C., Mölg, T., Nicholson, L., and Abermann, J.: Meteorological drivers of ablation processes on a cold glacier in the semi-arid Andes of Chile, *The Cryosphere*, 7, 1513–1526, 2013.
- Machguth, H., Paul, F., Kotlarski, S., and Hoelzle, M.: Calculating distributed glacier mass balance for the Swiss Alps from regional climate model output: a methodical description and interpretation of the results, *J. Geophys. Res.*, 114, D19106, doi:10.1029/2009JD011775, 2009.
- Marshall, S. J., Sharp, M. J., Burgess, D. O., and Anslow, F. S.: Surface temperature lapse rate variability on the Prince of Wales Ice-eld, Ellesmere Island, Canada: implications for regional-scale downscaling of temperature, *Int. J. Climatol.*, 27, 385–398, 2007.
- Martin, E., and Lejeune, Y.: Turbulent fluxes above the snow surface, *Ann. Glaciol.*, 26, 179-183, 1998.
- Mattson, L. E., Gardner, J. S., and Young, G. J.: Ablation on debris covered glaciers: an example from the Rakhiot Glacier, Punjab, Himalaya, *Snow and Glacier Hydrology, IAHS-IASH Publ.*, 218, 289–296, 1993.
- Maussion, F., Scherer, D., Finkelnburg, R., Richters, J., Yang, W., and Yao, T.: WRF simulation of a precipitation event over the Tibetan Plateau, China – an assessment using remote sensing and ground observations, *Hydrol. Earth Syst. Sci.*, 15, 1795–1817, 2011.
- Maussion, F., Scherer, D., Mlg, T., Collier, E., Curio, J., and Finkelnburg, R.: Precipitation seasonality and variability over the Tibetan Plateau as resolved by the High Asia Reanalysis, *J. Climate*, 27, 1910–1927, 2014.

- Mayer, C., Lambrecht, A., Belo, M., Smiraglia, C., and Diolaiuti, G.: Glaciological characteristics of the ablation zone of Baltoro glacier, Karakoram, Pakistan, *Ann. Glaciol.*, 43, 123–131, 2006.
- Mayer, C., Lambrecht, A., Mihalcea, C., Belo, M., Diolaiuti, G., Smiraglia, C., and Bashir, F.: Analysis of Glacial Meltwater in Bagrot Valley, Karakoram, *Mtn. Res. Dev.*, 30, 169–177, 2010.
- Mayer, C., Lambrecht, A., Oerter, H., Schwikowski, M., Vuillermoz, E., Frank, N., and Diolaiuti, G.: Accumulation Studies at a High Elevation Glacier Site in Central Karakoram, *Adv. Meteorol.*, 2014, 1–12, 2014.
- Mihalcea, C., Mayer, C., Diolaiuti, G., Smiraglia, C., and Tartari, G.: Ablation conditions on the debris covered part of Baltoro Glacier, Karakoram, *Ann. Glaciol.*, 43, 292–300, 2006.
- Mihalcea, C., Mayer, C., Diolaiuti, G., DAgata, C., Smiraglia, C., Lambrecht, A., Vuillermoz, E., and Tartari, G.: Spatial distribution of debris thickness and melting from remote-sensing and meteorological data, at debris-covered Baltoro glacier, Karakoram, Pakistan, *Ann. Glaciol.*, 48, 49–57, 2008.
- Molinari, J. and Dudek, M.: Parameterization of convective precipitation in mesoscale numerical-models – a critical-review, *Mon. Weather Rev.*, 120, 326–344, 1992.
- Mölg, T., Cullen, N. J., Hardy, D. R., Kaser, G., and Klok, E. J.: Mass balance of a slope glacier on Kilimanjaro and its sensitivity to climate, *Int. J. Climatol.*, 28, 881–892, 2008.
- Mölg, T., Cullen, N. J., Hardy, D. R., Winkler, M., and Kaser, G.: Quantifying climate change in the tropical midtroposphere over East Africa from glacier shrinkage on Kilimanjaro, *J. Climate*, 22, 4162–4181, 2009.
- Mölg, T. and Kaser, G.: A new approach to resolving climate–cryosphere relations: downscaling climate dynamics to glacier-scale mass and energy balance without statistical scale linking, *J. Geophys. Res.*, 116, D16101, doi:10.1029/2011JD015669, 2011.

- Mölg, T., Maussion, F., Yang, W., and Scherer, D.: The footprint of Asian monsoon dynamics in the mass and energy balance of a Tibetan glacier, *The Cryosphere*, 6, 1445–1461, 2012a.
- Mölg, T., Großhauser, M., Hemp, A., Hofer, M., and Marzeion, B.: Limited forcing of glacier loss through land-cover change on Kilimanjaro, *Nat. Clim. Change*, 2, 254–258, 2012b.
- Mölg, T., Maussion, F., and Scherer, D.: Mid-latitude westerlies as a driver of glacier variability in monsoonal High Asia, *Nat. Clim. Change*, 4, 68–73, 2013.
- Nakawo, M. and Young, G. J.: Field experiments to determine the effect of a debris layer on ablation of glacier ice, *Ann. Glaciol.*, 2, 85–91, 1981.
- Nakawo, M. and Young, G. J.: Estimate of glacier ablation under a debris layer from surface temperature and meteorological variables, *J. Glaciol.*, 28, 29–34, 1982.
- Nicholson, L. and Benn, D.: Calculating ice melt beneath a debris layer using meteorological data, *J. Glaciol.*, 52, 463–470, 2006.
- Nicholson, L. and Benn, D.: Properties of natural supraglacial debris in relation to modelling sub-debris ice ablation, *EPSL*, 38, 490–501, 2012.
- Nicholson, L., Prinz, R., Mölg, T., and Kaser, G.: Micrometeorological conditions and surface mass and energy fluxes on Lewis glacier, Mt Kenya, in relation to other tropical glaciers. *The Cryosphere*, 7, 1205–1225, 2013.
- Niu, G.-Y., Yang, Z.-L., Mitchell, K. E., Chen, F., Ek, M. B., Barlage, M., Kumar, A., Manning, K., Niyogi, D., Rosero, E., Tewari, M., and Youlong, X.: The community Noah land surface model with multiparameterization options (Noah-MP): 1. Model description and evaluation with local-scale measurements, *J. Geophys. Res.*, 116, D12109, doi:10.1029/2010JD015139, 2011.
- Oerlemans, J. and Knap, W. H.: A 1 year record of global radiation and albedo in the ablation zone of Morteratschgletscher, Switzerland, *J. Glaciol.*, 44, 231–238, 1998.
- Østrem, G.: Ice melting under a thin layer of moraine, and the existence of ice cores in moraine ridges, *Geogr. Ann.*, 41, 228–230, 1959.

- Paul, F. and Kotlarski, S.: Forcing a distributed glacier mass balance model with the regional climate model REMO. Part II: Downscaling strategy and results for two Swiss glaciers, *J. Climate*, 23, 1607–1620, 2010.
- Petch, J. C.: Sensitivity study of developing convection in a cloud-resolving model, *Q. J. Roy. Meteorol. Soc.*, 132, 345–358, 2006.
- Petersen, L. and Pellicciotti, F.: Spatial and temporal variability of air temperature on a melting glacier: atmospheric controls, extrapolation methods and their effect on melt modeling, Juncal Norte Glacier, Chile, *J. Geophys. Res.*, 116, D23109, doi:10.1029/2011JD015842, 2011.
- Pellicciotti, F., Stephan, C., Miles, E., Immerzeel, W. W., and Bolch, T.: Mass balance changes of the debris-covered glaciers in the Langtang Himal in Nepal between 1974 and 1999, *J. Geophys. Res.*, in Press., 127.
- Pfeffer, W. T., Arendt, A., Bliss, A., Bolch, T., Cogley, J. G., Gardner, A. S., Hagen, J.-O., Hock, R., Kaser, G., Kienholz, C., Miles, E. S., Moholdt, G., Mölg, N., Paul, F., Radic, V., Rastner, P., Raup, B. H., Rich, J., and Sharp, M. J.: The Randolph Glacier Inventory: a globally complete inventory of glaciers, *J. Glaciol.*, 221, 537–552, 2014.
- Pritchard, M. S., Bush, A. B. G., and Marshall, S. J.: Neglecting ice-atmosphere interactions underestimates ice sheet melt in millennial-scale deglaciation simulations, *Geophys. Res. Lett.*, 35, L01503, doi:10.1029/2007GL031738, 2008.
- Quincey, D. J., Copland, L., Mayer, C., Bishop, M., Luckman, A., and Belo, M.: Ice velocity and climate variations for Baltoro Glacier, Pakistan, *J. Glaciol.*, 55, 1061–1071, 2009.
- Radić, V. and Hock, R.: Regionally differentiated contribution of mountain glaciers and ice caps to future sea-level rise, *Nat. Geosci.*, 4, 91–94, 2011.
- Rankl, M., Kienholz, C., and Braun, M.: Glacier changes in the Karakoram region mapped by multiresolution satellite imagery, *The Cryosphere*, 8, 977–989, 2014.
- Reid, T. D. and Brock, B. W.: An energy-balance model for debris-covered glaciers including heat conduction through the debris layer, *J. Glaciol.*, 56, 903–916, 2010.

- Reid, T. D., Carenzo, M., Pellicciotti, F., and Brock, B. W.: Including debris cover effects in a distributed model of glacier ablation, *J. Geophys. Res.*, 117, D18105, doi:10.1029/2012JD017795, 2012.
- Reid, T. D. and Brock, B. W.: Assessing ice-cliff backwasting and its contribution to total ablation of debris-covered Miage glacier, Mont Blanc massif, Italy, *J. Glaciol.*, 60, 3–13, 2014.
- Reijmer, C. H. and Hock, R.: Internal accumulation on Storglaciaren, Sweden, in a multi-layer snow model coupled to a distributed energy- and mass- balance model, *J. Glaciol.*, 54, 61–71, 2008.
- Reznichenko, N., Davies, T., Shulmeister, J., and McSaveney, M.: Effects of debris on ice-surface melting rates: an experimental study, *J. Glaciol.*, 56, 384–394, 2010.
- Ridley, J. K., Huybrechts, P., Gregory, J. M., and Lowe, J. A.: Elimination of the Greenland ice sheet in a high CO₂ climate, *J. Climate*, 18, 3409–3427, 2005.
- Sakai, A., Nakawo, M., and Fujita, K.: Melt rate of ice cliffs on the Lirung Glacier, Nepal Himalayas, 1996. *Bull. Glacier Res.*, 16, 57–66, 1998.
- Sakai, A., Takeuchi, N., Fujita, K., and Nakawo, N.: Role of supraglacial ponds in the ablation process of a debris-covered glacier in the Nepal Himalaya. *Debris-Covered Glaciers*, IAHS PUBLICATION no. 264, 119–130, 2000.
- Sakai, A., Fujita, K., and Kubota, J.: Evaporation and percolation effect on melting at debris-covered Lirung Glacier, Nepal Himalayas, 1996, *Bull. Glaciol. Res.*, 21, 9–15, 2004.
- Scherler, D., Bookhagen, B., and Strecker, M. R.: Spatially variable response of Himalayan glaciers to climate change affected by debris cover, *Nat. Geosci.*, 4, 156–159, 2011.
- Scherler, D., Bookhagen, B., and Strecker, M. R.: Hillslopeglaciers coupling: The interplay of topography and glacial dynamics in High Asia, *J. Geophys. Res.*, 116, doi:10.1029/2010JF001751, 2011.

- Scherler, D., and Strecker, M. R.: Large surface velocity fluctuations of Biafo Glacier, central Karakoram, at high spatial and temporal resolution from optical satellite images, *J. Glaciol.*, 58, 569-580, 2012.
- Searle, M. P.: *Geology and Tectonics of the Karakoram Mountains*, John Wiley and Sons, Chichester, 1991.
- Sheng, D.: Review of fundamental principles in modelling unsaturated soil behaviour, *Comput. Geotech.*, 38, 757-776, 2011.
- Shi, Y., Liu, C., and Kang, E.: The glacier inventory of China, *Ann. Glaciol.*, 50, 1-4, 2009.
- Skamarock, W. C. and Klemp, J. B.: A time-split nonhydrostatic atmospheric model for weather research and forecasting applications, *J. Comput. Phys.*, 227, 3465-3485, 2008.
- Smith, G. D.: *Numerical solution of partial differential equations: finite difference methods*, 3rd edn., Oxford, Oxford University Press, 1985.
- Stokes, C. R., Popovnin, V., Aleynikov, A., Gurney, S. D., and Shahgedanova, M.: Recent glacier retreat in the Caucasus Mountains, Russia, and associated increase in supraglacial debris cover and supra-/proglacial lake development, *Ann. Glaciol.*, 46, 195-203, 2007.
- Stroeve, J. C., Box, J. E., and Haran, T.: Evaluation of the MODIS (MOD10A1) daily snow albedo product over the Greenland ice sheet, *Remote Sens. Environ.*, 105, 155-171, 2006.
- Suzuki, R., Fujita, K., and Ageta, Y.: Spatial distribution of thermal properties on debris-covered glaciers in the Himalayas derived from ASTER data, *Bull. Glaciol. Res.*, 24, 13-22, 2007.
- Takeuchi, Y., Kayastha, R. B., and Nakawo, M.: Characteristics of ablation and heat balance in debris-free and debris-covered areas on Khumbu glacier, Nepal Himalayas, in the pre-monsoon season, in: *Debris-covered glaciers*, IAHS Publ., 264, 53-61, 2000.
- Takeuchi, Y., Kayastha, R. B., Naito, N., Kadota, T., and Izumi, K.: Comparison of meteorological features in the debris-free and debris-covered areas at Khumbu Glacier, Nepal Himalayas, in the premonsoon season, 1999, *Bull. Glaciol. Res.*, 18, 15-18, 2001.

- Thompson, G., Field, P. R., Rasmussen, R. M., and Hall, W. D.: Explicit forecasts of winter precipitation using an improved bulk microphysics scheme. Part II: Implementation of a new snow parameterization, *Mon. Wea. Rev.*, 136, 5095–5115, 2008.
- Treydte, K. S., Schleser, G. H., Helle, G., Frank, D. C., Winiger, M., Haug, G. H., and Esper, J.: The twentieth century was the wettest period in northern Pakistan over the past millennium, *Nature*, 440, 1179–1182, 2006.
- van Pelt, W. J. J., Oerlemans, J., Reijmer, C. H., Pohjola, V. A., Pettersson, R., and van Angelen, J. H.: Simulating melt, runoff and refreezing on Nordenskiöldbreen, Svalbard, using a coupled snow and energy balance model, *The Cryosphere*, 6, 641–659, 2012.
- Wagnon, P., Vincent, C., Arnaud, Y., Berthier, E., Vuillermoz, E., Gruber, S., Ménégoz, M., Gilbert, A., Dumont, M., Shea, J. M., Stumm, D., and Pokhrel, B. K.: Seasonal and annual mass balances of Mera and Pokalde glaciers (Nepal Himalaya) since 2007, *The Cryosphere*, 7, 1769–1786, 2013.
- Wake, C. P.: Glaciochemical investigations as a tool for determining the spatial and seasonal variation of snow accumulation in the central Karakoram, northern Pakistan. *Ann. Glaciol.*, 13, 279–284, 1989.
- Webb, E. K., Pearman, G. I., and Leuning, R.: Correction of flux measurements for density effects due to heat and water vapour transfer, *Q. J. Roy. Meteor. Soc.*, 106, 85–100, 1980.
- Weisman, M. L., Skamarock, W. C., and Klemp, J. B.: The resolution dependence of explicitly modeled convective systems, *Mon. Weather Rev.*, 125, 527–548, 1997.
- Wilson, G. W., Fredlund, D. G., and Barbour, S.L.: Coupled soil-atmosphere modelling for soil evaporation, *Can. Geotech. J.*, 31, 151–161, 1994.
- Winiger, M., Gumpert, M., and Yamout, H.: KarakorumHindukushwestern Himalaya: assessing highaltitude water resources, *Hydrol. Process.*, 19, 2329–2338, 2005.
- Yadav, R. R., Park, W.-K., Singh, J., and Dubey, B.: Do the western Himalayas defy global warming? *Geophys. Res. Letts.*, 31, L17201, doi:10.1029/2004GL020201, 2004.

- Yao, T.: Map of the Glaciers and Lakes on the Tibetan Plateau and Adjoining Regions, Xian Cartographic Publishing House, Xian, China, 2007.
- Yeh, H-F., Lee, C.-C., and Lee, C.-H.: A rainfall-infiltration model for unsaturated soil slope stability, *J. Environ. Eng. Manage.*, 18, 261–268, 2008.
- Young, G. J. and Hewitt, K.: Glaciohydrological features of the Karakoram Himalaya: measurement possibilities and constraints, in: *Proceedings of the Kathmandu Symposium – Snow and Glacier Hydrology*, IAHS Publ., 218, 273–283, 1993.
- Zhang, Y., Fujita, K., Liu, S., Liu, Q., and Nuimura, T.: Distribution of debris thickness and its effect on ice melt at Hailuoguo glacier, southeastern Tibetan Plateau, using in situ surveys and ASTER imagery, *J. Glaciol.*, 57, 1147–1157, 2011.
- Zeng, Y., Su, Z., Wan, L., and Wen, J.: A simulation analysis of the advective effect on evaporation using a two-phase heat and mass flow model, *Water Resour. Res.*, 47, W10529, doi:10.1029/2011WR010701, 2011.